

**NASA
Technical
Paper
3184**

1992

**Wind Tunnel Aerodynamic
Characteristics of a
Transport-Type Airfoil
in a Simulated Heavy
Rain Environment**

Gaudy M. Bezos,
R. Earl Dunham, Jr.,
and Garl L. Gentry, Jr.
*Langley Research Center
Hampton, Virginia*

W. Edward Melson, Jr.
*Wallops Flight Facility
Wallops Island, Virginia*

NASA

National Aeronautics and
Space Administration

Office of Management

Scientific and Technical
Information Program



Summary

A wind tunnel investigation was conducted with a cambered airfoil representative of typical commercial transport wing sections in the Langley 14-by-22-Foot Subsonic Tunnel to determine the aerodynamic penalty associated with a simulated heavy rain encounter. The model was comprised of an NACA 64-210 airfoil section with a chord of 2.5 ft, a span of 8 ft, and was mounted on the tunnel centerline between two large endplates. The rain simulation system manifold, which was located 10 chord lengths upstream of the model, produced liquid water contents ranging from 16 to 46 g/m³. Aerodynamic measurements in and out of the simulated rain environment were obtained for dynamic pressures of 30 and 50 psf and an angle-of-attack range of 0° to 20° for the cruise configuration and 4° to 20° for the landing configuration (leading-edge slat and trailing-edge double-slotted flap). Both configurations experienced significant losses in maximum lift capability, increases in drag for a given lift condition, and a progressive decrease in the lift curve slope at both dynamic pressures as the liquid water content increased. The results obtained on the landing configuration also indicated a progressive decrease in the angle of attack at which maximum lift occurred and an increase in the slope of the pitching-moment curve as the liquid water content increased. Accompanying the reduction in the stall angle of attack was the general flattening of the lift curve past stall as the liquid water content was increased. The NACA 64-210 data indicated that the severity of the rain effect appears to be configuration-dependent and is most severe for high-lift configuration airfoils with leading- and trailing-edge devices configured for landing or take-off operations. Experiments were also conducted to investigate the sensitivity of test results to the effects of water surface tension by introducing a surface-tension reducing agent into the rain spray. The reduction in the surface tension of water by a factor of 2 did not significantly alter the level of performance losses for the landing configuration tested.

Introduction

This investigation is part of a broad National Aeronautics and Space Administration (NASA) research program to obtain fundamental aerodynamic information regarding the effect of heavy rain on aircraft performance. The aim of the program is to understand the physical phenomena associated with any aerodynamic performance penalty that may occur during a rain encounter, particularly during take-off and landing.

Until the late 1970's the recognition of weather-related safety hazards to aircraft performance during take-off and landing operations included lightning, icing, hail, low-altitude wind shear, and microburst phenomena. Since 1971, research has been directed at determining the nature and characteristics of the wind shear/microburst phenomenon. In 1977, the Federal Aviation Administration (FAA) conducted a study on aircraft accidents and incidents from 1964 to 1976 in which low-altitude wind shear could have been a contributing factor (ref. 1). The study, which identified 25 cases (23 approach or landing and 2 take-off) involving large aircraft (gross weights in excess of 12 500 lb), indicated that 10 cases had occurred in a rain environment, 5 of which were classified as intense or heavy rain encounters. These findings led to the consideration of heavy rain, i.e., high-intensity, short-duration rain, as being a potential weather-related aircraft safety hazard. Specifically, a pilot of an aircraft encountering low-altitude wind shear during take-off or landing operations would depend upon "dry" aircraft performance margins. If the wind shear environment is immersed in a severe convective rainstorm, the actual performance margins may be significantly reduced. A determination of the effect of rain on aircraft performance is required to provide safe piloting procedures for a wind shear encounter in a severe rain environment.

The rain environment present in convective storms has been of interest to the meteorological and aviation communities for many years. The parameters used to characterize rain are the rainfall rate and the liquid water content. At ground level, rainfall rate, the rate at which rain falls (usually expressed in either in/hr or mm/hr) is generally used to characterize a rain event. For airborne measurements, the relevant parameter is the liquid water content, which is the mass of liquid water contained in a unit volume of air and is usually expressed in grams per cubic meter of air (g/m³). The relationship between liquid water content and rainfall rate is uniquely dependent on the type of storm and the intensity level of the storm as detailed in appendix A. Measurements made above ground by airplanes instrumented for atmospheric research have shown that convective storms can contain localized regions of high-intensity rain. As these localized regions of high-intensity rain precipitate toward the ground, gusting winds disperse the liquid water over a larger region that results in lower ground-based rain intensity measurements than actually exist at altitude. The world record ground-level rainfall rate of 73.8 in/hr was recorded in Unionville, Maryland, for a short time (approximately 1 min) on July 4, 1956, in an intense

afternoon thunderstorm (ref. 2). In 1962, Roys and Kessler (ref. 3) conducted measurements of liquid water content in a thunderstorm with an instrumented F-100 airplane. The instrumented airplane recorded an average liquid water content value of approximately 8.4 g/m^3 with a peak value of 44 g/m^3 . The ground-based radar measurements in those experiments indicated modest rainfall rates of 1.48 in/hr. Prior to 1987, all ground-based natural rainfall rate measurements were averaged over relatively long time periods, on the order of minutes and hours (ref. 4), which masked the short-duration, high-intensity rain characteristics associated with convective storms and wind shear/microburst phenomena. This result led to the development of a ground-based natural rainfall rate measurement technique by Melson to acquire data over very short time periods, as short as one sample per second (ref. 5). His results verified the existence of high-intensity rain: over 7000 events measured above 4 in/hr with a maximum rain event of 29 in/hr for short time intervals on the order of 10 to 30 sec at ground level.

The earliest analytical work on the effect of rain on aerodynamic performance was conducted by Rhode in 1941 (ref. 6). His analysis indicated that drag increases associated with the momentum imparted to a DC-3 aircraft encountering a rain cloud with a liquid water content of 50 g/m^3 would cause an 18-percent reduction in airspeed. Rhode considered such an encounter to be of little consequence to an aircraft flying at 5000 ft. Because low-visibility take-offs and landings were not routine in 1941, the consequences of a heavy rain encounter during these phases of flight were not considered. However, for a modern day transport such an airspeed loss during take-off or landing would be significant.

The reconsideration of heavy rain as a potential weather-related aircraft safety hazard in 1977 led to the development of a broad experimental and analytical research effort, spearheaded by NASA to determine the effect of heavy rain on aircraft performance. In 1982, Haines and Luers (ref. 7), under contract from Wallops Flight Facility, analytically evaluated the effect of rain on aircraft landing performance. Their study refined the work of Rhode by estimating the effects of rain on a modern day transport. Their analysis not only included the calculation of the impact momentum of the raindrops, but also estimated the increase in skin-friction drag by equating the two-phase flow phenomenon over the airfoil surface to an equivalent sandgrain roughness. Reduc-

tions in lift capability were calculated with empirical data of roughness effects on airfoil lift. Their analysis indicated that a Boeing 747 transport encountering a rain cloud with a liquid water content of 18 g/m^3 (based on a rainfall rate of 39 in/hr) would experience a 5-percent increase in drag, a 29-percent reduction in maximum lift capability, and a 5° reduction in the angle of attack for maximum lift. These predictions constitute a substantial loss of performance.

At the time of the Haines' and Luers' analysis, no experimental data existed for verification of the predictions. Hence in 1981, an experimental research program was established at Langley Research Center to obtain a heavy rain effects data base. Small-scale wind tunnel model tests were considered to provide the most controlled environment for evaluating the effects of rain on airfoil performance. Test techniques and procedures were developed and exploratory wind tunnel tests were conducted on an NACA 0012 airfoil section fitted with a simply hinged, full-span trailing-edge flap in the Langley 14- by 22-Foot Subsonic Tunnel (ref. 8). The wind tunnel rain simulation system produced liquid water content levels ranging from 13 to 22 g/m^3 . A 15-percent reduction in the maximum lift capability of both the cruise and landing configurations of the airfoil model was measured in the simulated rain environment independent of the liquid water content level. The exploratory small-scale wind tunnel results confirmed the existence of a performance penalty in a simulated rain environment.

The objective of the present investigation was threefold: first, to determine the severity of the rain effect on a cambered airfoil representative of typical commercial transport wing sections; second, to determine the aerodynamic penalty over a wider range of rain intensities; and third, to explore the importance of surface-tension interactions of water as a scaling parameter. The data presented in this report were obtained with an NACA 64-210 airfoil model with leading- and trailing-edge high-lift devices tested in cruise and landing configurations. The tests were conducted in the Langley 14- by 22-Foot Subsonic Tunnel at dynamic pressures of 30 and 50 psf, which correspond to Reynolds numbers of 2.6×10^6 and 3.3×10^6 based on airfoil chord. The rain intensity was varied to produce liquid water content levels ranging from 16 to 46 g/m^3 . The test results are described in terms of lift, drag, and pitching-moment characteristics in and out of the simulated rain environment and represent the baseline data to be used in the evaluation of full-scale modeling of rain effects.

Symbols

b	airfoil metric section span, 1 ft
c	airfoil chord, 2.5 ft
c_d	section drag coefficient, Drag/qbc
c_l	section lift coefficient, Lift/qbc
c_m	section pitching-moment coefficient, $\text{Pitching moment}/qbc^2$
D	drop diameter, mm
D_1	arithmetic mean drop diameter, mm
D_2	volumetric mean drop diameter, mm
H	height of rain spray at model location, ft
ID	inner diameter of hypodermic-type nozzle, in.
K	conversion constant
LWC	liquid water content, g/m^3 (see fig. 12 and appendix A)
$N(D)$	drop size density function
Q	volumetric flow rate, gal/min
q	free-stream dynamic pressure, psf
R	rainfall rate, in/hr
Re	free-stream Reynolds number, $\rho_a V c / \mu_a$
V	free-stream velocity, ft/sec
W	width of rain spray at model location, ft
We	Weber number, $0.00328 \rho_w V^2 D_2 / \sigma_{w,a}$
x	chordwise location of model geometry, ft
z	ordinate location corresponding to x , ft
α	angle of attack, deg
μ_a	viscosity of air, slugs/ft-sec
μ_w	viscosity of water, slugs/ft-sec
ρ_a	density of air, slugs/ft ³
ρ_w	density of water, slugs/ft ³
$\sigma_{w,a}$	surface tension between water and air, slugs/sec ²

Apparatus and Procedure

Wind Tunnel and Model Support

The present investigation was conducted in the Langley 14- by 22-Foot Subsonic Tunnel, which is a closed-circuit atmospheric wind tunnel allowing open and closed test section operation (ref. 9). For this investigation, the tests were conducted in the closed test section with dimensions of 14.5 ft high by 21.75 ft wide by 50 ft long. A photograph of the test setup is shown in figure 1. The model hardware, aligned laterally with the tunnel centerline, was located in the aft bay of the test section. The rain simulation system manifold, which was located approximately 10 wing chord lengths upstream of the model location, directed the rain spray horizontally at the model.

Model

The model used in this investigation had a rectangular planform and was supported between two endplates in an attempt to represent a two-dimensional test setup (fig. 2). The airfoil chord was 2.5 ft and the span between the endplates was 8 ft. An NACA 64-210 airfoil section was chosen as being representative of a cambered, commercial transport wing section. The model was equipped with leading- and trailing-edge high-lift devices. Details of the cruise and landing configurations that were tested are shown in figure 3 and in tables 1(a) and (b). For the landing configuration, the high-lift devices consisted of a leading-edge slat deflected 57° and a trailing-edge double-slotted flap deflected 35.75° . For the cruise configuration, the model leading-edge slat was stowed and the trailing-edge flap system was replaced with a cruise flap section installed flush to the aft end of the main wing section. The stowed leading-edge slat produced an aft-facing step of 0.059 in. that was not faired to the main wing section contour.

The model consisted of a 1-ft span metric center section mounted between two nonmetric outer panels. The center section was mounted on an internal, three-component, strain-gauge balance and was separated from the outboard panels by small gaps that were sealed with a thin, flexible layer of rubber (dental dam) to approximate two-dimensional flow and eliminate three-dimensional effects caused by leakage. The sealing technique did not degrade the balance performance. Aerodynamic data were obtained with the boundary-layer transition fixed with No. 80 grit along the 5-percent chordline on the upper and lower surfaces of the wing and each high-lift element in accordance to reference 10.

Rain Simulation System

The simulation of natural rain in a wind tunnel environment should be able to simultaneously produce a natural rain drop size distribution, vary the rain intensity level, and provide uniform rain spray coverage at the model location with minimal influence on the tunnel free-stream conditions. The wind tunnel rain simulation technique developed during the exploratory small-scale tests (ref. 8) identified an inherent difficulty in producing large size drops typical of natural rain while at the same time achieving the desired rain intensity and drop size distribution. When water is injected into a high-velocity airstream at a velocity substantially less than the airstream velocity, the larger drops that form break up almost immediately into much smaller drops as detailed in reference 11. Although this difficulty can be alleviated by increasing the water injection pressure so that the initial drop velocity approaches the airstream velocity, the resulting rain intensity tends to be too high. The exploratory small-scale tests indicated that the drop size distribution and the rain intensity levels were a function of the nozzle design, water injection pressure, and airstream velocity.

An extensive experimental research effort was carried out by the Jet Propulsion Laboratory (JPL) to develop a nozzle design that would simulate a range of rain intensity levels and a drop size distribution that would include drops 2 mm in size and larger (ref. 12). The JPL-designed nozzle consisted of a series of 0.063-in-diameter hypodermic tubes arranged circumferentially around a plenum (fig. 4(a)). The hypodermic nozzle design provided the flexibility to independently vary the rain intensity while retaining control over the drop size. The rain intensity produced by the hypodermic nozzle design was a function of the air supply pressure, dynamic pressure, and number of tubes in the particular nozzle configuration. The JPL research effort led to the selection of two nozzle configurations, a 5- and 7-tube (B1N5 and B1N7, respectively), as shown in figure 4(b). Also shown in figure 4(b) is a commercially available fan jet nozzle (1570), previously used in the exploratory wind tunnel tests on the NACA 0012 airfoil model. This nozzle had an elliptical cross section and produced the highest volumetric flow rate of the three. The 5- and 7-tube hypodermic nozzles, along with the fan jet nozzle, were each used separately (no mixing of nozzle type) in the present investigation to determine the severity of the performance degradation as a function of rain intensity. The 5-tube hypodermic nozzle produced the lowest rain intensity and the fan jet nozzle produced the highest rain intensity.

The rain simulation system hardware was designed to meet the volumetric flow requirements of the fan jet nozzle. A schematic of the hardware setup is shown in figure 5. The rain simulation system consisted of a 20-gallon water tank accumulator, a manifold, and three sets of nozzles (5-tube, 7-tube, and fan jet nozzle set). A remotely controlled air pressure valve regulated the water supply to the tank, which was connected to the manifold. The air supply pressure was varied to control the volume of water passing through the manifold and exiting out the nozzles. The operating pressure was limited to a maximum of 100 psig. The volumetric flow rate and the air supply pressure were both measured and recorded.

The rain simulation system manifold was fabricated from streamlined steel tubing having a chord length of 3.5 in. and a fineness ratio (chord length to thickness) of 2.2 to minimize the interference effect on tunnel free-stream conditions. The manifold was located 25 ft upstream of the model (approximately 10 wing chord lengths) to allow time for the stabilization of the accelerating water droplets and the dispersion of the manifold disturbances on tunnel free-stream conditions. The manifold was aligned approximately 6 in. above the chord plane of the model to account for gravity effects on the water droplets. Comparisons of model aerodynamic data in and out of the simulated rain environment were measured with the spray manifold in position at all times.

The manifold hardware shown in figure 6 was initially designed to immerse the NACA 0012 airfoil model in a simulated rainfield (ref. 8). The manifold was modified for the present investigation to ensure coverage of the NACA 64-210 model. Two vertical posts spaced 1 ft apart at the center of the horizontal bar of the manifold were added as shown in figure 7. The vertical and horizontal spacing of the three sets of nozzles was determined by trial and error. The optimum nozzle spacing (the same for all three nozzle sets) is shown in figure 7 with a total of four nozzles, two nozzles on each vertical post. Each nozzle is spaced 1 ft apart from the other both horizontally and vertically to completely immerse the instrumented 1-ft metric center section of the NACA 64-210 airfoil model. The simulated rainfield was centered about the model chordline for a total height of approximately 4 ft and extended approximately 1.5 ft on either side of the metric center section for all the nozzle configurations tested.

Rain Simulation System Calibration

As was previously mentioned, the parameters used to characterize rain are the rainfall rate (R)

and the liquid water content (LWC). The relationship between R and LWC is uniquely dependent on the type of storm and the intensity level of the storm (refs. 2 and 13). A detailed description of this relationship can be found in appendix A. The wind tunnel rain system simulates a thunderstorm-type rain that is defined as being a high-intensity, short-duration rain. The wind tunnel simulated rainfield was quantified in terms of drop size distribution, drop velocity, and LWC.

As part of the nozzle development research effort, JPL developed a shadowgraph technique to measure the drop size and drop velocity distributions produced in a wind tunnel environment. The shadowgraph technique used a pulsed ruby laser as shown in figure 8. The photographic optics were arranged to sample a small region in the central portion of the spray just in front of the model location. A typical shadowgraph photograph is shown in figure 9 for a dynamic pressure of 30 psf. The photographic negatives were digitized on a computerized optical scanner and analyzed to determine drop population characteristics of the hypodermic and fan jet nozzle types.

The drop size distribution data were obtained at dynamic pressures of 15, 30, and 50 psf for the hypodermic-type nozzle and 30 and 70 psf for the fan jet nozzle type as tabulated in table 2(a). Drop size was a function of nozzle type, water injection pressure, and tunnel test velocity. Note that the drop size and drop velocity characteristics measured for the JPL-designed hypodermic nozzle are applicable for both the 5- and 7-tube configurations because the nozzles have the same tube geometry (i.e., inner diameter, see fig. 4(a)). The drop population characteristics are tabulated in terms of the arithmetic mean drop diameter, the volumetric mean drop diameter, and the ratio of the drop velocity to the free-stream velocity. The volumetric mean drop diameter is defined as that drop diameter for which half the total volume of the rain spray is in larger drops and half in smaller drops. The distribution of the drop sizes, shown in figures 10 and 11, indicates a large difference between the geometric and volumetric mean drop diameters due to the existence of many small drops in the simulated rainfield. The wind tunnel rain simulation technique did not produce a natural rain drop size distribution as detailed in references 13 to 15.

The laser system also was operated in a double-pulsed mode with about 20 msec between pulses to determine drop velocity. Drop velocity data are shown in table 2(b) for the hypodermic-type nozzle. At the lower dynamic pressure of 15 psf, the water

droplets produced by the hypodermic-type nozzle were moving at approximately 92-percent free-stream velocity, but at the higher dynamic pressure of 30 psf, the drop velocity was approximately 89 percent of the free-stream velocity. It is interesting to note that the measured drop velocities were independent of the drop size at the model location. In summary, the mean drop size decreased with increasing tunnel test speed and the drop velocity was measured to be about 90 percent of the free-stream velocity for all nozzle configurations.

In a wind tunnel environment, LWC is expressed as a function of the rainfield area, volumetric flow rate, and free-stream velocity as shown by the relationship in figure 12. A flowmeter measured the volume of water flowing through the manifold. The rainfield width and height were photographically obtained at the model location with a fluorescent dye, an ultraviolet strobe light to enhance the photographic qualities of the rainfield, and a nearfield linear-length reference. A photograph of a typical simulated rainfield is shown in figure 13. The rainfield appears to be uniformly distributed at the model location. Because of the dynamic nature of water drops, the boundaries of the rain spray region at any instant in time are not precise straight lines. Therefore, deriving the rain spray by photographic means involves subjectively determining the usable rain spray region boundaries. The rain spray area produced by the three nozzle configurations is presented in table 2(c) as a function of nozzle type, tunnel dynamic pressure, air supply pressure, and volumetric flow rate.

Scaling of Rain Effects

Because of the complexity of the two-phase flow environment, the established wind tunnel model to full-scale scaling laws may not be applicable in the rain environment. In 1985, Bilanin (ref. 16) addressed the subject of scaling for model tests of airfoils in simulated rain. His analysis showed that the following variables, relevant to the rain spray, are important in scaling the effects of rain from model tests: the density of water, kinematic viscosity of water, surface tension interactions of water, mean drop spacing, volumetric mean drop diameter, and drop velocity. The first three variables are inherent properties of water itself and the last three variables are dependent on the test technique used. The scaling parameters that are derived from the grouping of the aforementioned variables are Weber number (We), LWC, and R . The We is the ratio of inertial forces to surface tension forces and is a function of the density of water, drop velocity, volumetric mean

drop diameter, and the surface-tension interactions between water and air. The LWC is a function of the drop size distribution, drop velocity, and density of water. The R is a function of LWC. The sensitivity of the wet airfoil aerodynamic characteristics to each of the aforementioned parameters must be assessed.

This investigation assessed the sensitivity of a cambered, commercial transport-type airfoil equipped with high-lift devices to LWC and We . The sensitivity to LWC was assessed by varying the nozzle type, water injection pressure, volumetric flow rate, and the tunnel dynamic pressure. The sensitivity of the wet aerodynamic characteristics to Weber number, i.e., surface-tension interactions between water and air, also was addressed. A surface-tension reducing agent was added to the water in sufficient quantity (24 ml/gal of water) to reduce the surface tension by a factor of 2 (from 0.0047965 slug/sec² to 0.0021242 slug/sec²), which changed We by a factor of 2.

Data Accuracy

An internal, three-component, strain-gauge balance was used in this investigation to measure the aerodynamic forces and moments in and out of the simulated rain environment. This balance has an accuracy rating of ± 0.5 percent of full-scale loading. The calibration and corresponding error range for each component are as follows:

Component	Load	Error
Normal force, lb	± 600	± 3.0
Axial force, lb	± 100	± 0.5
Pitching moment, lb	± 2000	± 10

In aerodynamic coefficient form, the corresponding error range is as follows:

Aerodynamic coefficient	$q = 30$ psf	$q = 50$ psf
c_l	± 0.04	± 0.024
c_d	± 0.0067	± 0.004
c_m	± 0.053	± 0.032

Test Conditions

The location of the rain simulation system manifold 10 wing chord lengths upstream of the model and 6 in. above the model chord plane was chosen to mitigate any manifold-induced airflow disturbances. The data of reference 17 indicate the manifold upstream of the model location produced a slight increase in the free-stream turbulence level, in addition to a slight increase in drag. Comparisons of model aerodynamic data in and out of the simulated rain environment are with the manifold in position at all times.

During this investigation, no significant changes in dynamic pressure were measured at the model location in the simulated rain environment. Consequently, the calibrated dry air tunnel dynamic pressure was used to nondimensionalize the aerodynamic data obtained. All data shown were obtained with the boundary-layer transition fixed as discussed previously.

The tunnel dynamic pressure, angle of attack, and LWC conditions were parametrically varied to determine the performance degradation of the NACA 64-210 airfoil model equipped with and without high-lift devices. Aerodynamic measurements in and out of the simulated rain environment were obtained over an angle-of-attack range from 0° to 20° for dynamic pressures of 30 and 50 psf for the cruise configuration and an angle-of-attack range of 4° to 20° for dynamic pressures of 30 and 50 psf for the landing configuration. The rain intensity was varied to produce LWC values ranging from 16 to 46 g/m³. The sensitivity of the wet airfoil characteristics to water surface-tension interactions was also investigated for the landing configuration.

Presentation of Results

The results of this investigation have been reduced to coefficient form as presented in figures 14 through 37 and are listed in tabulated form in appendix B. The data were normalized with respect to the dry air dynamic pressure. The pitching-moment data were measured about the quarter-chord of the model. The data presented were obtained with the rain simulation system manifold in place. A listing of the data figures is as follows:

Reynolds number effect	14, 15
Cruise configuration lift curve and drag polar at $q = 30$ psf with LWC = 0, 25, and 39 g/m ³	16
Cruise configuration lift curve and drag polar at $q = 50$ psf with LWC = 0, 19, and 30 g/m ³	17
Cruise configuration drag as a function of angle of attack at $q = 30$ and 50 psf	18
Cruise configuration pitching moment versus lift and angle of attack at $q = 30$ and 50 psf	19
Water flow characteristics on upper surface of cruise configuration at $\alpha = 0^\circ$ and 20° and $q = 15$ psf with LWC = 17 g/m ³	23, 24
Water flow characteristics on lower surface of cruise configuration at $\alpha = 4^\circ$ and 16° and $q = 15$ psf with LWC = 14 g/m ³	25, 26
Landing configuration lift curve and drag polar at $q = 30$ psf with LWC = 0, 29, and 46 g/m ³	27
Landing configuration lift curve and drag polar at $q = 50$ psf with LWC = 0, 16, and 36 g/m ³	28
Landing configuration drag as function of angle of attack at $q = 30$ and 50 psf	29
Landing configuration pitching moment versus lift and angle of attack at $q = 30$ and 50 psf	30
Water flow characteristics on upper surface of landing configuration at $\alpha = 8^\circ$ and 20° and $q = 30$ psf with LWC = 46 g/m ³	32, 33
Water flow characteristics on lower surface of landing configuration at $\alpha = 4^\circ$ and 20° and $q = 30$ psf with LWC = 29 g/m ³	34, 35
Water surface tension effects on landing configuration aerodynamics at $q = 30$ psf	36
Water surface tension effects on landing configuration aerodynamics at $q = 50$ psf	37

Results and Discussion

Reynolds Number Effect

The dry aerodynamic data presented in figures 14 and 15 show the effect of Reynolds number at dynamic pressures of 30 and 50 psf for the cruise and landing configurations. The results indicate that Reynolds number had a negligible effect on lift coefficient versus angle of attack for both model configurations over the range tested. The data for both configurations also show small differences in the drag polar.

Cruise Configuration Aerodynamics

The effect of rain on the NACA 64-210 cruise configuration for $q = 30$ and 50 psf is shown in figures 16 and 17, respectively. Significant reductions in maximum lift were measured as LWC was increased, on the order of 8 and 11 percent at $q = 30$ psf (LWC = 25 and 39 g/m³) and 12 and 17 percent at $q = 50$ psf (LWC = 19 and 30 g/m³). A progressive decrease in the lift curve slope with increasing LWC was also observed for the cruise configuration (figs. 16 and 17). This effect may be explained by the observed water flow characteristics at low to moderate angles of attack discussed by Hastings et al. (ref. 18) and Hansman et al. (ref. 19). These characteristics were also observed during the present in-

vestigation and are discussed in detail later in this section.

The drag data at a constant lift condition do appear to be sensitive to LWC and dynamic pressure at and beyond stall. For example, the drag data in figure 16 for $q = 30$ psf and LWC = 25 g/m³ and $q = 50$ psf and LWC = 19 g/m³ in figure 17 show increases in drag coefficient at a constant lift coefficient of $c_l = 1.0$ of 37 and 71 percent, respectively. An increase in drag was measured for both dynamic pressures at low and moderate angles of attack as shown in figure 18. The drag data as a function of angle of attack and dynamic pressure do not appear to be as sensitive to increases in LWC as the lift data.

The effect of rain on pitching moment for the cruise configuration is shown in figures 19(a) and (b) for $q = 30$ and 50 psf. Prior to stall (fig. 19(b)), the effect of rain on pitching moment is negligible for both dynamic pressures. The change in the slope of the pitching-moment curve (fig. 19(a)) is marginal with increasing LWC for both dynamic pressures, although the break occurs earlier with a more pronounced effect with increasing LWC at a dynamic pressure of 50 psf.

The progressive decrease in the NACA 64-210 cruise configuration lift curve slope with increasing LWC may be explained by the water flow

characteristics observed during the present investigation. The photographic qualities of the rain spray were enhanced by the addition of a fluorescent dye to the water and the use of an ultraviolet strobe light in a darkened test section to capture the water flow patterns on the upper and lower surfaces of the airfoil. The surface blemishes on the upper and lower surfaces of the airfoil model are identified in figures 20 and 21 to make the reader aware that these blemishes will show up in an enhanced format during the visualization process.

The pattern of the water flow that develops can be qualitatively described in terms of an "ejecta fog" layer, water film layer, and "rivulet" flow field as sketched in figure 22(a). As the water droplets impact the leading edge of the airfoil at high speed, a layer of very fine droplets is formed in front of the leading edge as a consequence. This phenomenon has been defined as the "ejecta fog" layer. Beneath the ejecta fog layer, a water film layer develops at the wing leading edge and extends back toward the trailing edge along the upper and lower surfaces of the airfoil. At some point the water film layer breaks up into rivulets, which are thin capillary-like streams of water running chordwise toward the trailing edge of the airfoil.

The chordwise extent of the water film layer has been found to be dependent on the airfoil configuration, surface treatment, and angle of attack (refs. 18 and 19). As the angle of attack is increased, the chordwise extent of the water film layer decreases on the upper surface and increases on the lower surface as shown in figures 23 to 26 for the cruise configuration. Figures 23 and 24 were taken with an overhead camera and show the pattern of the water flow on the upper surface of the cruise configuration at $q = 15$ psf and $LWC = 17$ g/m³ for angles of attack of 0° and 20°, respectively. Photographs in figures 25 and 26 were taken with a camera located on the tunnel floor beneath the wing model and show the pattern of the water flow on the lower surface of the cruise configuration at $q = 15$ psf and $LWC = 14$ g/m³ for angles of attack of 4° and 16°, respectively. Note that the spanwise extent of the water film layer developing on the wing surface is limited to the width of the rain spray produced.

Focusing on the upper surface first, at $\alpha = 0^\circ$, the water film layer appears to extend back to approximately the 50-percent chordline before breaking up into rivulets (fig. 23). The presence of the rivulet field acts as the boundary for attached and separated flow. The rivulet field indicates attached flow at the low angles of attack. As the angle of attack is increased to 20°, the water film layer disappears

and the rivulet field highlights the separated flow regions present as shown in figure 24. On the lower surface, at $\alpha = 4^\circ$, the water film layer appears to extend back to approximately the 40-percent chordline before breaking up into rivulets (fig. 25). As the angle of attack increases, the chordwise extent of the water film increases until it encompasses the entire length of the airfoil. In figure 26 at $\alpha = 16^\circ$, the airfoil has stalled and the water film layer appears to extend back to approximately the 75-percent chordline before breaking up into rivulets. From visual observations, the rivulets on the lower surface appear to be pushed upward around the trailing edge and pooled on the upper surface. The cratering of the water film layer by droplet impacts and the break-up of the water film layer into rivulets simultaneously interact with the turbulent air boundary layer resulting in an early de-energization of the airfoil's boundary layer and hence, constantly changing the effective camber of the airfoil, which adversely affects the airfoil's performance throughout the entire angle-of-attack range.

In summary, the NACA 64-210 cruise configuration data presented in figures 16 through 19 indicated the same performance trends as the cruise configuration data of the NACA 0012 airfoil model previously cited in reference 8. Both airfoil sections exhibited significant reductions in maximum lift capability and increases in drag for a given lift condition in the simulated rain environment. The most significant difference between the cruise results of these two airfoil sections was the sensitivity of the NACA 64-210 airfoil section to LWC. This difference indicates that there is a rain effect sensitivity to camber. As previously mentioned, the NACA 0012 performance losses in the rain environment were not a function of LWC.

Landing Configuration Aerodynamics

The effects of rain on the NACA 64-210 landing configuration for $q = 30$ and 50 psf are shown in figures 27 and 28, respectively. The results obtained at stall for the landing configuration indicate that the LWC condition of 36 g/m³ at the higher dynamic pressure of 50 psf (fig. 28) produced almost as great a lift loss (18 percent) as the higher LWC condition of 46 g/m³ at the lower dynamic pressure of 30 psf (22 percent) (fig. 27). In addition, the greatest reduction in stall angle of attack (8°) was also measured at the higher dynamic pressure of 50 psf and $LWC = 36$ g/m³. Note that accompanying the reduction of the stall angle is the general flattening of the lift curve past stall with increasing LWC for both dynamic pressures. Similar to the cruise configuration data, the landing configuration

data also indicated a progressive decrease in the lift curve slope with increasing LWC. The same mechanism described in the cruise data section appears to be at work in this case.

Increases in drag were measured for both dynamic pressures at low and moderate angles of attack as shown in figures 27 and 28. The drag data at a constant lift condition do appear to be sensitive to LWC and test velocity. For example, the drag data for $q = 30$ psf (fig. 27) show increases in drag coefficient at a constant lift coefficient of $c_l = 2.3$ of 23 and 40 percent for $LWC = 29$ and 46 g/m^3 , respectively. At the higher dynamic pressure of 50 psf and the same lift coefficient of 2.3 (fig. 28), the drag data show increases of 14 and 15 percent for $LWC = 16$ and 36 g/m^3 , respectively. As was previously noted in the cruise configuration data, the landing configuration drag data as a function of angle of attack and dynamic pressure do not appear to be as sensitive to increases in LWC at low to moderate angles of attack as do the lift data (fig. 29).

The effect of rain on pitching moment for the landing configuration is shown in figures 30(a) and (b) for $q = 30$ and 50 psf. Prior to stall (fig. 30(a)), there appears to be a progressive increase in the slope of the pitching-moment curve with increasing LWC for both dynamic pressures. Similar to the cruise configuration data, the landing configuration data (fig. 30) also indicate the break in the pitching-moment curve occurs earlier with a more pronounced effect with increasing LWC at a dynamic pressure of 50 psf. Past stall, the rain environment continues to degrade pitching-moment performance at both dynamic pressures. The $q = 30$ psf pitching-moment data versus lift coefficient appear to be more sensitive to increases in LWC than the $q = 50$ psf pitching-moment data (fig. 30(b)).

The photographic coverage of the water flow characteristics on the upper and lower surfaces of the landing configuration indicates that for low to moderate angles of attack, where attached flow conditions exist, the water adheres to the airfoil surface forming a water film layer and a rivulet field. An additional flow complication is the presence of the high-lift devices (fig. 22(b)). The water passes through the gap openings between the high-lift devices and the main airfoil section and decreases the airflow through the gap openings. In figure 31, the landing configuration is shown immersed in the simulated rainfield. Figures 32 and 33 show the patterns of the water flow on the upper surface of the landing configuration at $q = 30$ psf and $LWC = 46 \text{ g/m}^3$ for angles of attack of 8° and 20° , respectively. Figures 34 and 35 show

the water patterns on the lower surface of the landing configuration at $q = 30$ psf and $LWC = 29 \text{ g/m}^3$ for angles of attack of 4° and 20° .

Focusing on the upper surface at $\alpha = 8^\circ$ (fig. 32), two interactions can be seen: the formation of a rivulet field on the main airfoil section and the water being driven upward from the underside of each high-lift device (leading-edge slat and trailing-edge double-slotted flaps) through the gap openings onto the upper surfaces of the adjacent airfoil element. As the angle of attack increases, the presence of the water reduces the gap openings, which alters the separated airflow regions on the upper surface of the airfoil and causes a breakdown of the water flow pattern, which results in regional pooling of the water, as shown in figure 33 at $\alpha = 20^\circ$. On the lower surface at $\alpha = 4^\circ$ (fig. 34), the water film layer extends back to approximately the 90-percent chordline on the main airfoil section. As the angle of attack increases, the slat and flap mounting brackets block some of the water flow as indicated by the nearly dry areas on the main airfoil section and flap system aft of the brackets shown in figures 33 and 35. At $\alpha = 20^\circ$, the water film layer extends back to the trailing edge of the main airfoil section (fig. 35) and from visual observations the gap openings of all the high-lift devices appear to be significantly immersed with water. In figure 35, a sheet of water appears to be coming from the underside of the wing, through the flap gap opening, and outward in the direction of the free-stream flow. The photographic coverage indicates that the large amount of water that flowed through the gaps played a significant role in the performance losses experienced by the landing configuration.

In summary, although reductions in maximum lift capability and corresponding increases in drag were measured for both the cruise and landing configurations of the NACA 64-210 airfoil model, the landing configuration was more sensitive to the rain environment than the cruise configuration. Of particular significance was the associated decrease in the angle of attack at which maximum lift occurred with increasing LWC. Accompanying the reduction of the stall angle of attack was the general flattening of the lift curve slope past stall. The severity of the rain effect appears to be dependent on test velocity and LWC.

Surface Tension Effects

The wetted aerodynamic characteristics of the landing configuration are shown in figures 36 and 37 with and without the surface-tension reducing agent added to the water at dynamic pressures of 30

and 50 psf. The addition of the surface-tension reducing agent changes the chemical properties of the water, which allows the water droplets to shatter and "wet" the airfoil surface (spread outward in a thin film) more easily. This aspect of the investigation is a first-cut attempt at discovering the effect of surface tension as identified by Bilanin (ref. 16) on the heavy rain phenomenon. The addition of the chemical reduced the surface tension of water by a factor of 2 (from 0.0047965 slug/sec² to 0.0021242 slug/sec²) which resulted in increasing the Weber number by a factor of 2.

The data of figures 36 and 37 for the treated rain spray indicate the same trends in maximum lift coefficient, angle of attack for maximum lift, and drag coefficient as the data for the untreated rain spray. Although the data do indicate a slight decrease in lift at both dynamic pressures for the treated water conditions, the maximum lift attained is approximately the same. The data of reference 19, which reduced the surface tension of water by the same factor as in these tests, showed that surface tension had a strong influence on the lift capability of laminar flow airfoils subjected to the treated rain spray; however, the data of the present investigation indicate that small-scale model testing of high-lift configurations having little or no laminar flow (recall that transition was fixed at the 5-percent chordline) is not strongly dependent on surface tension effects.

Summary of Results

The objective of the present investigation was threefold: first, to determine the severity of the rain effect on a cambered airfoil representative of typical commercial transport wing sections; second, to determine the aerodynamic penalty over a wider range of rain intensities; and third, to explore the importance of surface tension interactions of water as a scaling parameter.

In preparation for this investigation, a hypodermic nozzle was developed that provided the flexibility to independently vary the rain intensity while retaining control over the drop size. A 5- and 7-tube configuration of the hypodermic nozzle along with a fan jet nozzle were each used separately (no mixing of nozzle type) in the present investigation to vary the rain intensity. The 5-tube configuration of the hypodermic nozzle produced the lowest rain intensity and the fan jet nozzle produced the highest rain intensity. The wind tunnel rain system simulated a thunderstorm-type rain ranging from 16 to 46 g/m³.

The aerodynamic data presented in this report were obtained in the Langley 14- by 22-Foot Subsonic Tunnel at dynamic pressures of 30 and 50 psf

on a cambered wing having an NACA 64-210 airfoil section with leading- and trailing-edge high-lift devices tested in cruise and landing configurations. The NACA 64-210 cruise data indicated the same performance trends as the cruise data of the NACA 0012 airfoil model tested during the exploratory wind tunnel study cited in reference 8. Both airfoil sections exhibited significant reductions in maximum lift capability and increases in drag for a given lift condition at both dynamic pressures. The most significant difference between the cruise results of these two airfoil sections was the sensitivity of the NACA 64-210 airfoil section to liquid water content (LWC). Significant reductions in maximum lift and a progressive decrease in the lift curve slope were measured as LWC was increased for the NACA 64-210 cruise configuration. This difference indicates that there is a rain effect sensitivity to camber.

The NACA 64-210 high-lift airfoil geometry was representative of typical commercial transport wing sections. The landing configuration experienced substantial reductions in maximum lift capability with increasing LWC and an associated decrease in the angle of attack at which maximum lift occurred, as well as increases in drag at constant lift. Accompanying the reduction of the stall angle was the general flattening of the lift curve past stall as LWC was increased. The NACA 64-210 data indicate the severity of the rain effect appears to be configuration-dependent and is most severe for high-lift configuration airfoils with leading- and trailing-edge devices deflected for landing or take-off operations.

Prior to stall, there appears to be a progressive decrease in the lift curve slope for both model configurations at both dynamic pressures. There also appears to be a progressive increase in the slope of the pitching-moment curve with increasing LWC for the landing configuration. Although the change in the slope of the pitching-moment curve for the cruise configuration is marginal, the break in the pitching-moment curve occurs earlier with a more pronounced effect with increasing LWC at a dynamic pressure of 50 psf for both model configurations.

Photographic coverage of the water flow characteristics on the upper and lower surfaces of both model configurations indicates that for low to moderate angles of attack, where attached flow conditions exist, the water adheres to the airfoil surface and forms a water film layer and a rivulet field. The interactions of the droplet impacts, water film layer, and rivulet field appear to change the effective camber of the airfoil, adversely affecting the airfoil's performance throughout the entire angle-of-attack range. For the landing configuration, the presence of the

high-lift devices created an additional flow complication. The water passed through the gap openings between the high-lift devices and the main airfoil section and decreased the airflow through the gap openings. The landing configuration results indicate that the large amount of water that flowed through the gaps significantly reduced the efficiency of the high-lift devices.

Experiments conducted with a surface-tension reducing agent in the rain spray did not show the anticipated influence of surface tension on lift for the

fully turbulent, high-lift configuration tested. In order to fully understand the significance of the various mechanisms involved in the generation of lift in a two-phase flow with separated flow conditions, considerable analytical and experimental research is required.

NASA Langley Research Center
Hampton, VA 23681-0001
June 4, 1992

Appendix A Scaling of Rain

For natural rain, a relationship between liquid water content (LWC), drop size distribution, and rain rate was developed by Marshall and Palmer (ref. 14) in 1947 on the basis of experimental results. The study showed that the size distribution of rain in a cloud could be estimated with an exponential expression of the form

$$N(D) = N_o e^{-ID} \quad (\text{A1})$$

where $N(D)$ is the drop size distribution, or density function, in terms of the number of drops per cubic meter of air per unit interval of time, D is the drop diameter, and $I = nR^m$, where n , m , and N_o are empirically determined constants, and R is rainfall rate in mm/hr. Data from reference 15 indicated that $N_o = 8000$, $n = 4.1$, and $m = -0.21$ for light continuous rain. More recent studies (ref. 13) have shown that the values of N_o , n , and m are dependent upon storm type and intensity. Reference 13, for example, suggests that the distribution of heavy thunderstorm-type rain is best characterized by $N_o = 1400$, $n = 3.0$, and $m = -0.21$.

The drop size distribution is used to determine the LWC as a function of rain rate. The LWC is the integrated sum of the mass of each drop multiplied by the number of drops of each size per unit volume as follows:

$$\text{LWC} = \int_0^{\infty} \rho_w \frac{\pi}{6} D^3 N(D) dD \quad (\text{A2})$$

where ρ_w is the density of water. When the integration is performed this expression becomes

$$\text{LWC} = \frac{N_o \rho_w \pi}{I^4} \quad (\text{A3})$$

Substituting $I = nR^m$, then

$$\text{LWC} = \frac{N_o \rho_w \pi}{n^4 R^{4m}} \quad (\text{A4})$$

Using the aforementioned expression for the drop size distribution for thunderstorm-type rain, the LWC in g/m^3 is related to rainfall rate by

$$\text{LWC} = \frac{1400\pi 10^{-3}}{3^4 R^{-0.84}} = 0.054 R^{0.84} \quad (\text{A5})$$

Substituting the expression for drop size distribution for light widespread rain into equation (A2), the equation for LWC in terms of rainfall rate becomes

$$\text{LWC} = \frac{8000\pi 10^{-3}}{(4.1)^4 R^{-0.84}} = 0.08894 R^{0.84} \quad (\text{A6})$$

Figure A1 is a plot of the LWC as a function of rainfall rate for both light widespread rain and thunderstorm-type rain. Rain is adequately modeled by equations (A1), (A5), and (A6) when the type of rain environment is specified (thunderstorm or continuous) and either the LWC or rainfall rate is given.

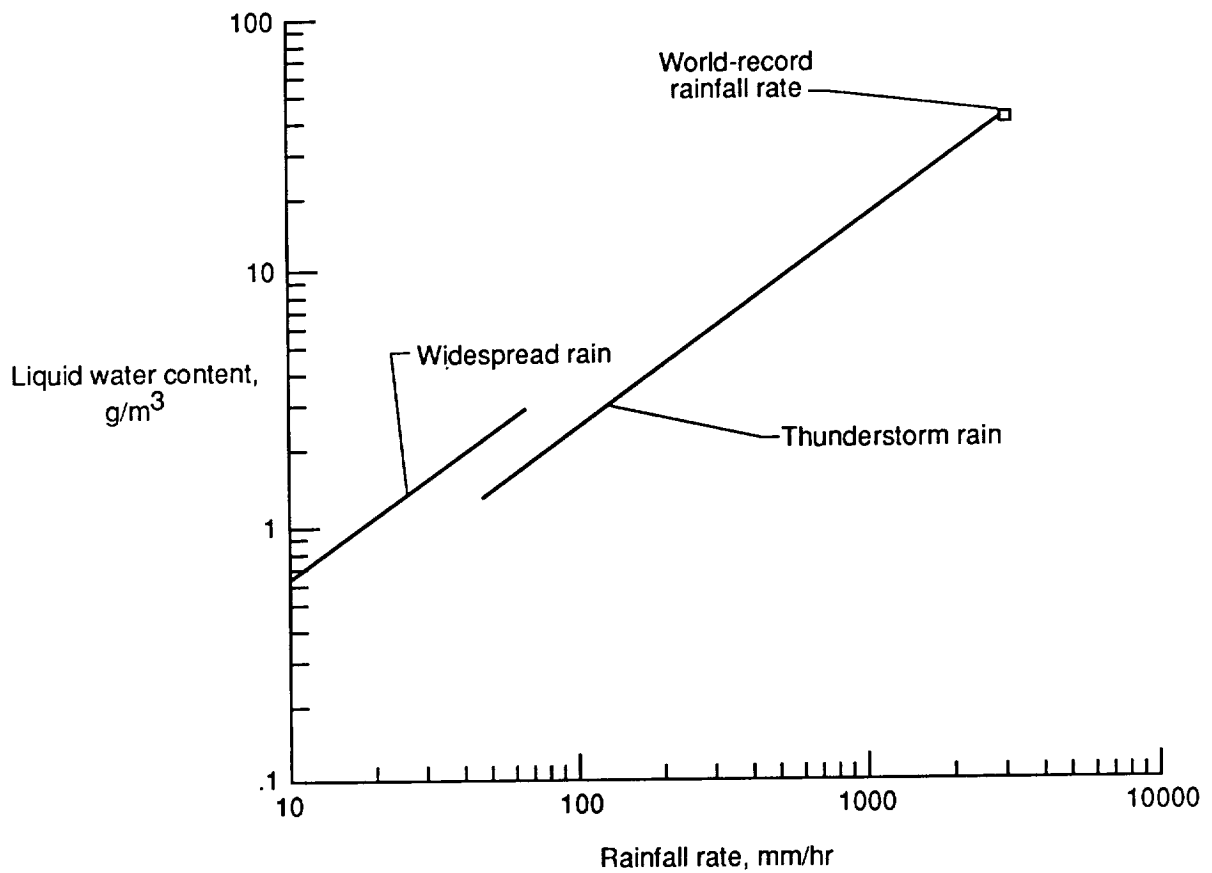


Figure A1. Liquid water content versus rainfall rate for widespread rain and thunderstorm rain.

Appendix B

Tabulated Data

Tables B1 and B2 present cruise and landing configuration data in coefficient form for dynamic pressures of 30 and 50 psf and an LWC range of 16 to 46 g/m³. Table B3 presents the landing configuration data in coefficient form with surface tension effects for dynamic pressures of 30 and 50 psf and an LWC range of 22 to 44 g/m³.

Table B1. NACA 64-210 Cruise Configuration

(a) $q = 30$ psf

LWC, g/m ³	α , deg	c_l	c_d	c_m
0	0.000	0.162	0.010	-0.034
	2.030	0.336	0.016	-0.037
	4.039	0.508	0.025	-0.038
	6.086	0.680	0.037	-0.039
	8.059	0.840	0.050	-0.040
	10.020	1.003	0.068	-0.041
	12.007	1.145	0.088	-0.041
	13.003	1.207	0.100	-0.040
	14.033	1.165	0.189	-0.058
	15.085	1.121	0.231	-0.096
	16.092	1.080	0.235	-0.100
	18.020	1.076	0.342	-0.136
	20.064	1.036	0.401	-0.158
	25	0.004	0.155	0.019
2.072		0.326	0.025	-0.035
4.035		0.484	0.032	-0.036
6.077		0.658	0.046	-0.037
8.124		0.812	0.062	-0.039
10.090		0.952	0.082	-0.039
12.050		1.064	0.103	-0.040
13.001		1.101	0.139	-0.047
14.020		1.073	0.214	-0.088
15.054		1.020	0.274	-0.116
16.062		1.030	0.280	-0.106
18.002		0.949	0.358	-0.140
20.063		0.894	0.410	-0.150
39		0.036	0.146	0.021
	2.054	0.315	0.028	-0.034
	4.005	0.478	0.036	-0.036
	6.067	0.639	0.046	-0.037
	8.038	0.793	0.063	-0.037
	10.051	0.928	0.080	-0.038
	12.061	1.023	0.109	-0.043
	13.057	1.061	0.158	-0.057
	14.022	1.024	0.231	-0.098
	14.998	0.942	0.267	-0.115
	16.037	0.923	0.308	-0.131
	18.041	0.868	0.347	-0.137
	20.016	0.823	0.383	-0.137

(b) $q = 50$ psf

LWC, g/m ³	α , deg	c_l	c_d	c_m
0	0.000	0.161	0.009	-0.036
	2.009	0.338	0.013	-0.038
	3.997	0.511	0.020	-0.039
	5.997	0.684	0.030	-0.040
	8.081	0.858	0.043	-0.041
	10.075	1.018	0.060	-0.041
	12.077	1.160	0.078	-0.039
	13.038	1.211	0.093	-0.039
	14.050	1.156	0.140	-0.050
	15.091	1.114	0.169	-0.070
	16.043	1.102	0.227	-0.092
	18.099	1.063	0.310	-0.124
	20.064	0.973	0.358	-0.134
	19	0.000	0.160	0.016
2.006		0.326	0.019	-0.035
4.016		0.492	0.026	-0.037
6.007		0.659	0.037	-0.038
8.025		0.818	0.052	-0.038
10.087		0.952	0.073	-0.039
12.036		1.046	0.127	-0.050
13.022		1.065	0.173	-0.079
13.994		1.031	0.227	-0.105
14.990		0.964	0.263	-0.123
30	0.000	0.153	0.018	-0.032
	2.036	0.325	0.020	-0.034
	4.025	0.485	0.027	-0.036
	6.020	0.647	0.039	-0.037
	8.020	0.799	0.055	-0.038
	10.024	0.915	0.079	-0.041
	12.071	1.010	0.143	-0.061
	13.067	0.995	0.204	-0.096
	13.989	0.965	0.242	-0.112
	15.000	0.941	0.272	-0.124
16.027	0.920	0.298	-0.133	
18.071	0.857	0.339	-0.137	
20.170	0.805	0.362	-0.130	

Table B2. NACA 64-210 Landing Configuration

(a) $q = 30$ psf

(b) $q = 50$ psf

LWC, g/m ³	α , deg	c_l	c_d	c_m
0	4.024	2.195	0.158	-0.431
	6.111	2.386	0.188	-0.413
	8.018	2.530	0.216	-0.392
	10.056	2.686	0.250	-0.370
	11.973	2.827	0.286	-0.351
	13.945	2.951	0.329	-0.325
	16.022	3.024	0.368	-0.292
	17.936	3.019	0.396	-0.257
	20.240	2.864	0.408	-0.185
29	4.047	2.126	0.193	-0.414
	6.064	2.291	0.230	-0.397
	8.064	2.463	0.271	-0.378
	10.085	2.580	0.308	-0.356
	12.078	2.702	0.344	-0.333
	14.201	2.779	0.368	-0.237
	16.049	2.742	0.391	-0.248
	18.094	2.677	0.411	-0.204
	20.078	2.440	0.472	-0.256
46	4.041	2.094	0.194	-0.405
	6.064	2.232	0.230	-0.380
	8.073	2.330	0.263	-0.353
	10.171	2.437	0.290	-0.316
	12.284	2.345	0.294	-0.248
	14.250	2.375	0.310	-0.220
	16.076	2.357	0.356	-0.229
	18.112	2.303	0.421	-0.244
	20.026	2.332	0.471	-0.266

LWC, g/m ³	α , deg	c_l	c_d	c_m
0	4.038	2.146	0.155	-0.405
	6.024	2.344	0.163	-0.393
	8.065	2.500	0.196	-0.373
	10.028	2.666	0.233	-0.356
	12.003	2.809	0.272	-0.339
	14.078	2.922	0.300	-0.311
	16.029	2.988	0.345	-0.286
	17.929	3.024	0.393	-0.267
	19.962	2.863	0.442	-0.240
16	3.999	2.168	0.157	-0.405
	6.016	2.344	0.187	-0.390
	8.039	2.509	0.218	-0.370
	10.049	2.659	0.251	-0.350
	12.031	2.781	0.284	-0.326
	14.151	2.674	0.290	-0.244
	16.165	2.712	0.324	-0.216
	18.015	2.867	0.404	-0.239
	19.961	2.523	0.476	-0.278
36	4.030	2.133	0.157	-0.400
	6.034	2.299	0.187	-0.382
	8.026	2.448	0.217	-0.362
	10.101	2.597	0.250	-0.341
	12.172	2.598	0.265	-0.275
	14.172	2.560	0.284	-0.225
	16.120	2.631	0.325	-0.216
	18.162	2.474	0.418	-0.255
	19.851	2.474	0.478	-0.266

Table B3. NACA 64-210 Landing Configuration With Surface Tension Effects

(a) $q = 30$ psf

LWC, g/m ³	α , deg	c_l	c_d	c_m
27	8.046	2.400	0.252	-0.386
	10.062	2.533	0.284	-0.364
	12.021	2.654	0.318	-0.337
	16.082	2.696	0.354	-0.257
44	8.064	2.331	0.273	-0.369
	10.075	2.468	0.306	-0.344
	12.145	2.363	0.301	-0.250
	16.177	2.476	0.353	-0.208

(b) $q = 50$ psf

LWC, g/m ³	α , deg	c_l	c_d	c_m
22	8.023	2.424	0.233	-0.376
	10.033	2.572	0.265	-0.357
	12.032	2.699	0.315	-0.340
	16.086	2.689	0.349	-0.234
35	8.051	2.369	0.250	-0.361
	12.209	2.494	0.296	-0.270
	16.166	2.615	0.330	-0.213

References

1. *Low-Altitude Wind Shear and Its Hazard to Aviation*. National Academy Press, 1983.
2. Riordan, Pauline: *Weather Extremes Around the World*. Tech. Rep. 70-45-ES, U.S. Army, Jan. 1970. (Available from DTIC as AD 707 920.)
3. Roys, George P.; and Kessler, Edwin: Measurements by Aircraft of Condensed Water in Great Plains Thunderstorms. Tech. Note 49-NSSP-19, U.S. Dep. of Commerce, July 1966.
4. Melson, W. Edward, Jr.: Heavy Rain Characteristics and Ground Measurement Comparisons. Paper presented at the WMO IAHS 8th International Workshop on Precipitation Measurement (St. Moritz, Switzerland), Dec. 4-7, 1989.
5. Melson, W. Edward, Jr.: Observation and Comparison of Rainfall Measured at a High Sample Rate. Paper presented at the American Meteorological Society 71st Annual Meeting (New Orleans, Louisiana), Jan. 13-18, 1991.
6. Rhode, Richard V.: *Some Effects of Rainfall on Flight of Airplanes and on Instrument Indications*. NACA TN 803, 1941.
7. Haines, P. A.; and Luers, J. K.: *Aerodynamic Penalties of Heavy Rain on a Landing Aircraft*. NASA CR-156885, 1982.
8. Dunham, R. E., Jr.: Potential Influences of Heavy Rain on General Aviation Airplane Performance. AIAA-86-2606, Sept. Oct. 1986.
9. Gentry, Garl L., Jr.; Quinto, P. Frank; Gatlin, Gregory M.; and Applin, Zachary T.: *The Langley 14-by 22-Foot Subsonic Tunnel: Description, Flow Characteristics, and Guide for Users*. NASA TP-3008, 1990.
10. Braslow, Albert L.; Hicks, Raymond M.; and Harris, Roy V., Jr.: *Use of Grit-Type Boundary-Layer-Transition Trips on Wind-Tunnel Models*. NASA TN D-3579, 1966.
11. Booker, J. D.; and Nash, M. J. B.: *Facilities at R.A.E. for the Simulation of Flight Through Rain*. RAE-TR-67245, British Royal Aircraft Establ., Oct. 1967.
12. Hernan, M. A.; Gharib, M.; Parikh, P.; and Sarohia, V.: *Simulation and Analysis of Natural Rain in a Wind Tunnel Via Digital Image Processing Techniques Interim Report*. JPL D-2231 (Contract NAS7-918, Task Order RE 65/Amendment 459), California Inst. of Technology, Oct. 31, 1984.
13. Markowitz, Allan H.: Raindrop Size Distribution Expressions. *J. Appl. Meteorol.*, vol. 15, no. 9, Sept. 1976, pp. 1029-1031.
14. Marshall, J. S.; and Palmer, W. McK.: The Distribution of Raindrops With Size. *J. Meteorol.*, vol. 5, no. 4, Aug. 1948, pp. 165-166.
15. Joss, J.; and Waldvogel, A.: Raindrop Size Distribution and Sampling Size Errors. *J. Atmos. Sci.*, vol. 26, no. 3, May 1969, pp. 566-569.
16. Bilanin, Alan J.: Scaling Laws for Testing of High Lift Airfoils Under Heavy Rainfall. AIAA-85-0257, Jan. 1985.
17. Campbell, Bryan A.; and Bezos, Gaudy M.: *Steady-State and Transitional Aerodynamic Characteristics of a Wing in Simulated Heavy Rain*. NASA TP-2932, 1989.
18. Hastings, E. C., Jr.; and Manuel, G. S.: Measurements of Water Film Characteristics on Airfoil Surfaces From Wind-Tunnel Tests With Simulated Heavy Rain. AIAA-85-0259, Jan. 1985.
19. Hansman, R. John, Jr.; and Barsotti, Martitia F.: The Aerodynamic Effect of Surface Wetting Characteristics on a Laminar Flow Airfoil in Simulated Heavy Rain. AIAA-85-0260, Jan. 1985.

Table 1. Model Coordinates

[NACA 64-210]

(a) Cruise configuration, $c = 2.5$ ft (cruise chord)

Upper surface		Lower surface	
$100 \times \frac{x}{c}$	$100 \times \frac{z}{c}$	$100 \times \frac{x}{c}$	$100 \times \frac{z}{c}$
0	0	0	0
.431	.867	.569	-.767
.673	1.056	.827	-.916
1.163	1.354	1.337	-1.140
2.401	1.884	2.599	-1.512
4.890	2.656	5.110	-2.024
7.387	3.248	7.613	-2.400
9.887	3.736	10.113	-2.702
14.894	4.514	15.106	-3.168
19.905	5.097	20.095	-3.505
24.919	5.533	25.081	-3.743
29.934	5.836	30.066	-3.892
34.951	6.010	35.049	-3.950
39.968	6.059	40.032	-3.917
44.985	5.938	45.015	-3.748
50.000	5.689	50.000	-3.483
55.014	5.333	54.987	-3.143
60.025	4.891	59.975	-2.749
65.033	4.375	64.967	-2.315
70.038	3.799	69.962	-1.855
75.040	3.176	74.960	-1.386
80.038	2.518	79.962	-.926
85.033	1.849	84.968	-.503
90.024	1.188	89.977	-.154
95.012	.564	94.988	.068
100.000	0	100.000	0
L.E. radius: 0.720			
Slope of radius through L.E.: 0.084			

Table 1. Continued

(b) High-lift configuration, $c = 2.5$ ft (cruise chord)

Leading-edge slat				Main wing section			
Upper surface		Lower surface		Upper surface		Lower surface	
$\frac{x}{c}$	$\frac{z}{c}$	$\frac{x}{c}$	$\frac{z}{c}$	$\frac{x}{c}$	$\frac{z}{c}$	$\frac{x}{c}$	$\frac{z}{c}$
0.00083	0.00291	0.10848	-0.00047	0.00431	0.00814	0.79781	0.00000
.00312	.00485	.10323	.00057	.01379	.01404	.78175	-.00002
.00731	.00676	.09684	.00118	.03015	.02306	.76573	-.00210
.01250	.00819	.08961	.00135	.04749	.03015	.75204	-.00678
.01691	.00887	.08145	.00125	.07194	.03753	.73722	-.02441
.02128	.00921	.07411	.00104	.09049	.04172	.72283	-.03496
.02570	.00937	.06821	.00064	.11205	.04419	.71036	-.03562
.03049	.00942	.06207	-.00073	.14300	.04719	.67886	-.03735
.03673	.00927	.05569	-.00322	.17552	.04974	.63670	-.03973
.04342	.00892	.04974	-.00635	.20927	.05172	.59557	-.04187
.04974	.00850	.04342	-.01132	.24322	.05309	.55605	-.04371
.05569	.00804	.03673	-.01630	.27761	.05387	.51840	-.04520
.06207	.00733	.03049	-.02011	.31216	.05404	.48235	-.04634
.06821	.00659	.02570	-.02219	.34677	.05362	.44662	-.04707
.07411	.00587	.02128	-.02260	.37965	.05267	.41222	-.04735
.08145	.00493	.01691	-.02165	.41222	.05093	.37965	-.04717
.08961	.00379	.01250	-.01848	.44662	.04845	.34677	-.04632
.09684	.00264	.00731	-.01414	.48235	.04527	.31216	-.04498
.10323	.00148	.00312	-.00972	.51840	.04149	.27761	-.04321
.10882	.00047	.00083	-.00511	.55605	.03705	.24322	-.04100
		.00000	.00000	.59557	.03192	.20927	.03841
				.63670	.02608	.17552	-.03543
				.67886	.01968	.14300	-.03210
				.71036	.01467	.11205	-.02847
				.72283	.01263	.09049	-.02562
				.73722	.01026	.07194	-.02293
				.75204	.00779	.04749	-.01885
				.76573	.00548	.03015	-.01549
				.78175	.00275	.01379	-.01212
				.79781	.00000	.00431	-.00782
						.00000	.00000

Table 1. Concluded

(b) Concluded

Trailing-edge vane				Trailing-edge flap			
Upper surface		Lower surface		Upper surface		Lower surface	
$\frac{x}{c}$	$\frac{z}{c}$	$\frac{x}{c}$	$\frac{z}{c}$	$\frac{x}{c}$	$\frac{z}{c}$	$\frac{x}{c}$	$\frac{z}{c}$
0.00033	0.00300	0.08148	-0.00053	0.00070	0.00297	0.21477	-0.00050
.00145	.00597	.07763	.00044	.00409	.00657	.20610	.00013
.00339	.00837	.07293	.00142	.00930	.01087	.19632	.00052
.00561	.01034	.06760	.00234	.01635	.01422	.18542	.00070
.00833	.01174	.06189	.00319	.02464	.01696	.17336	.00069
.01141	.01269	.05600	.00397	.03409	.01867	.16015	.00049
.01554	.01347	.05015	.00435	.04482	.01965	.14580	.00015
.02049	.01399	.04523	.00428	.05684	.02001	.13040	-.00021
.02531	.01410	.04018	.00379	.06947	.01956	.11412	-.00064
.03018	.01393	.03513	.00286	.08153	.01887	.09728	-.00112
.03513	.01354	.03018	.00150	.09728	.01860	.08153	-.00162
.04018	.01296	.02531	-.00038	.11412	.01800	.06947	-.00204
.04523	.01203	.02049	-.00292	.13040	.01709	.05684	-.00253
.05015	.01100	.01554	-.00608	.14580	.01587	.04482	-.00305
.05600	.00969	.01141	-.00840	.16015	.01434	.03409	-.00357
.06189	.00823	.00833	-.00898	.17336	.01246	.02464	-.00406
.06760	.00659	.00561	-.00842	.18542	.01020	.01635	-.00449
.07293	.00476	.00339	-.00720	.19632	.00751	.00930	-.00460
.07763	.00276	.00145	-.00492	.20610	.00430	.00409	-.00394
.08174	.00053	.00033	-.00246	.21478	.00050	.00070	-.00217
		.00000	.00000			.00000	.00000

Table 2. Simulated Rain Characteristics

[D_1 = Arithmetic mean diameter;]
 [D_2 = Volumetric mean diameter]

(a) Droplet diameter characteristics

Hypodermic nozzle			Commercial fan jet nozzle		
Dynamic pressure, psf	Supply pressure, psi	Mean diameter, mm	Dynamic pressure, psf	Supply pressure, psi	Mean diameter, mm
15	80	$D_1 = 0.9$ $D_2 = 2.6$	30	50	$D_1 = 0.72$ $D_2 = 2.08$
30	80	$D_1 = 1.0$ $D_2 = 2.47$	70	70	$D_1 = 0.47$ $D_2 = 1.12$
50	80	$D_1 = 0.55$ $D_2 = 1.44$			

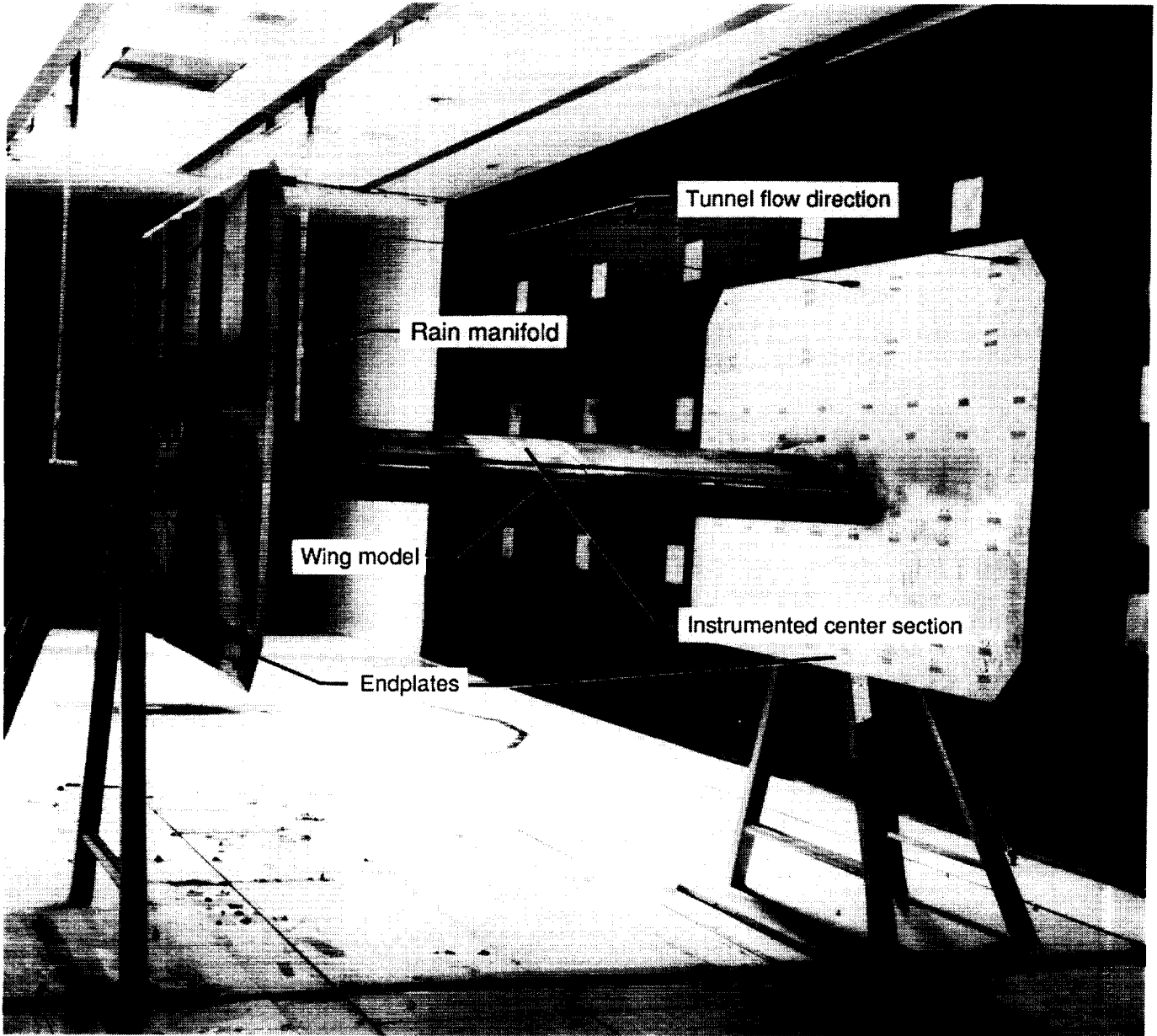
(b) Droplet velocity characteristics

Nozzle type	Dynamic pressure, psf	Free-stream velocity, ft/sec	Ratio of mean drop velocity to free-stream velocity
Hypodermic	15	112	0.92
	30	159	0.89

(c) Rain system performance characteristics

Nozzle type	Dynamic pressure, psf	Air supply pressure, psi	Avg. volumetric flow rate, gal/min	Spray area, ft ²
5-tube	15	80	13	16
	30, 50	80	13	9
7-tube	30, 50	80	19	9
Fan jet	30, 50	70	33	10

ORIGINAL PAGE
BLACK AND WHITE PHOTOGRAPH



L-84-4279

Figure 1. View of test setup looking upstream in Langley 14- by 22-Foot Subsonic Tunnel.

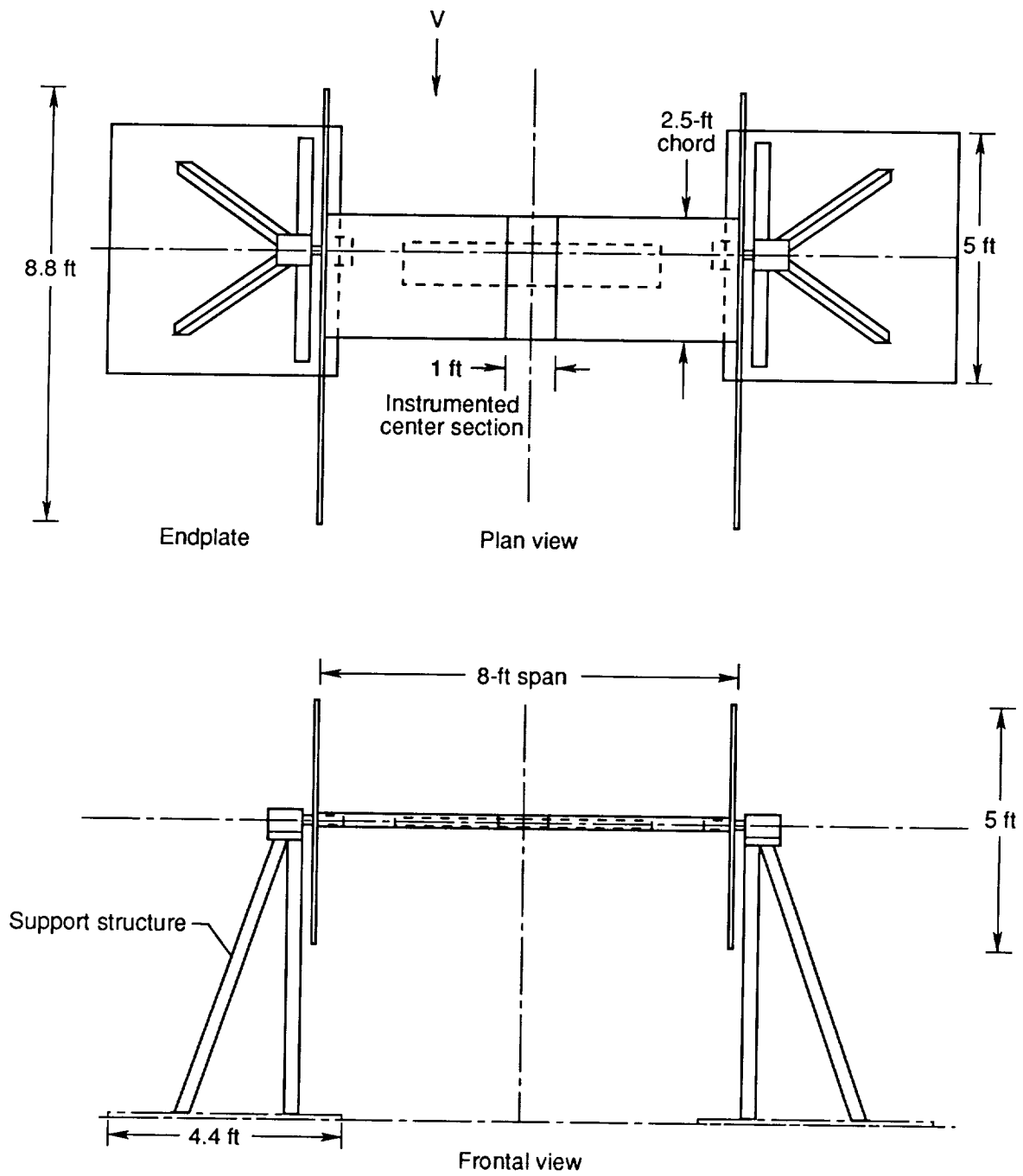


Figure 2. Plan and frontal views of model and support apparatus.

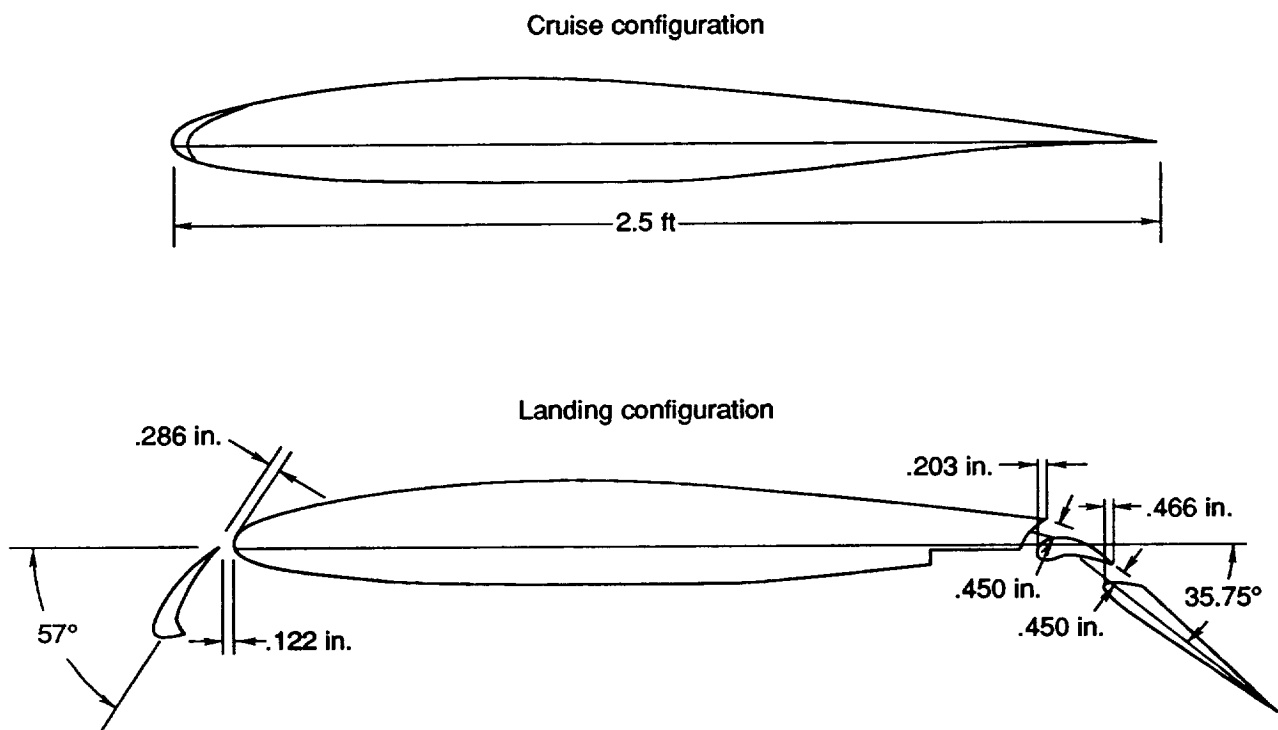
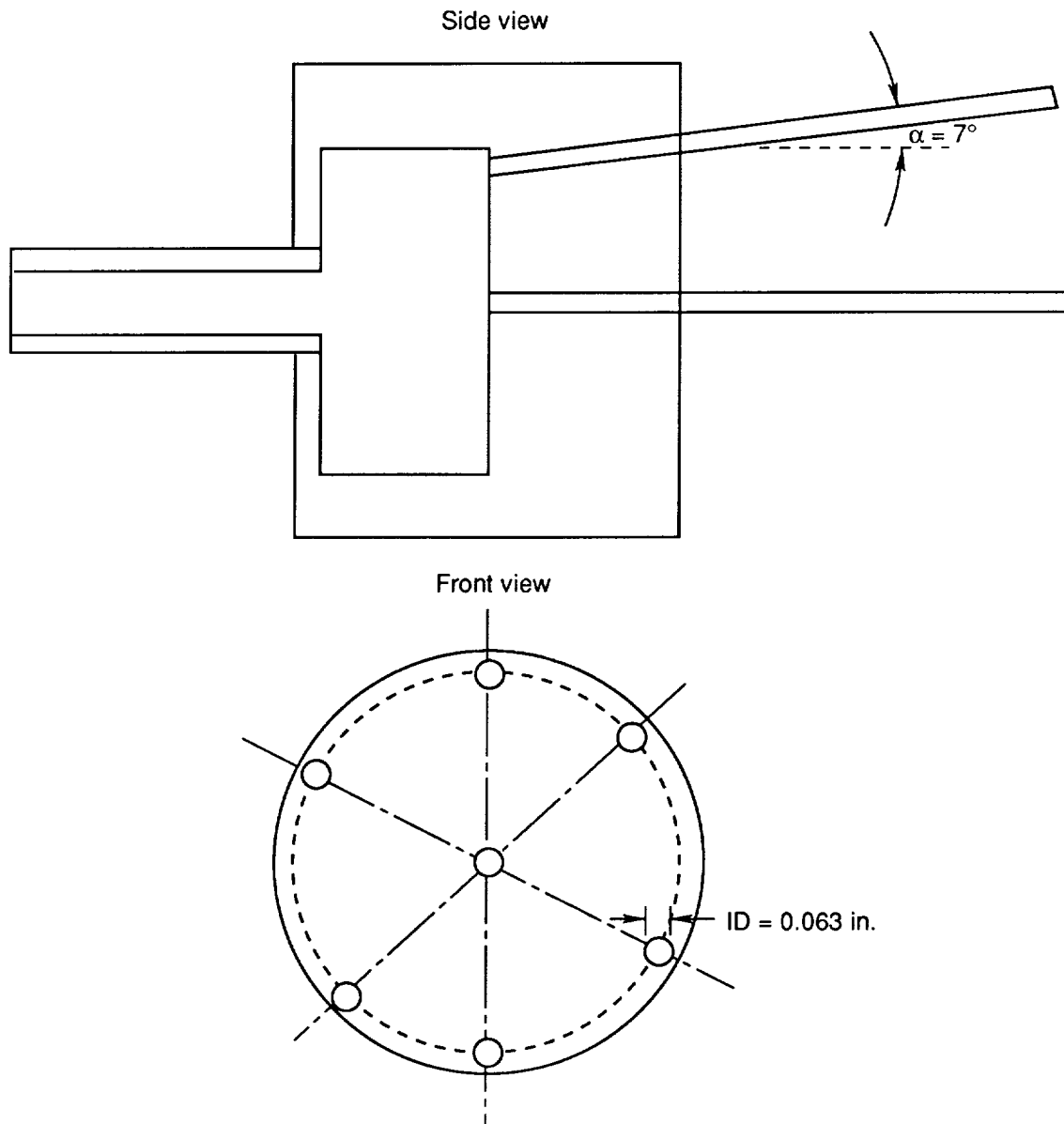


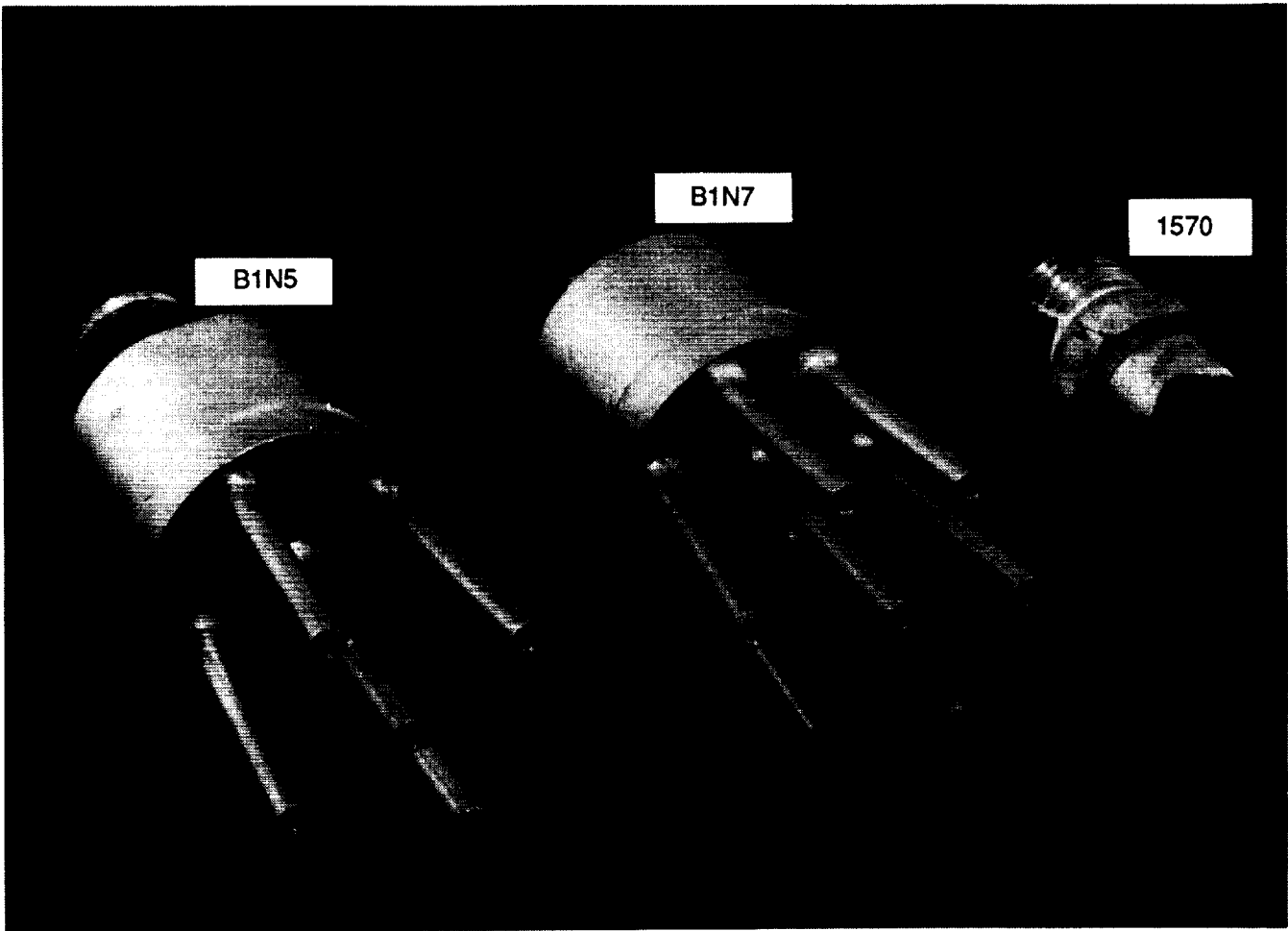
Figure 3. Cross sections of cruise and landing configurations of NACA 64-210 airfoil model.



(a) Details of JPL-designed hypodermic nozzle.

Figure 4. Nozzle hardware used in simulation of rain in Langley 14- by 22-Foot Subsonic Tunnel.

ORIGINAL PAGE
BLACK AND WHITE PHOTOGRAPH



L-84-12276

(b) Three nozzles used to vary rain spray characteristics.

Figure 4. Concluded.

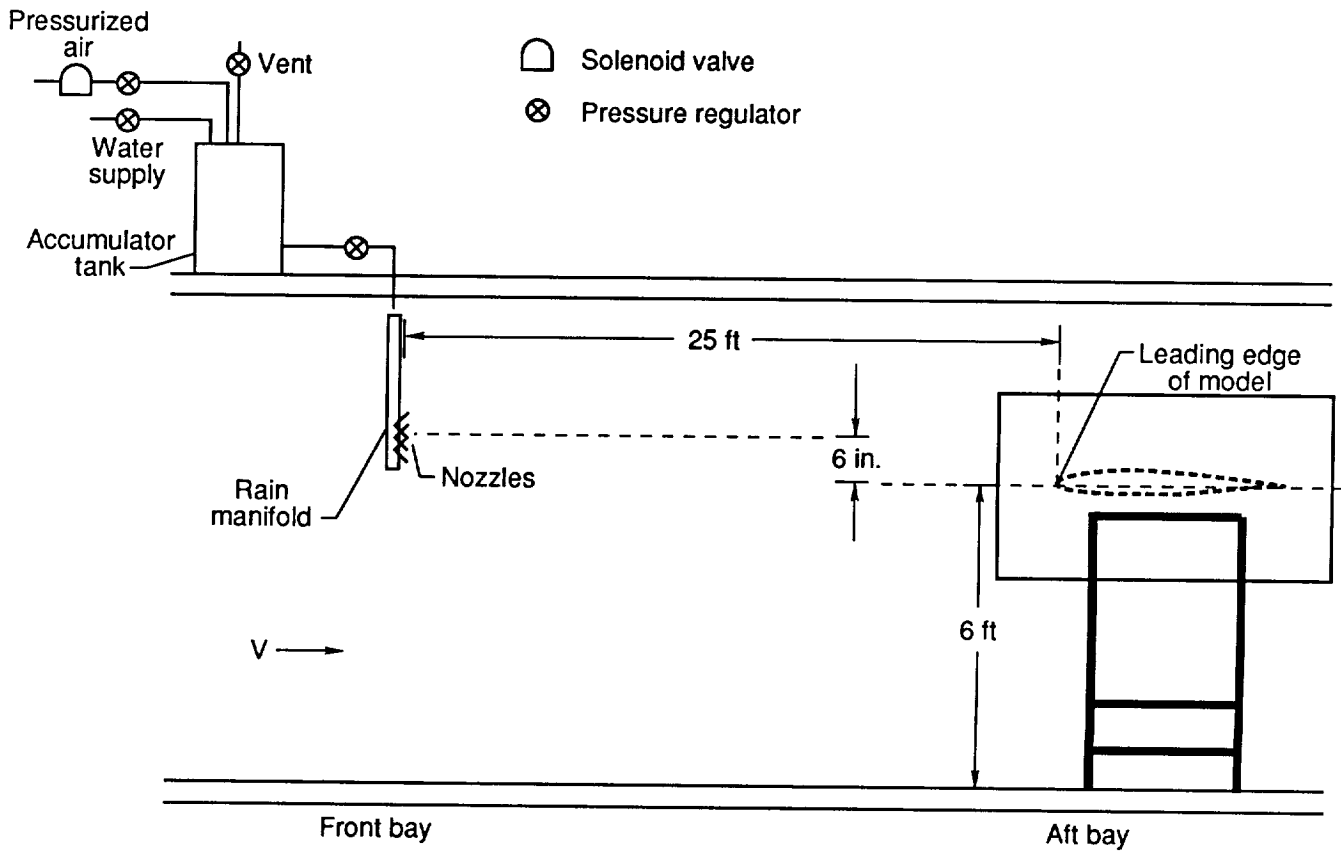
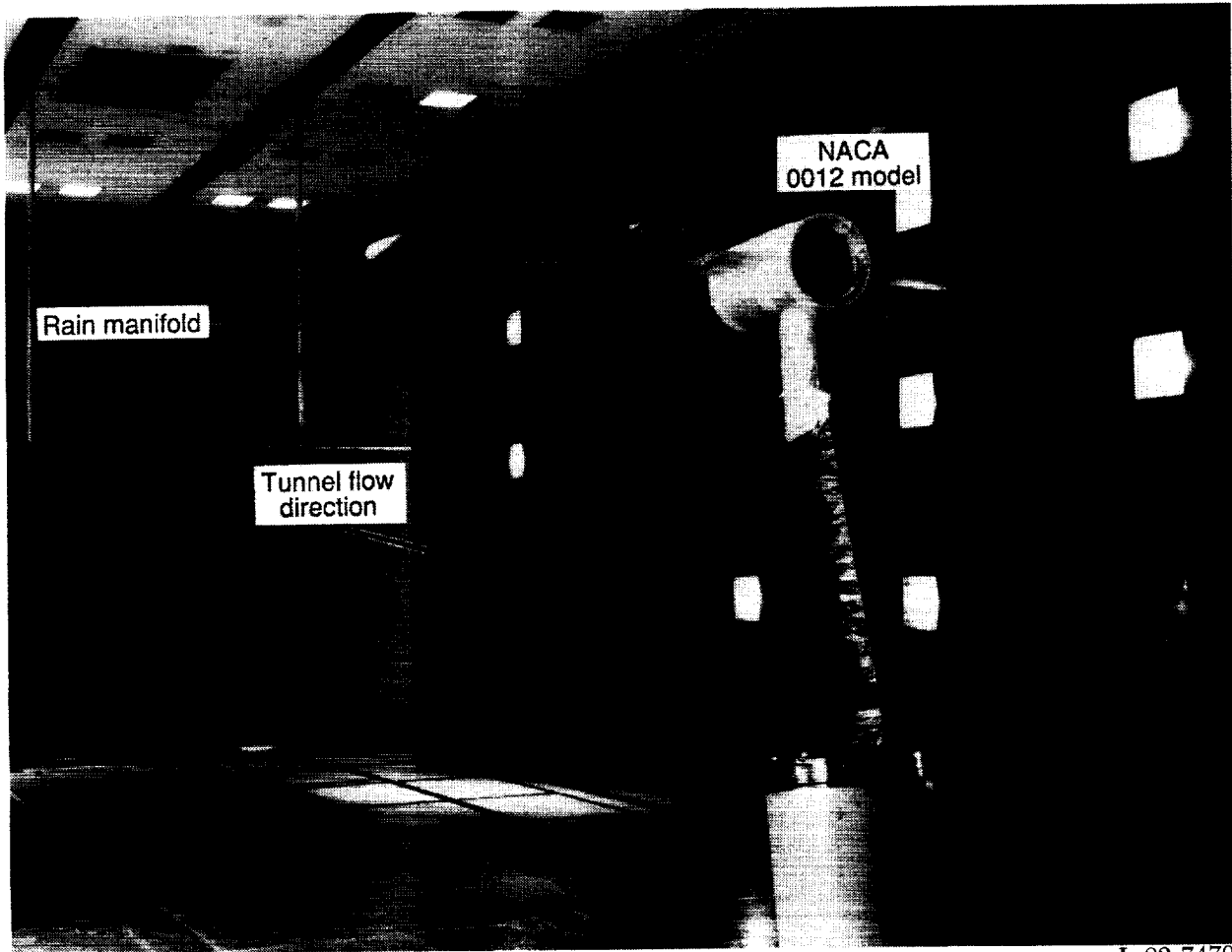


Figure 5. Schematic of test technique developed to produce rain in a wind tunnel facility.

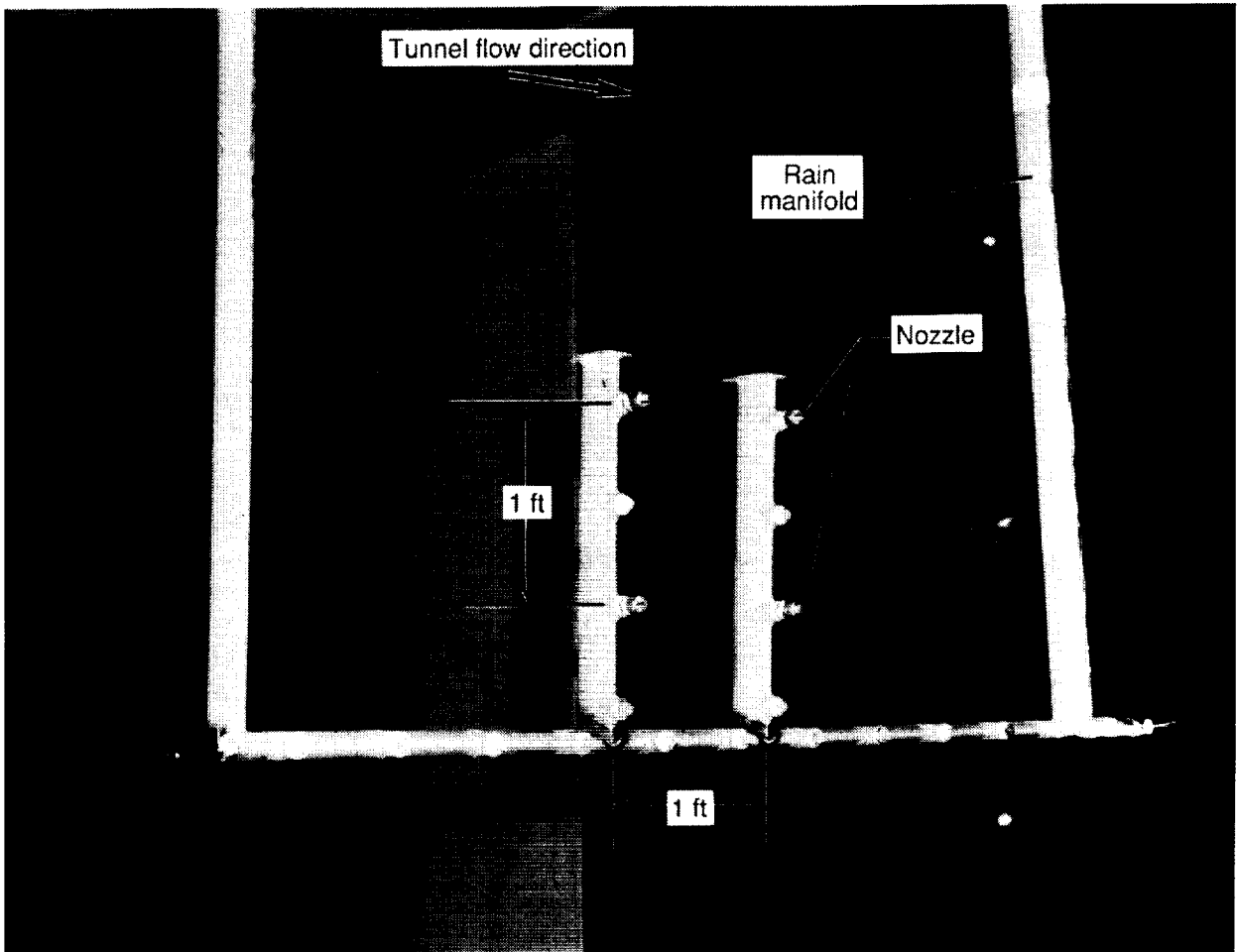
ORIGINAL PAGE
BLACK AND WHITE PHOTOGRAPH



L-82-7470

Figure 6. View of test setup looking upstream in Langley 14- by 22-Foot Subsonic Tunnel with NACA 0012 model installed.

ORIGINAL PAGE
BLACK AND WHITE PHOTOGRAPH



L-84-3926

Figure 7. Close-up view of rain manifold hardware modified for NACA 64-210 wind tunnel investigation.

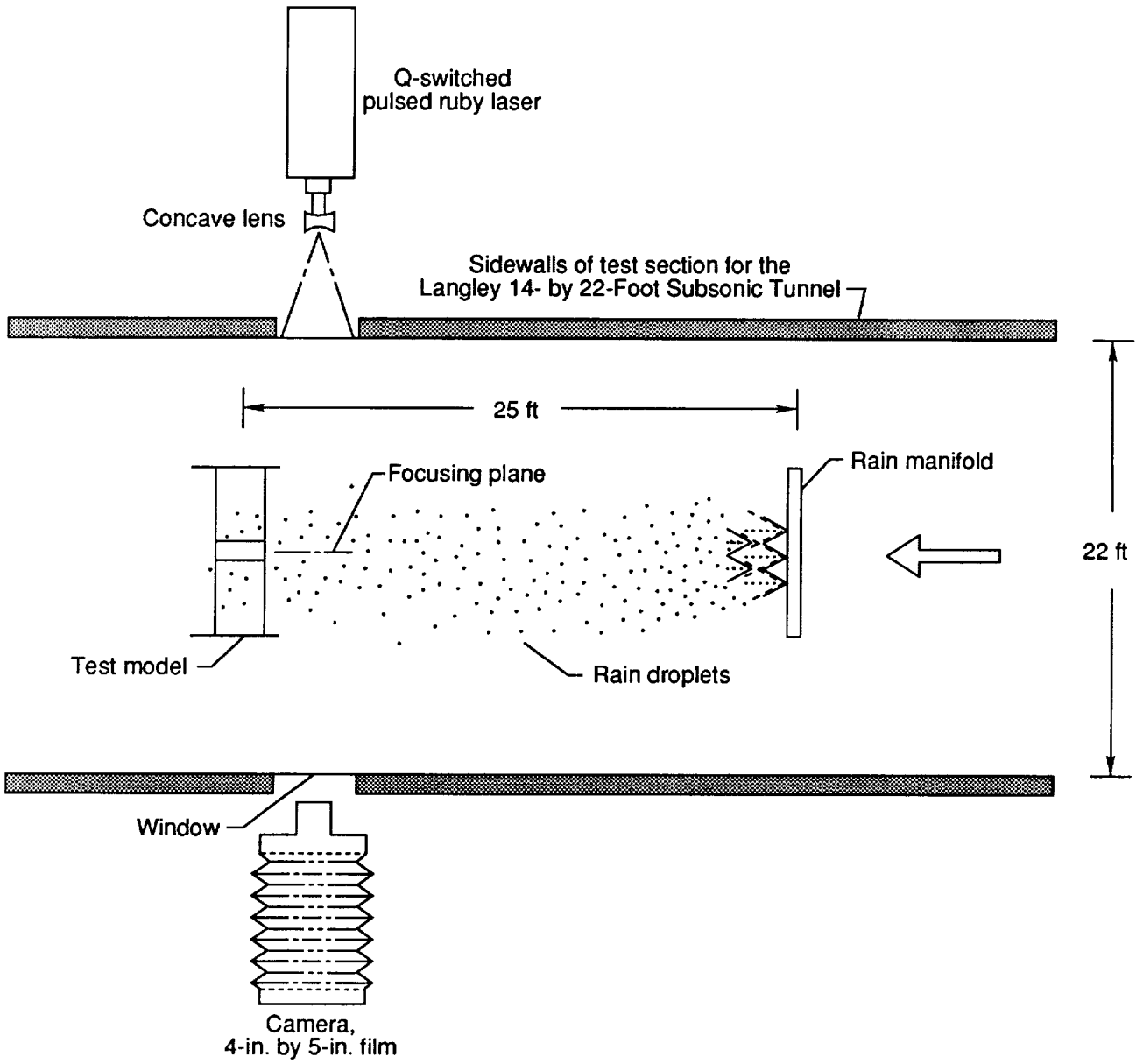


Figure 8. Sketch of laser system used to obtain drop size and drop distribution characteristics.

ORIGINAL PAGE
BLACK AND WHITE PHOTOGRAPH

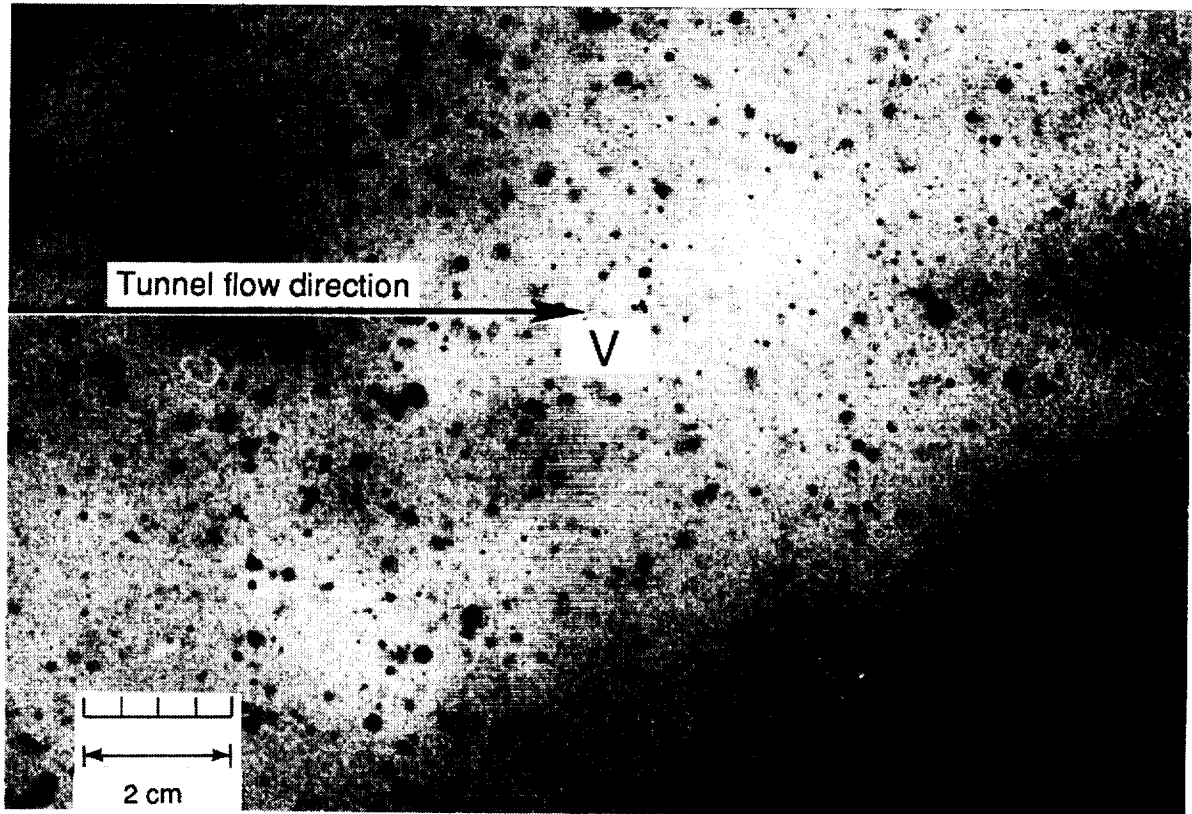
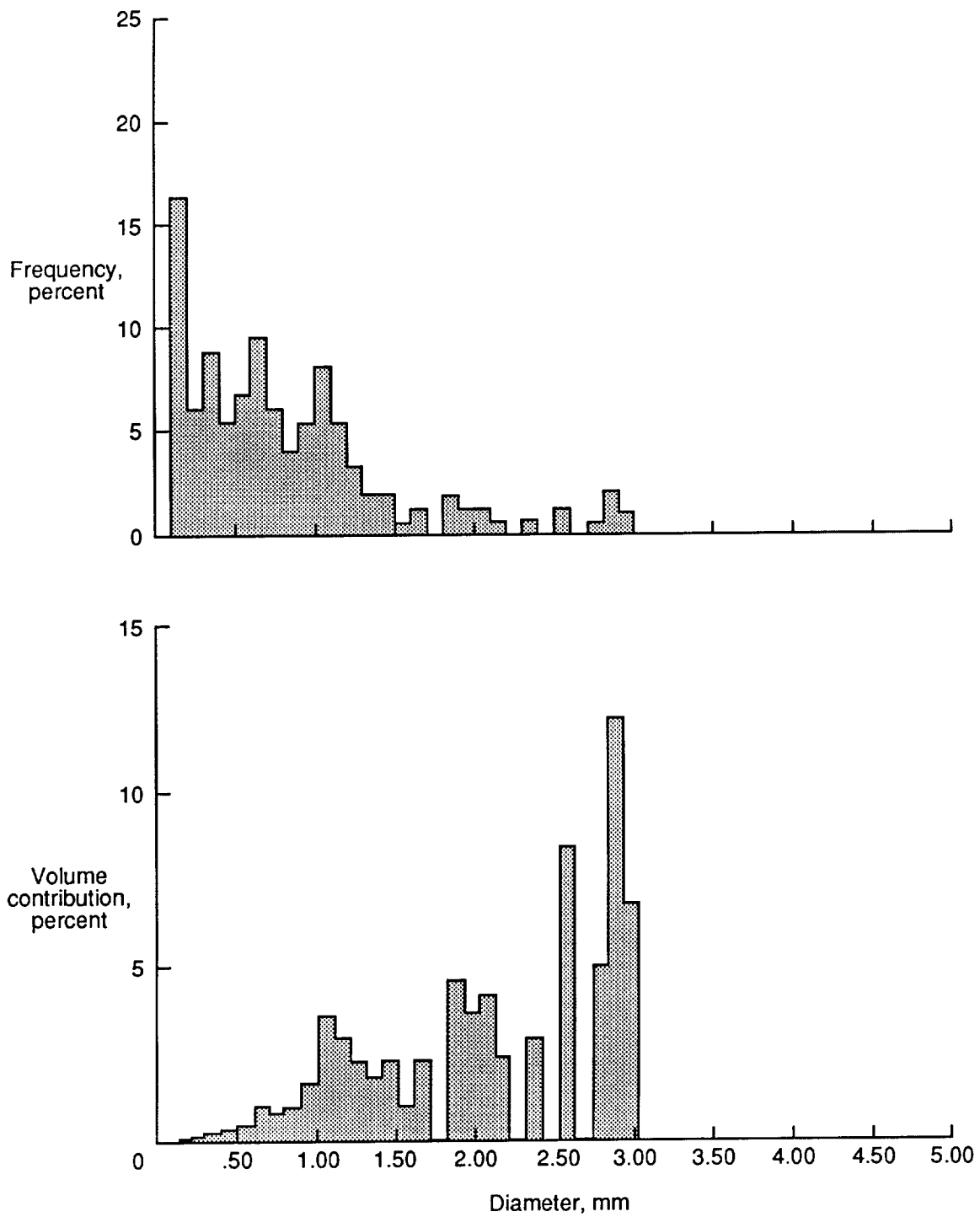
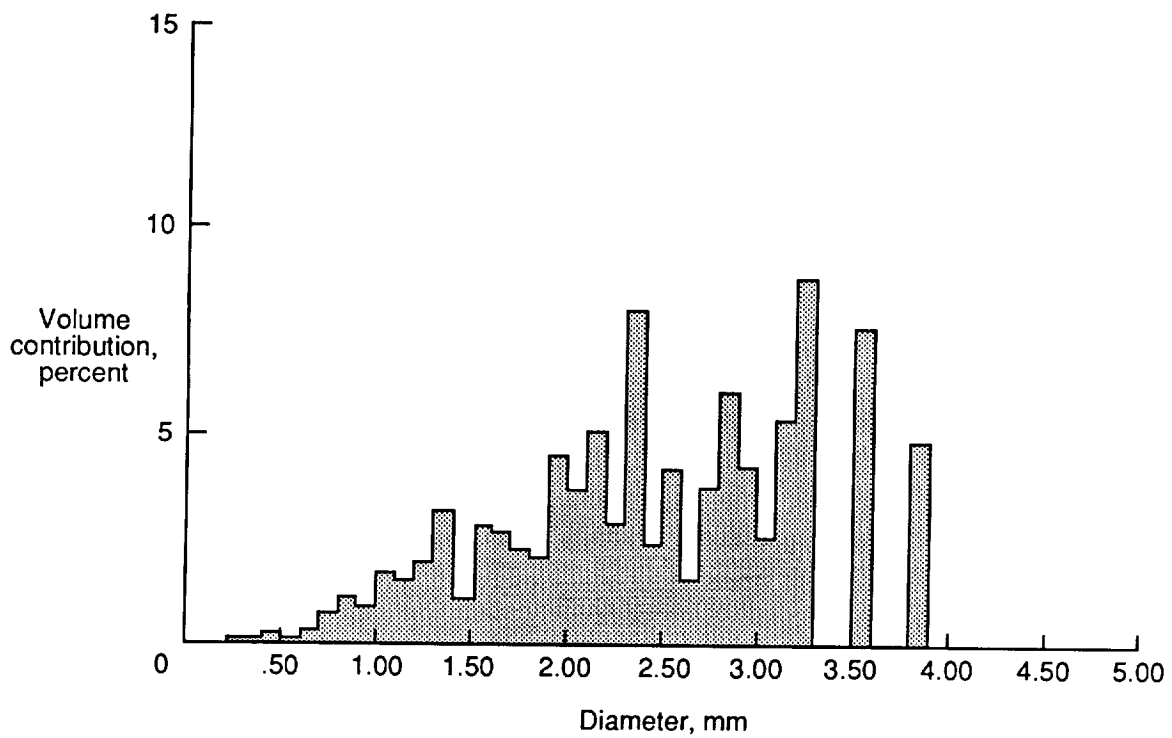
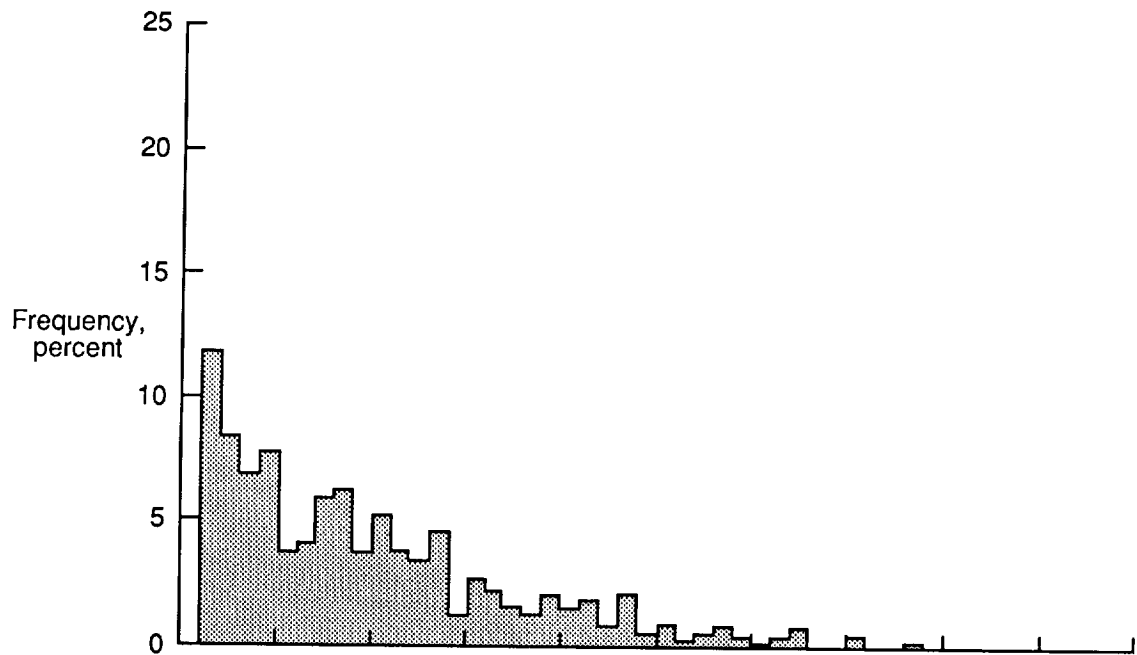


Figure 9. Sample of typical shadowgraph taken with laser system at tunnel dynamic pressure of 30 psf for 5-tube nozzle configuration.



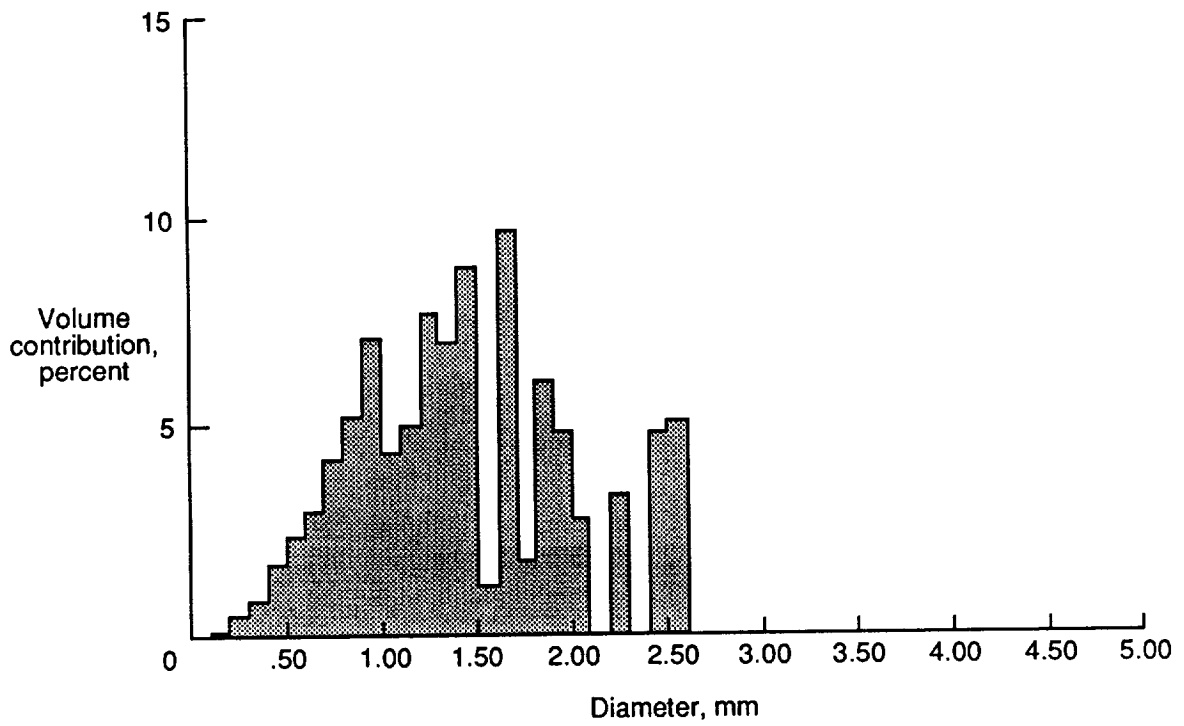
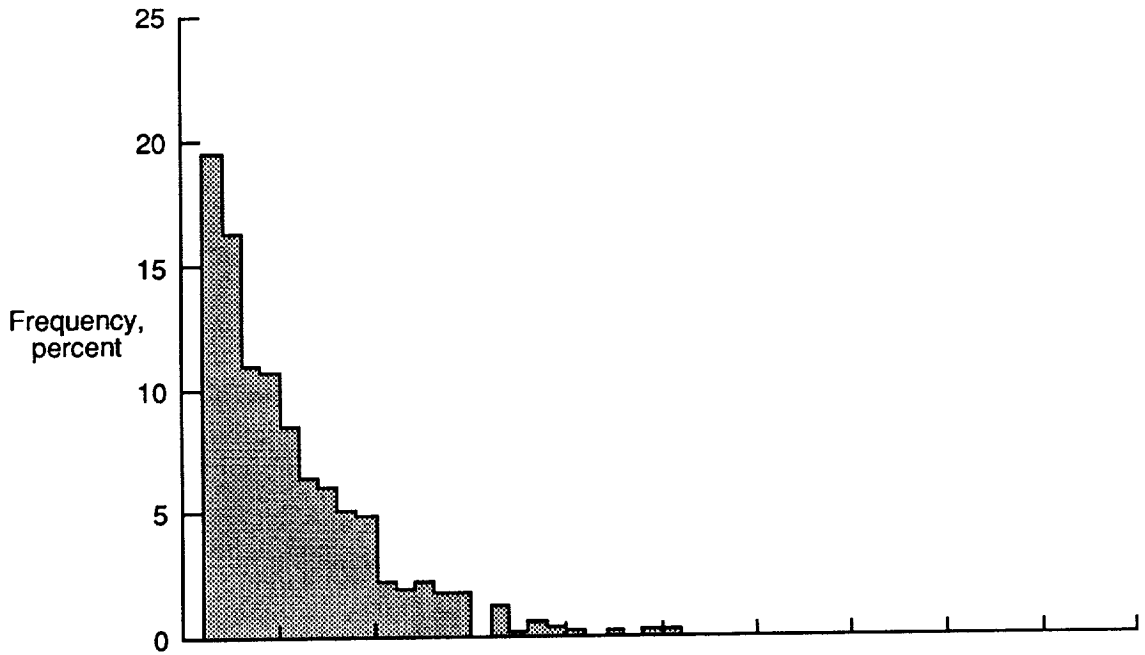
(a) Drop size spectrum at 80 psi and 112 ft/sec ($q = 15$ psf).

Figure 10. Drop size characteristics of JPL hypodermic nozzle (B1N5).



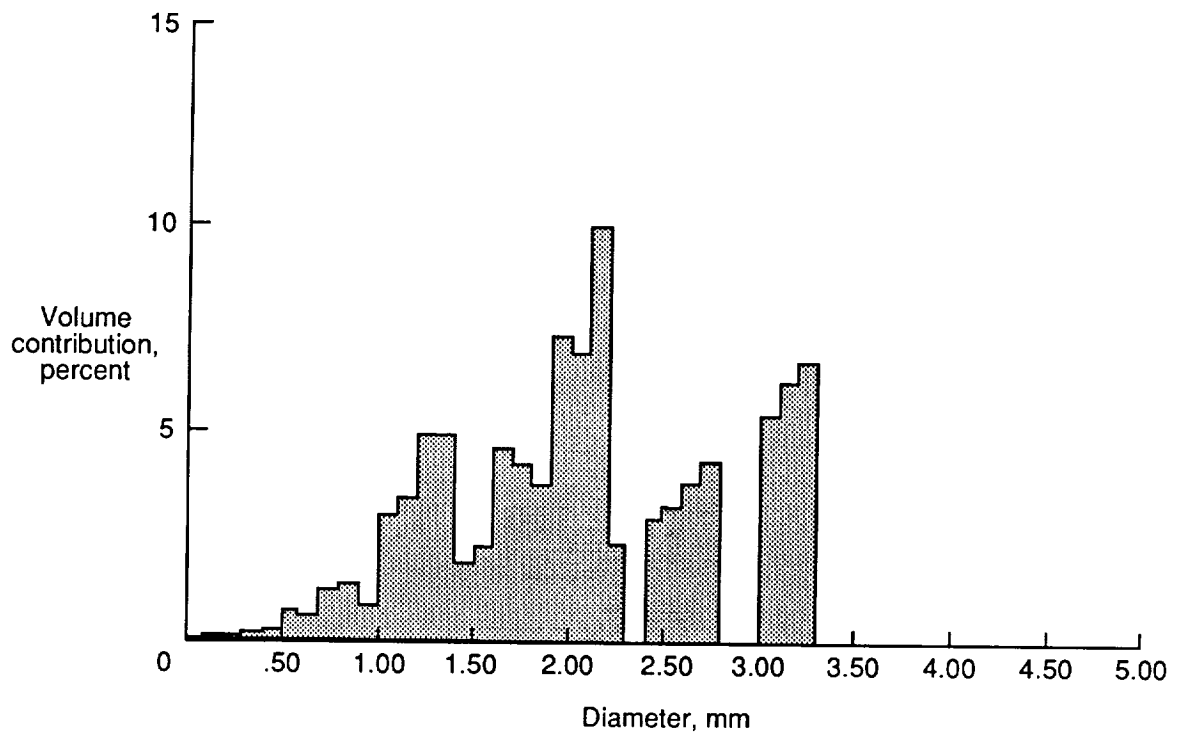
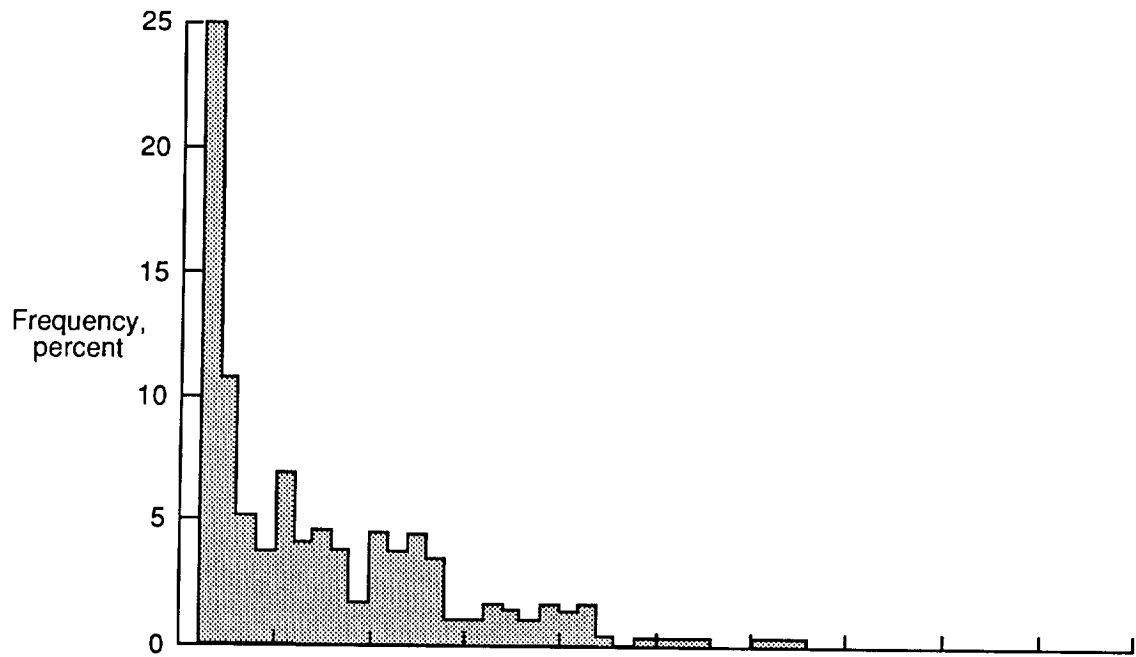
(b) Drop size spectrum at 80 psi and 159 ft/sec ($q = 30$ psf).

Figure 10. Continued.



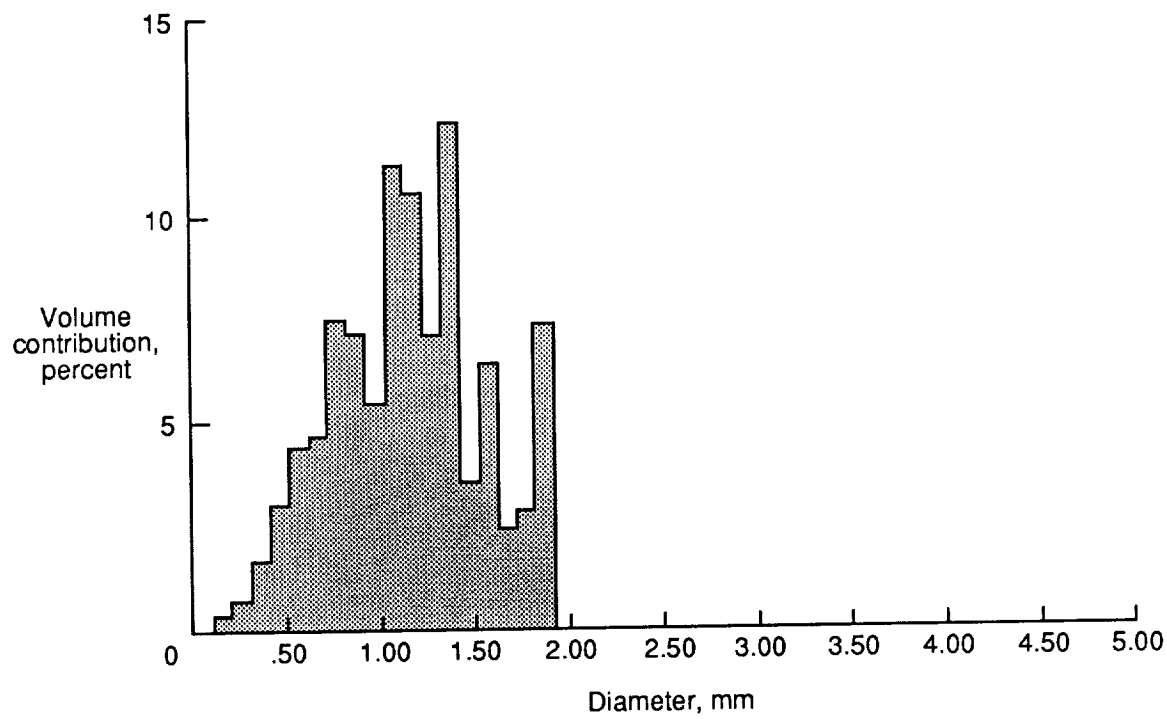
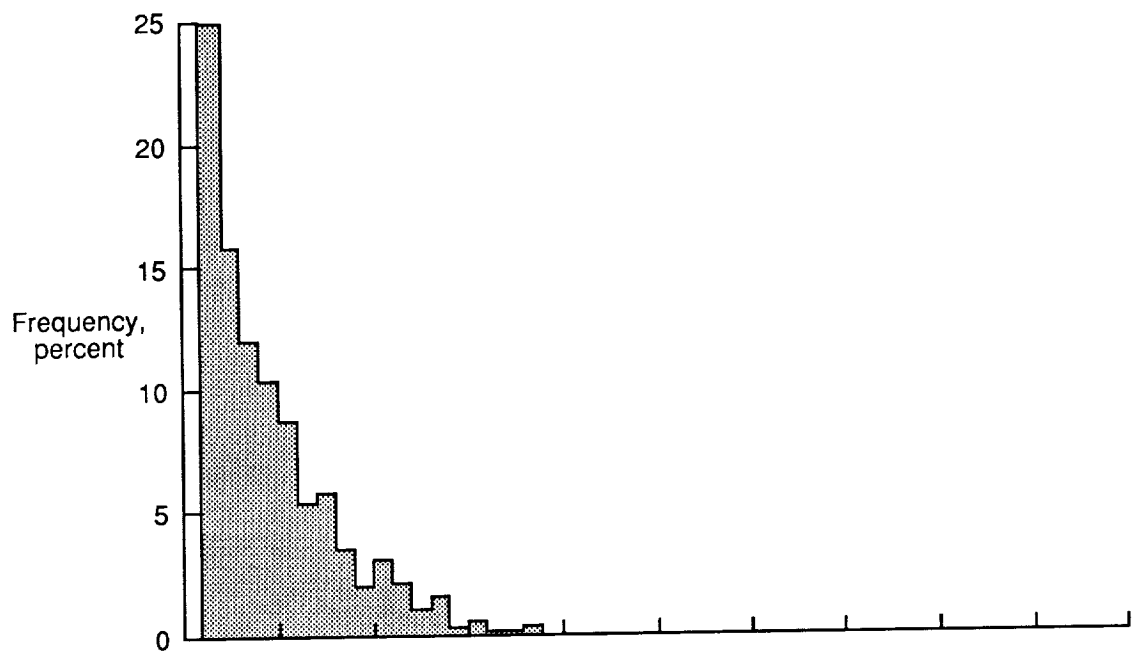
(c) Drop size spectrum at 80 psi and 207 ft/sec ($q = 50$ psf).

Figure 10. Concluded.



(a) Drop size spectrum at 50 psi and 159 ft/sec ($q = 30$ psf).

Figure 11. Drop size characteristics of fan jet nozzle (1570).



(b) Drop size spectrum at 70 psi and 246 ft/sec ($q = 70$ psf).

Figure 11. Concluded.

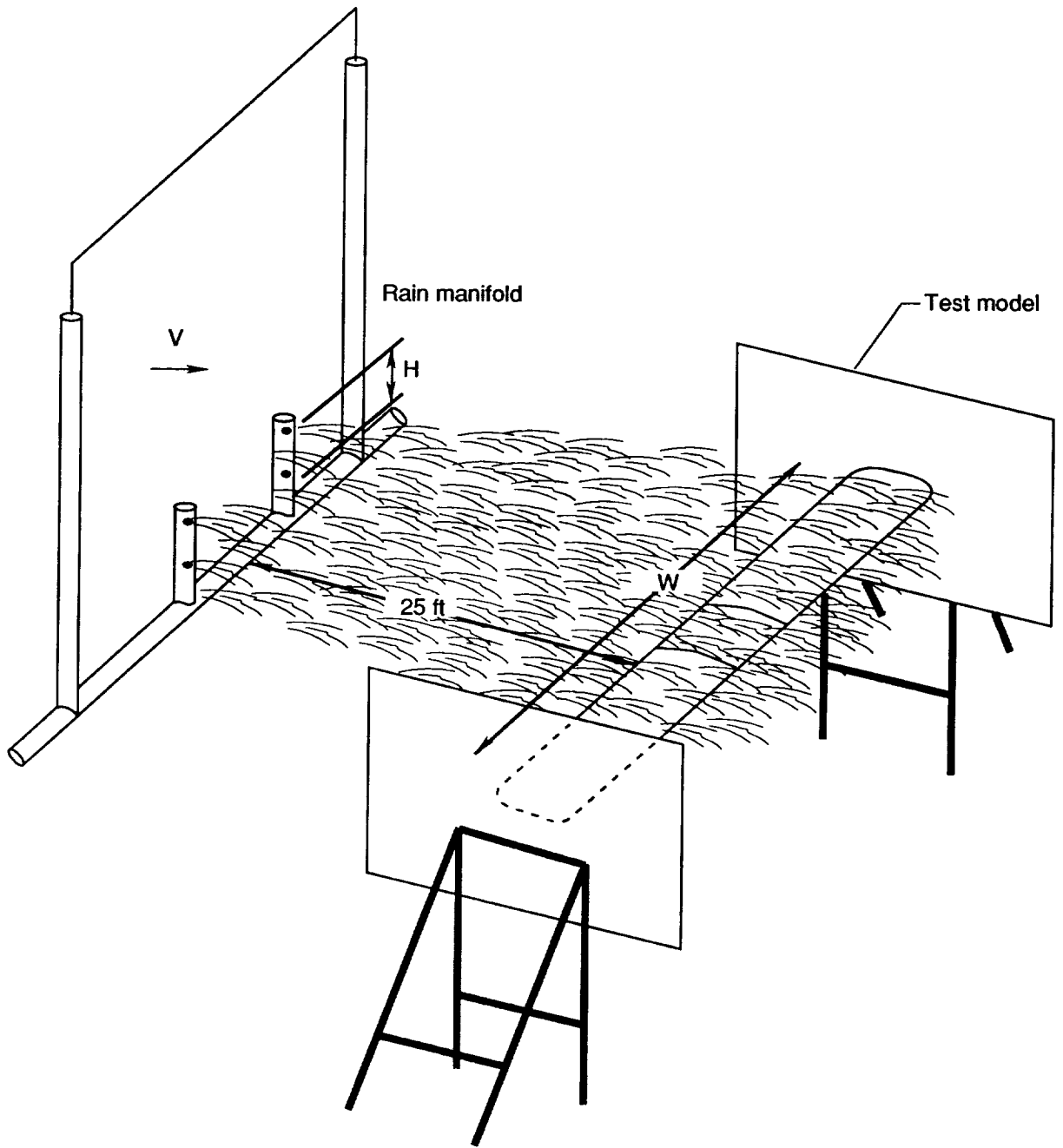
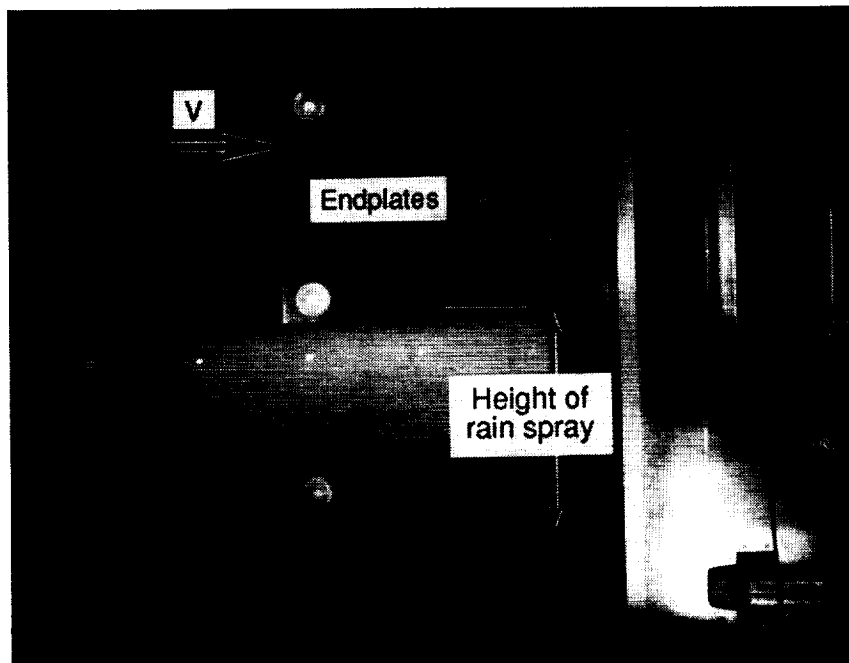
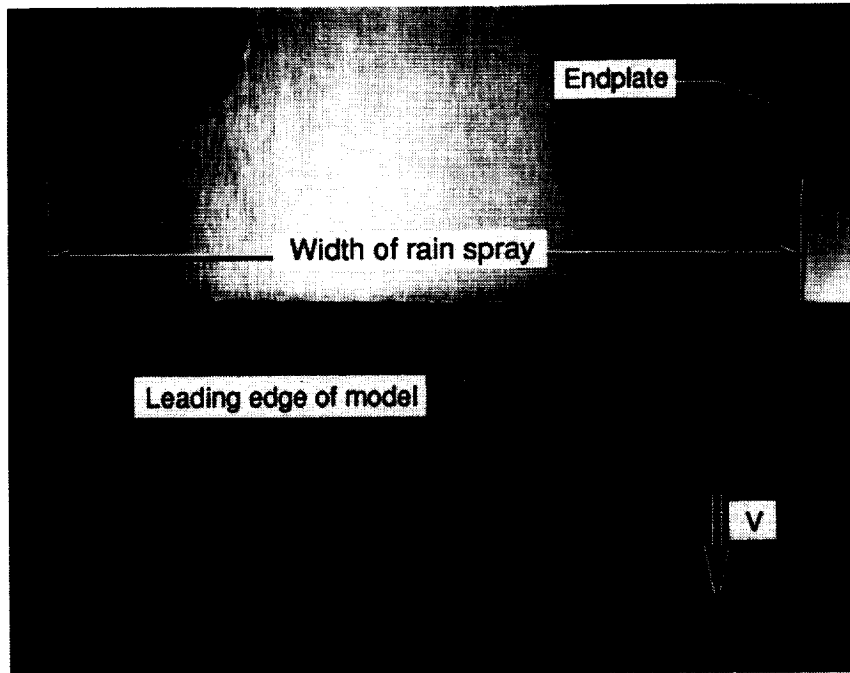


Figure 12. Relationship used for determining liquid water content in wind tunnel facility. $IWC = KQ/VWH$;
 $K = 2225.8086$.



L-92-29

Figure 13. Sample of typical rain spray area coverage photograph taken at model location.

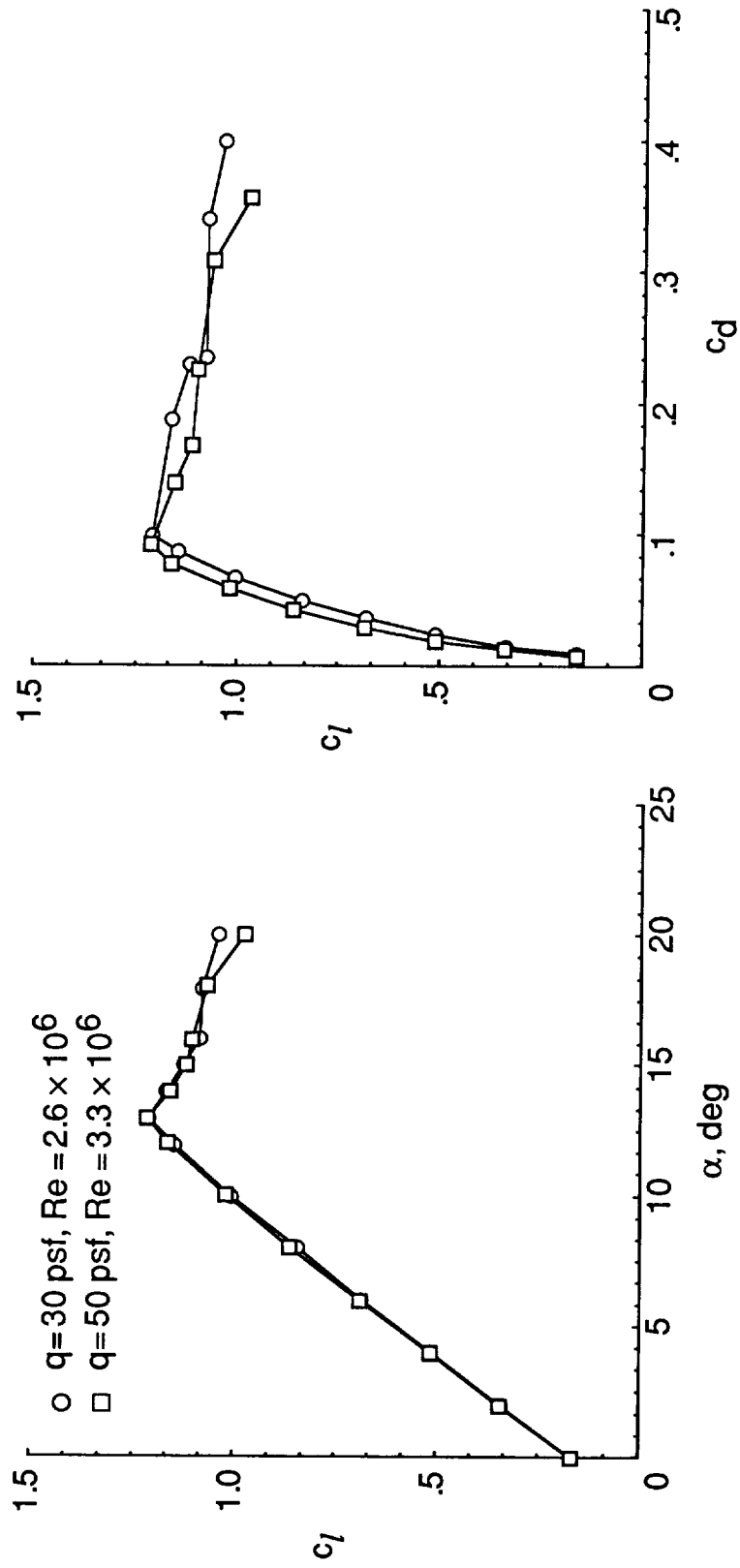


Figure 14. Effect of Reynolds number for cruise configuration.

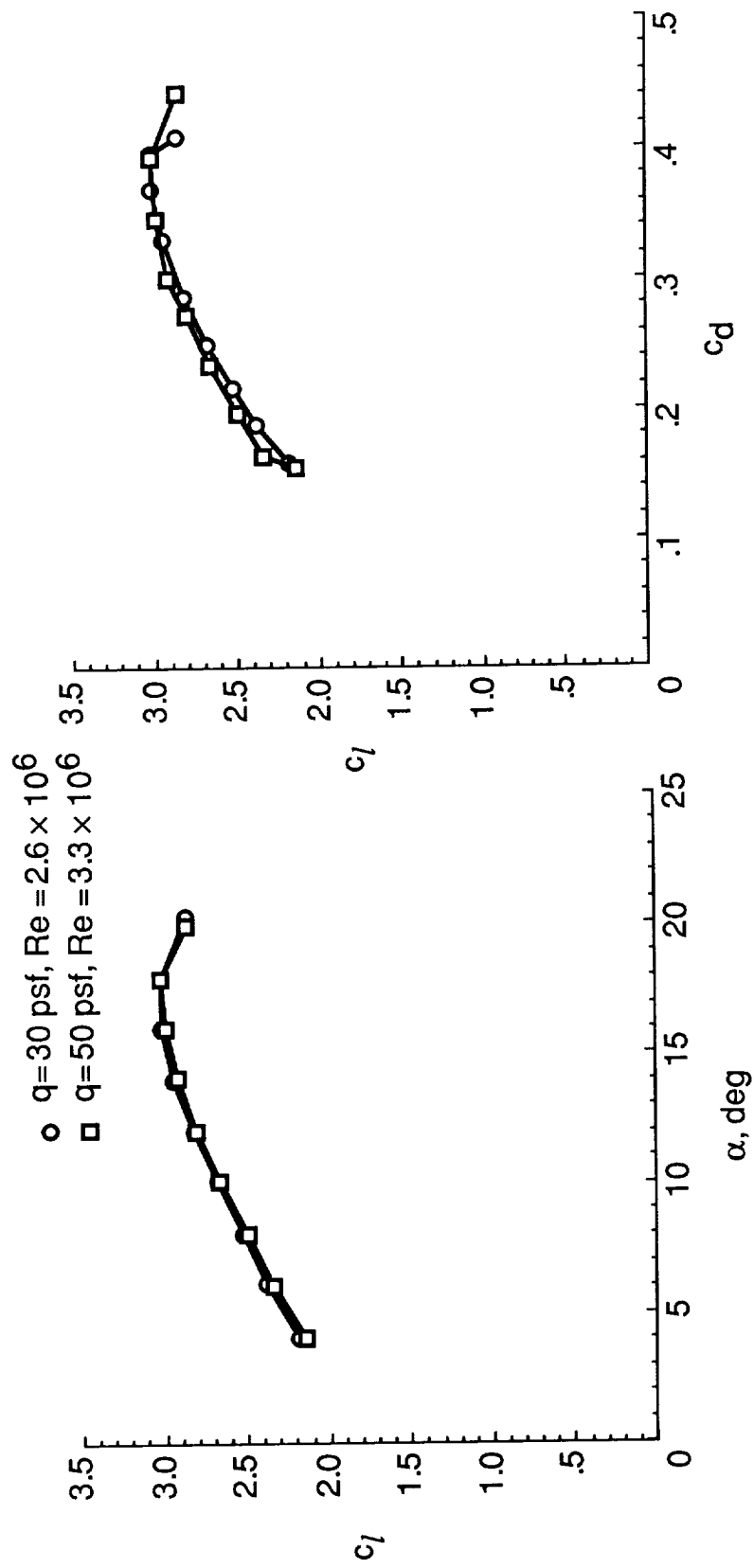


Figure 15. Effect of Reynolds number for landing configuration.

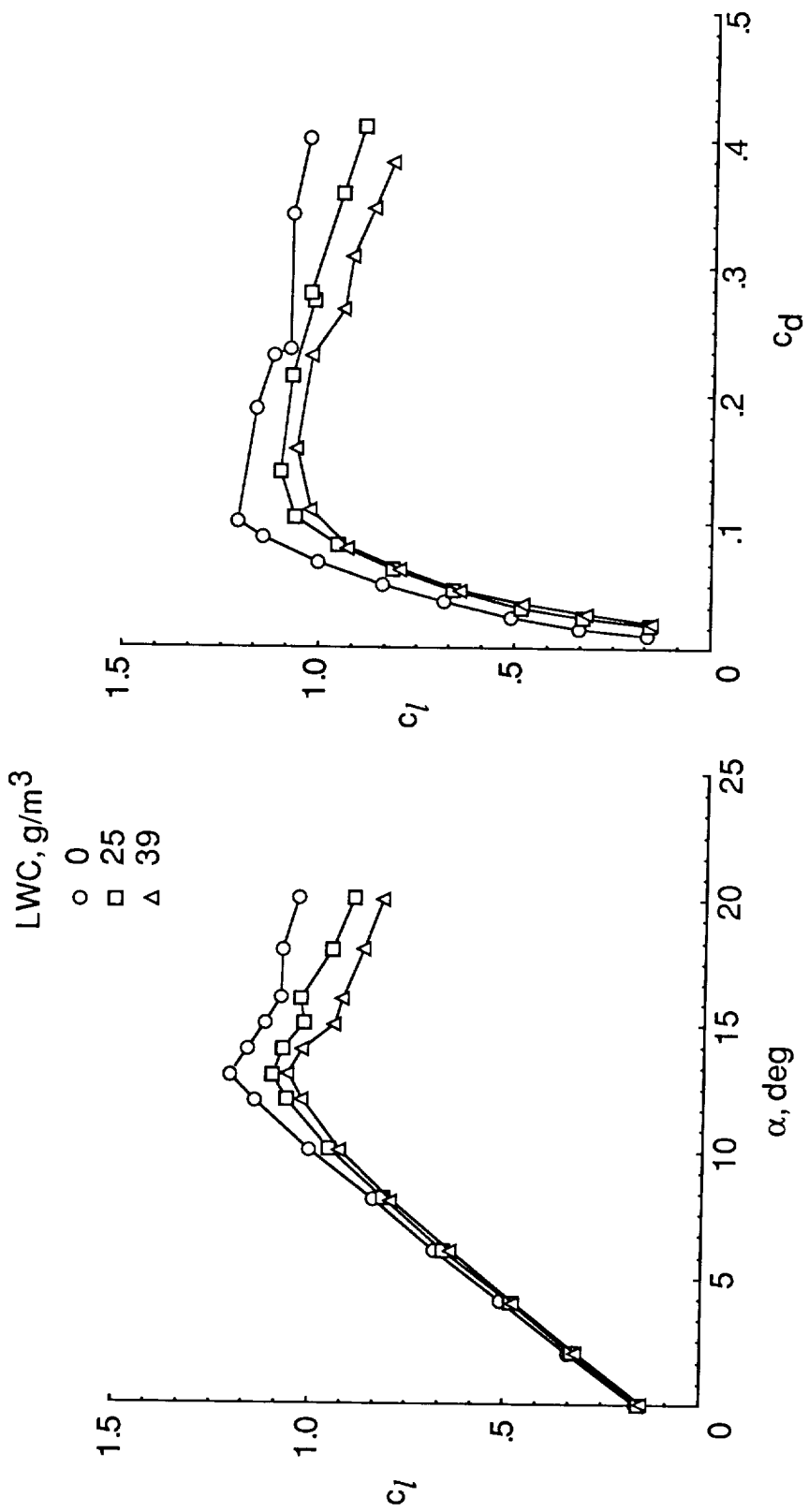


Figure 16. Cruise configuration lift curve and drag polar at dynamic pressure of 30 psf.

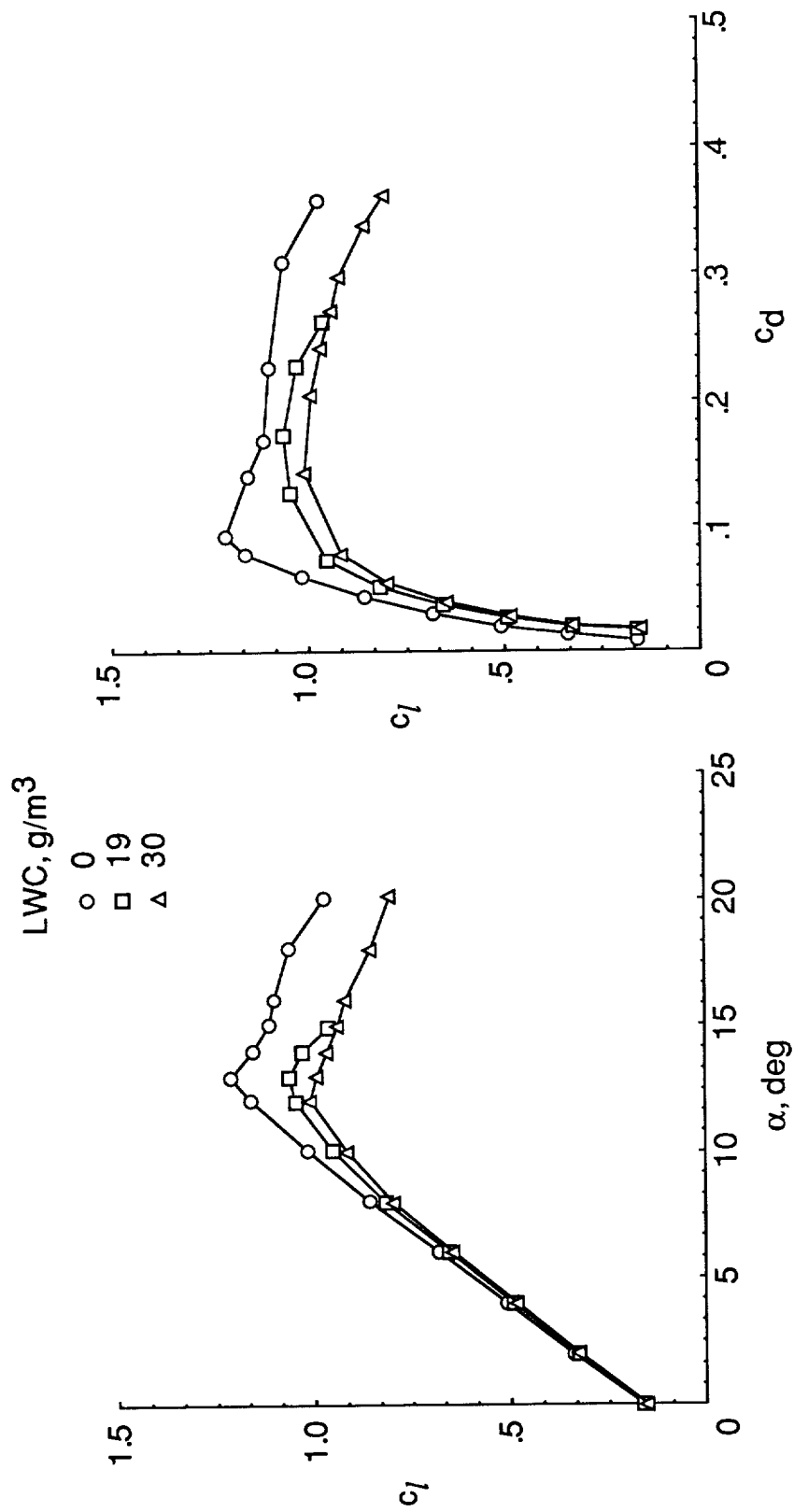


Figure 17. Cruise configuration lift curve and drag polar at dynamic pressure of 50 psf.

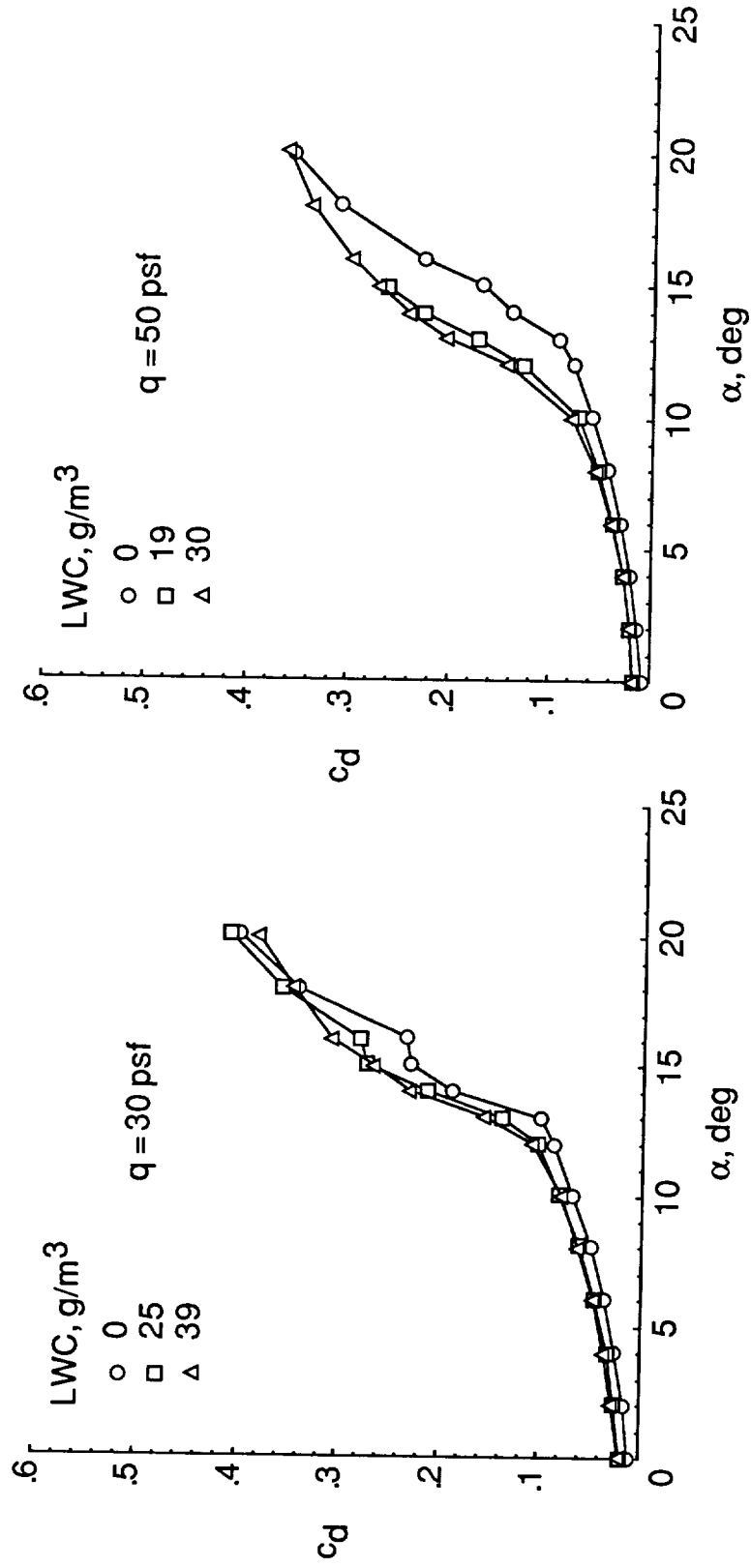
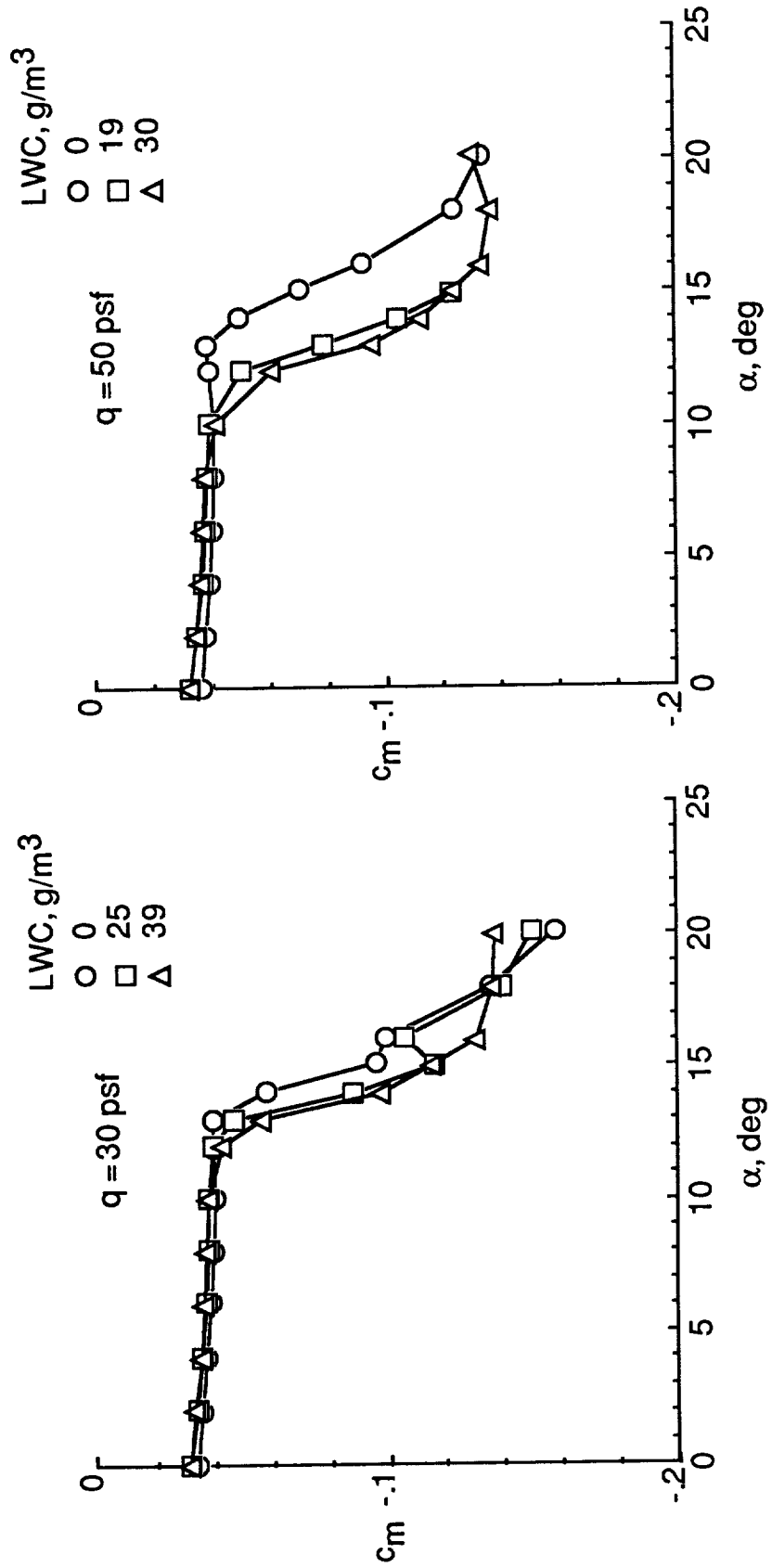
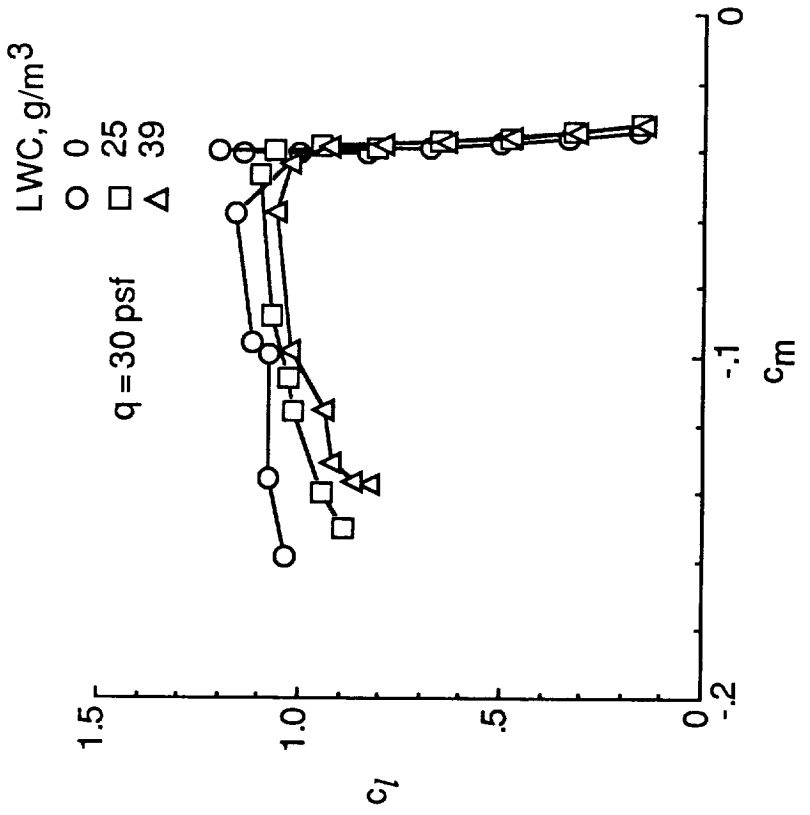
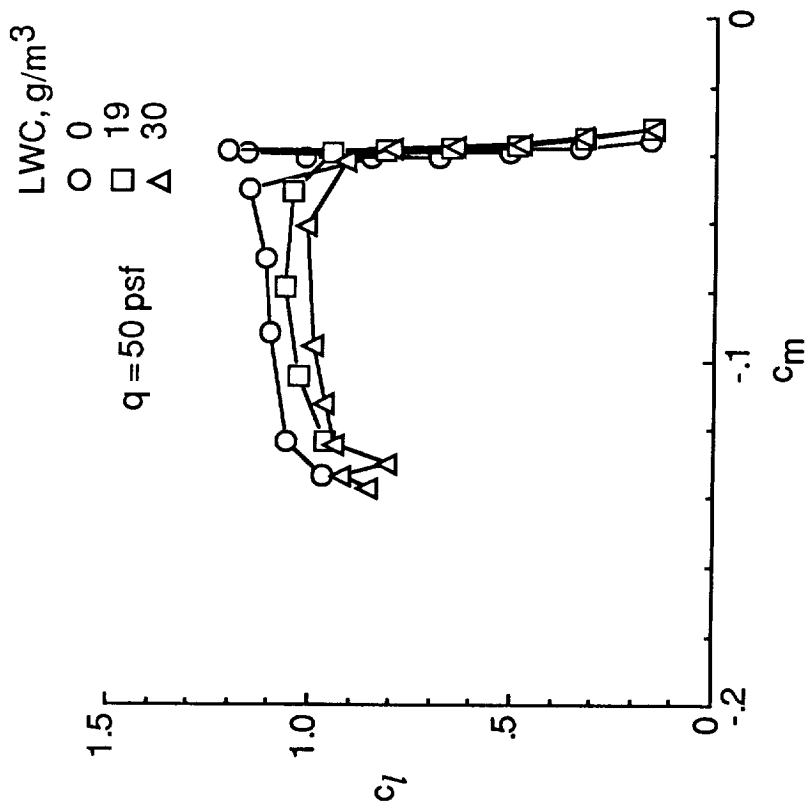


Figure 18. Cruise configuration drag as function of angle of attack.



(a) Pitching moment as a function of angle of attack.

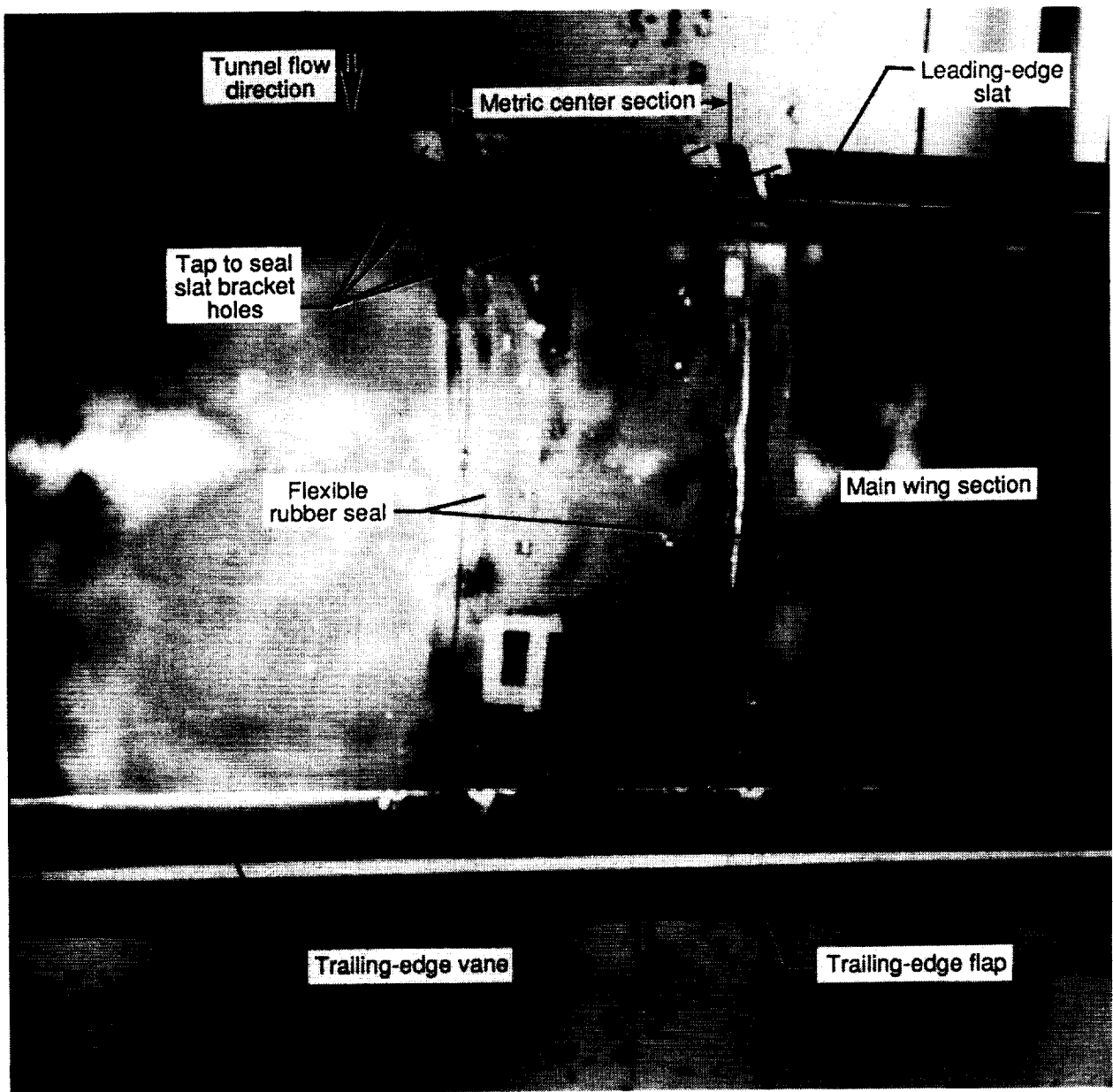
Figure 19. Effect of rain on cruise configuration pitching moment.



(b) Lift as a function of pitching moment.

Figure 19. Concluded.

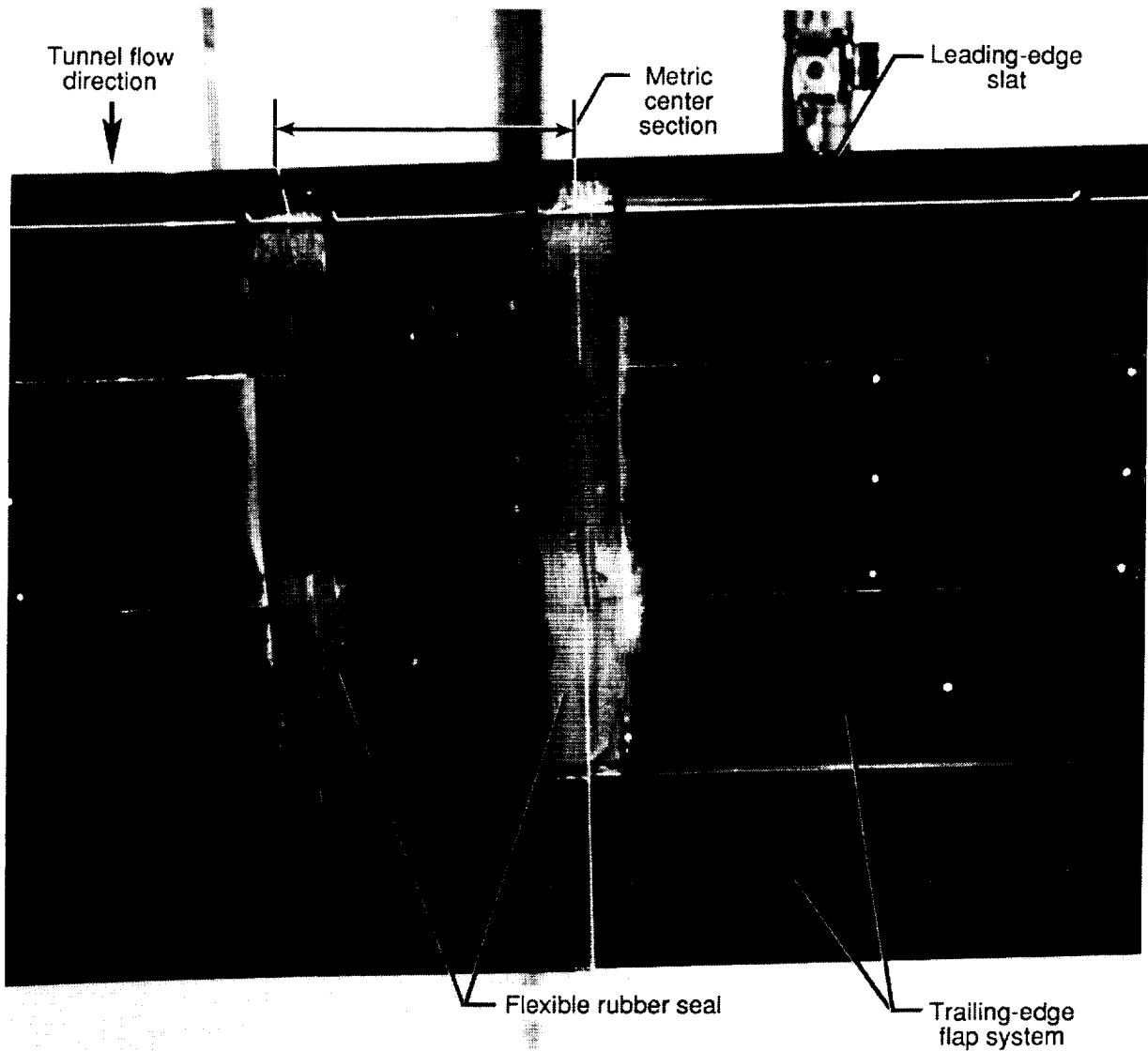
ORIGINAL PAGE
BLACK AND WHITE PHOTOGRAPH



L-92-30

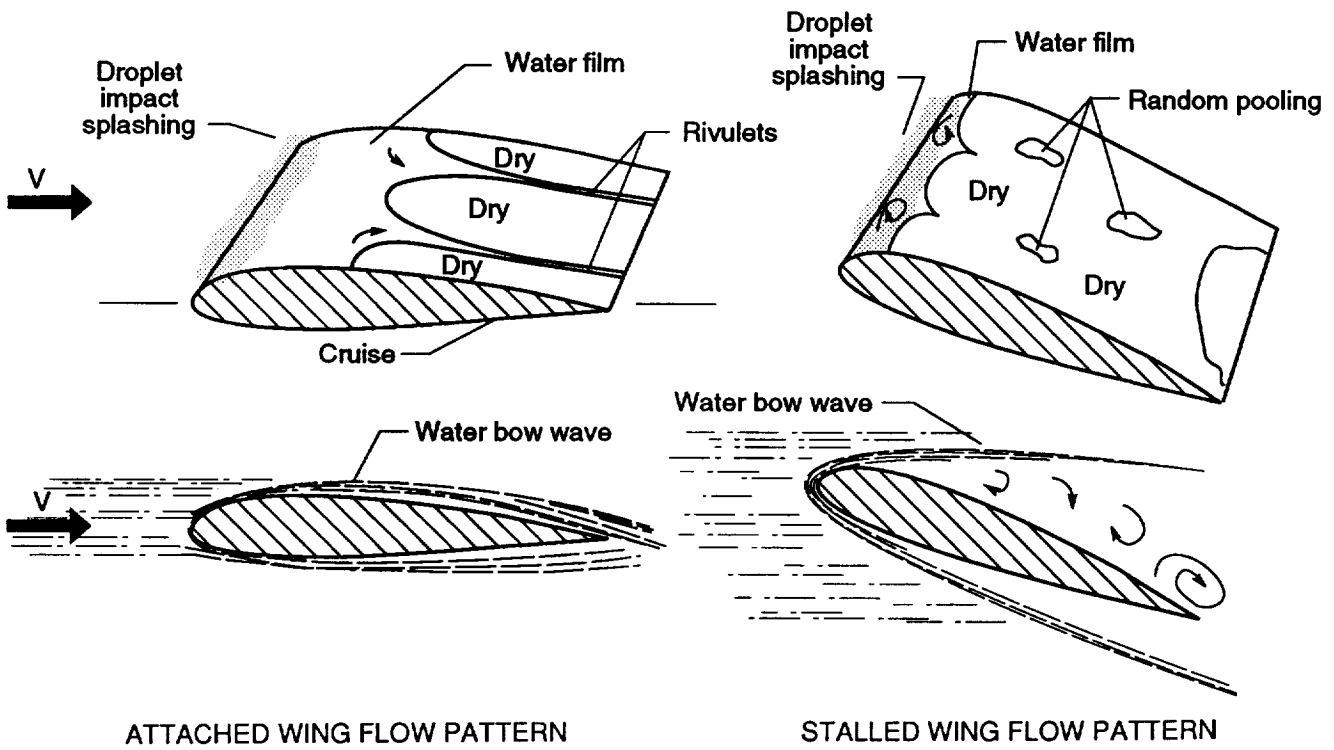
Figure 20. View of upper surface blemishes on airfoil model prior to water flow visualization process.

ORIGINAL DATA
BLACK AND WHITE PHOTOGRAPH



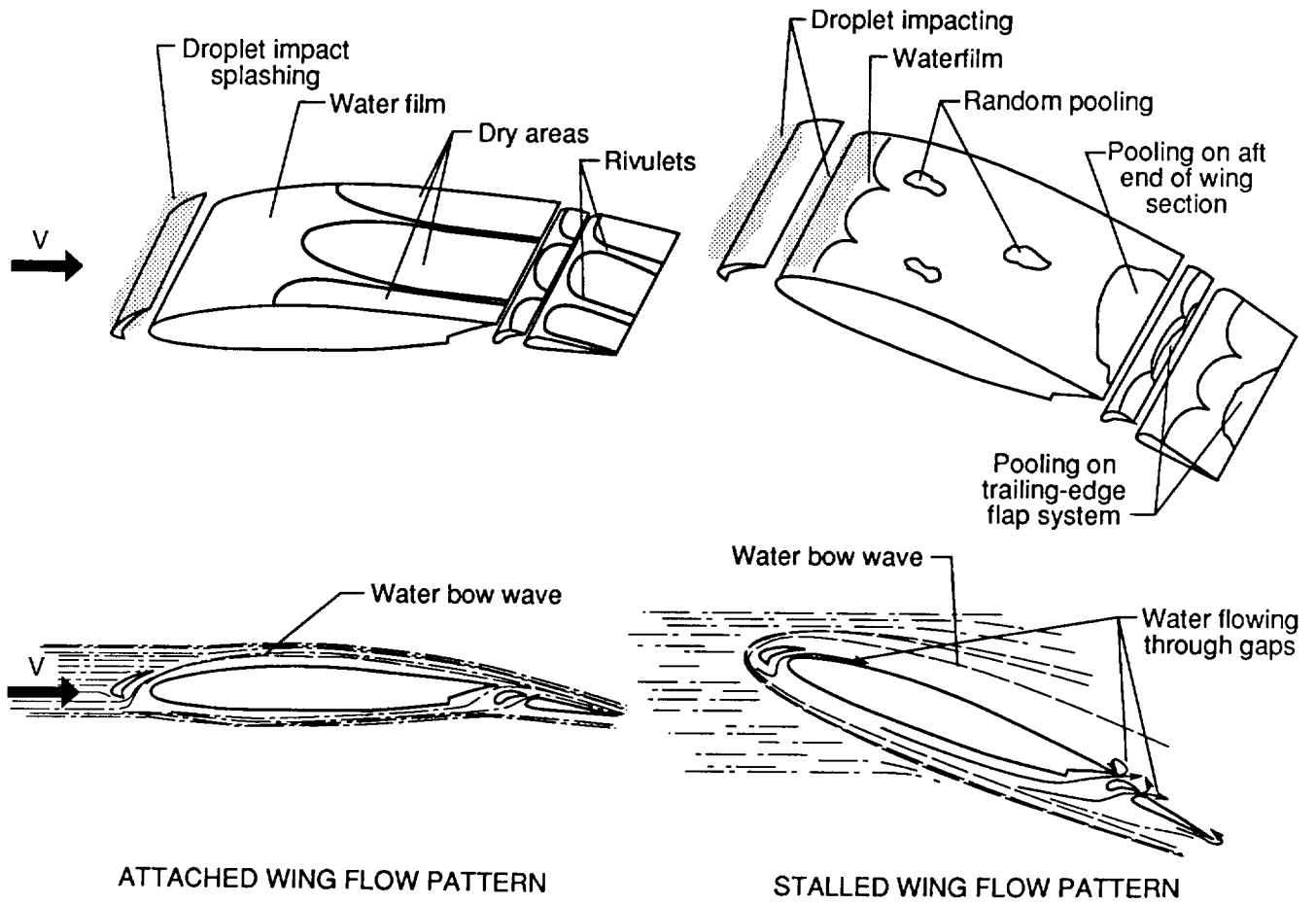
L-92-31

Figure 21. View of lower surface blemishes on airfoil model prior to water flow visualization process.



(a) Cruise configuration.

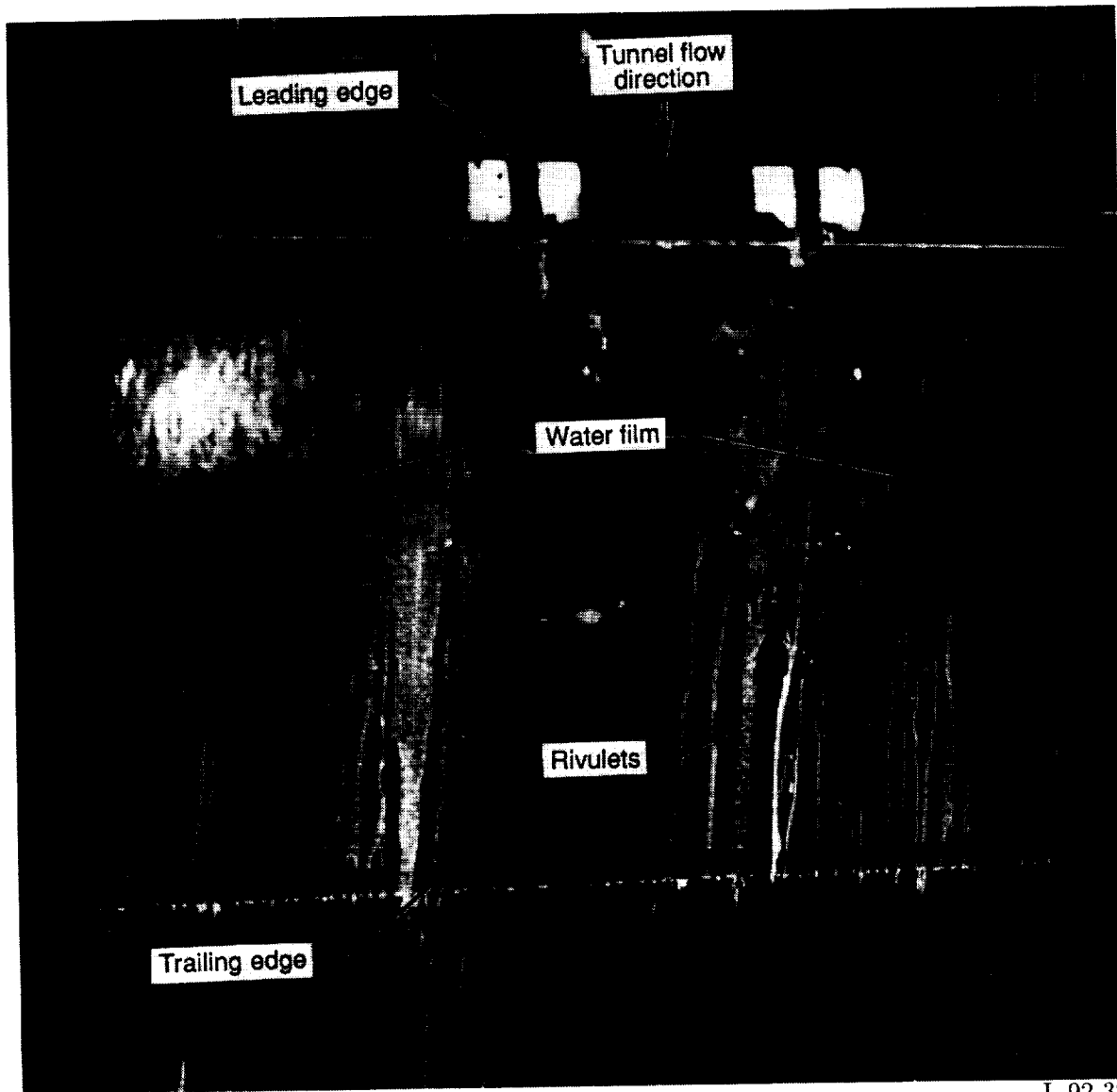
Figure 22. Water flow characteristics about 64-210 airfoil model.



(b) Landing configuration.

Figure 22. Concluded.

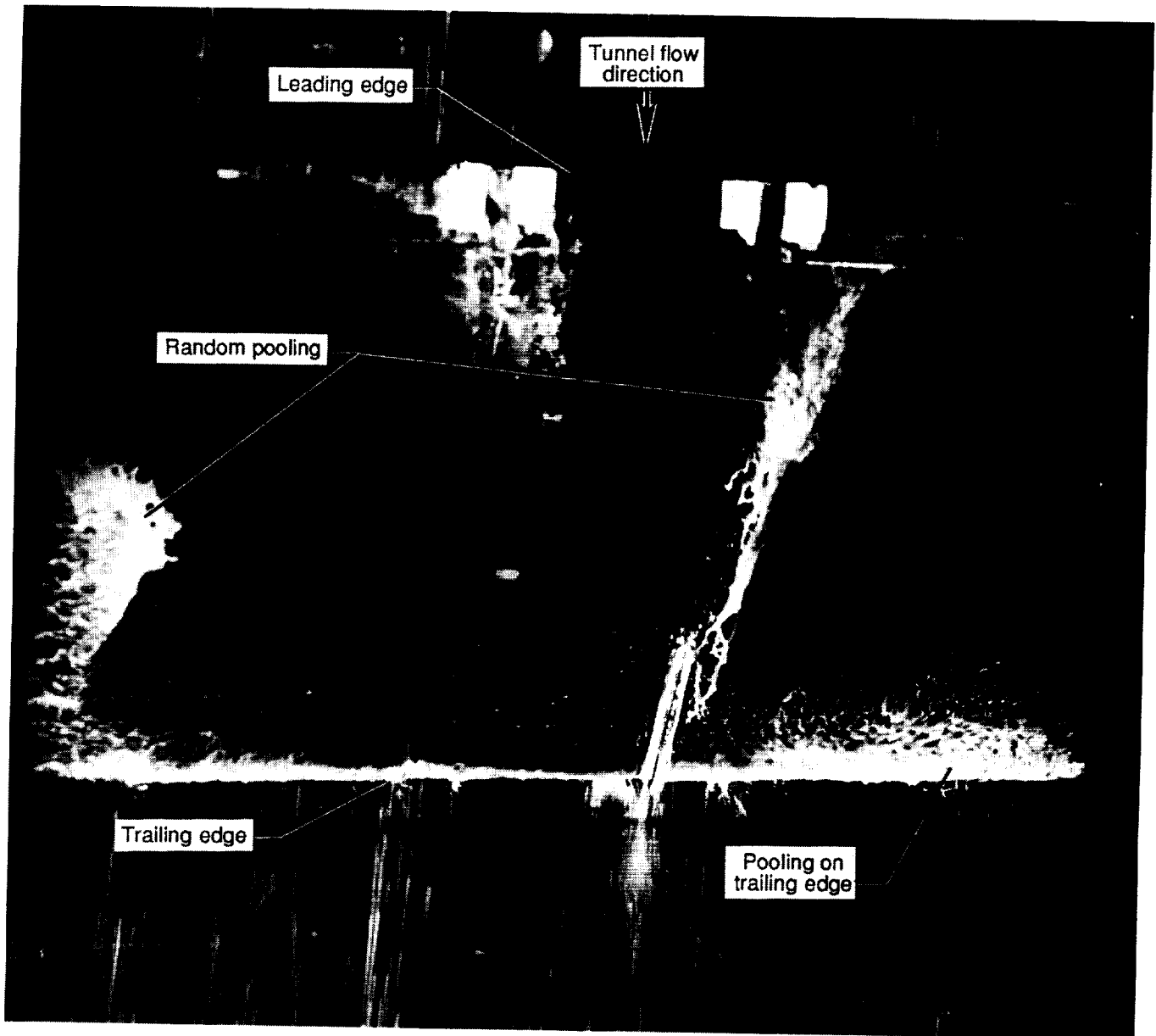
ORIGINAL PAGE
BLACK AND WHITE PHOTOGRAPH



L-92-32

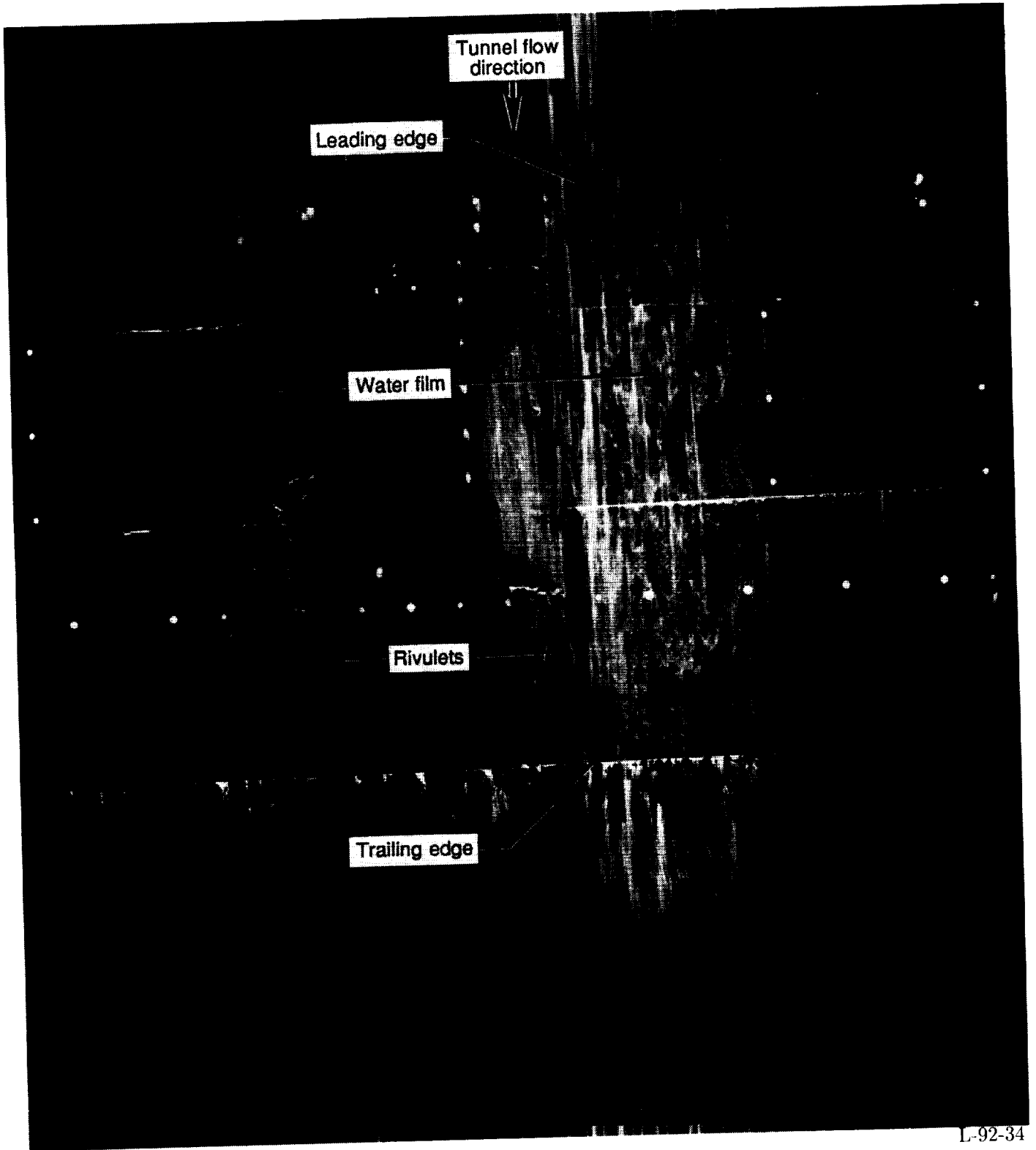
Figure 23. Sample of typical water film pattern on upper surface of model for cruise configuration at angle of attack of 0° , dynamic pressure of 15 psf, and $LWC = 17 \text{ g/m}^3$.

ORIGINAL PAGE
GRAY AND WHITE PHOTOGRAPH



L-92-33

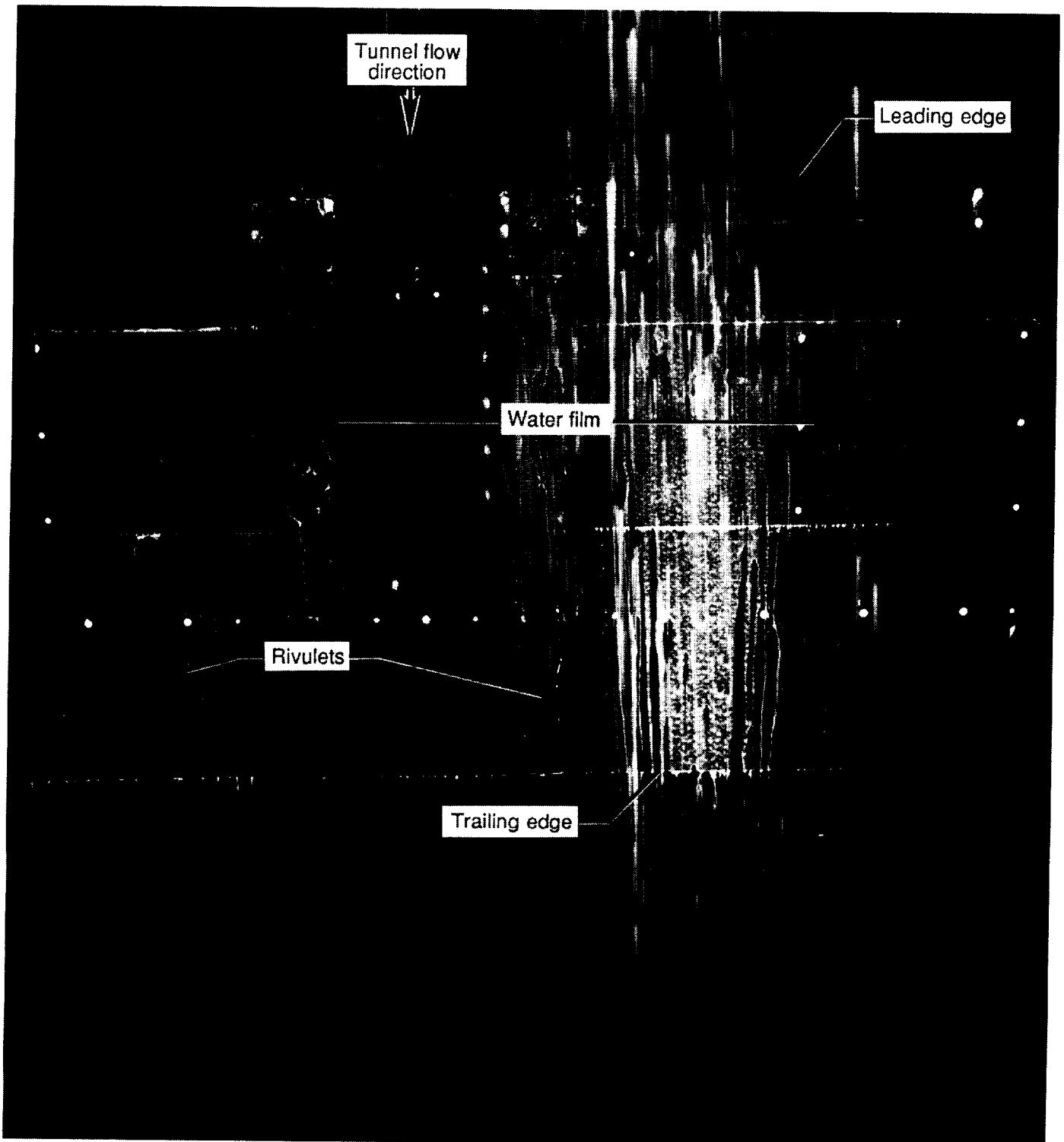
Figure 24. Sample of typical water film pattern on upper surface of model for cruise configuration at angle of attack of 20° , dynamic pressure of 15 psf, and $LWC = 17 \text{ g/m}^3$.



L-92-34

Figure 25. Sample of typical water film pattern on lower surface of model for cruise configuration at angle of attack of 4° , dynamic pressure of 15 psf, and $LWC = 14 \text{ g/m}^3$.

BLACK AND WHITE PHOTOGRAPH



L-92-35

Figure 26. Sample of typical water film pattern on lower surface of model for cruise configuration at angle of attack of 16° , dynamic pressure of 15 psf, and $LWC = 14 \text{ g/m}^3$.

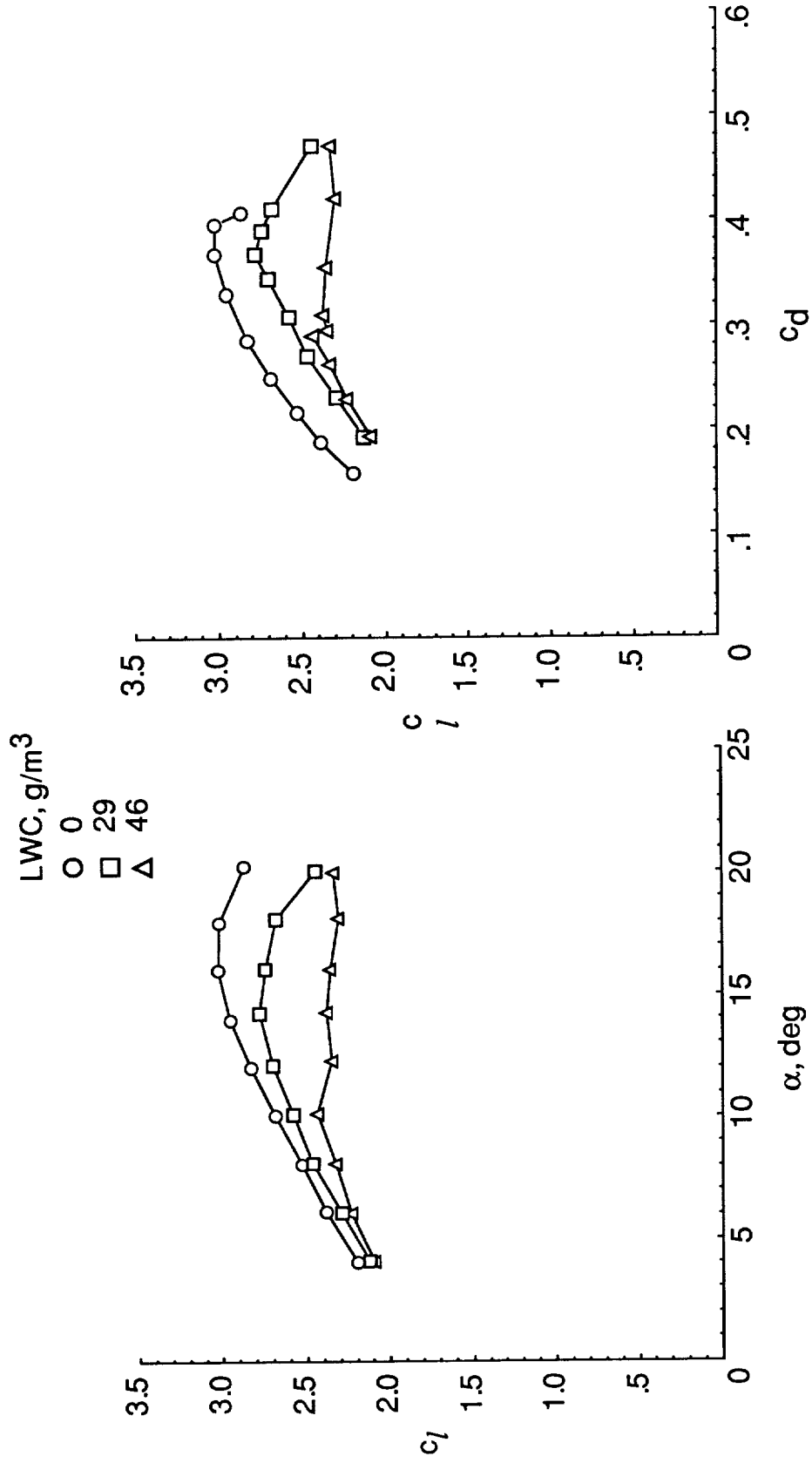


Figure 27. Landing configuration lift curve and drag polar at dynamic pressure of 30 psf.

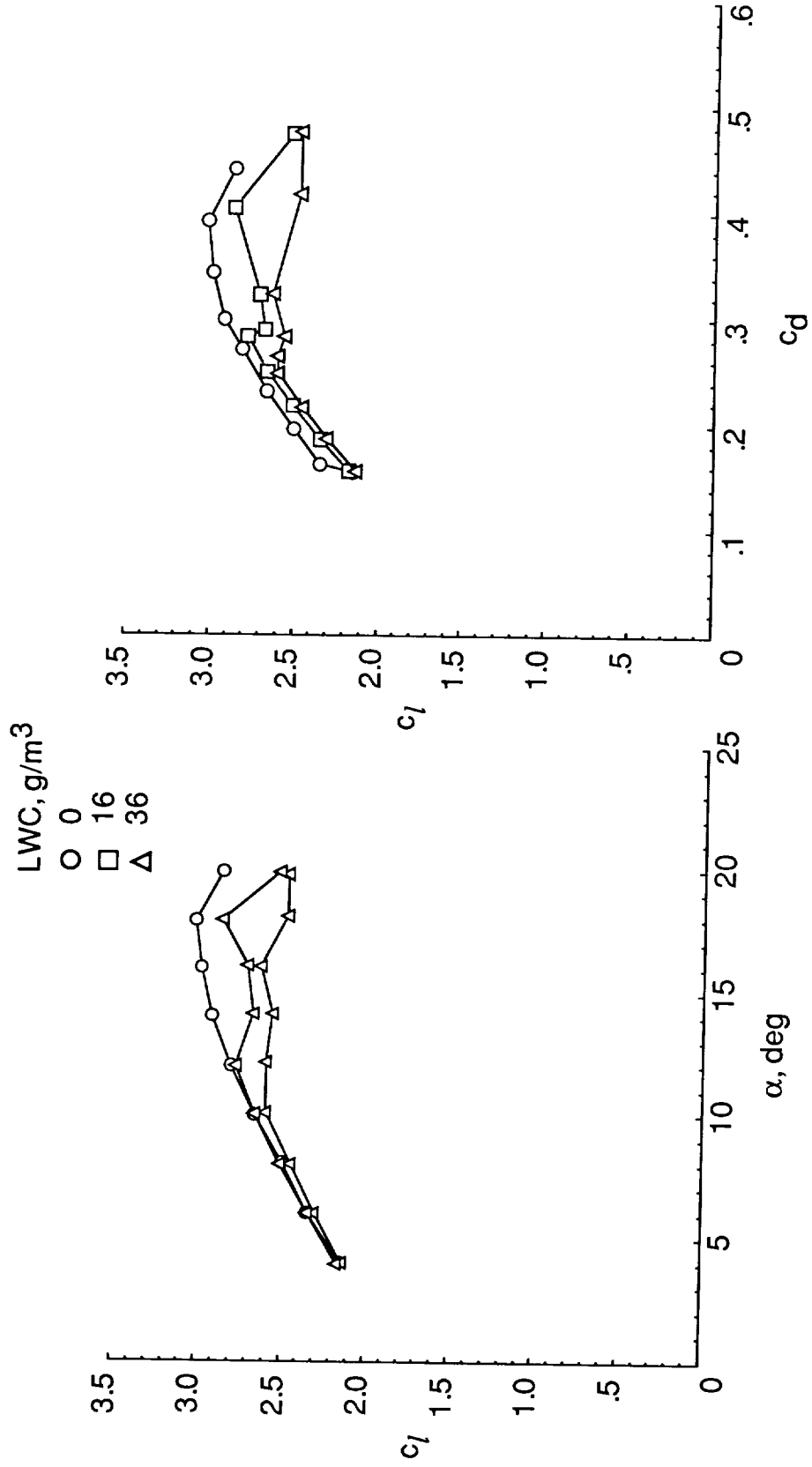


Figure 28. Landing configuration lift curve and drag polar at dynamic pressure of 50 psf.

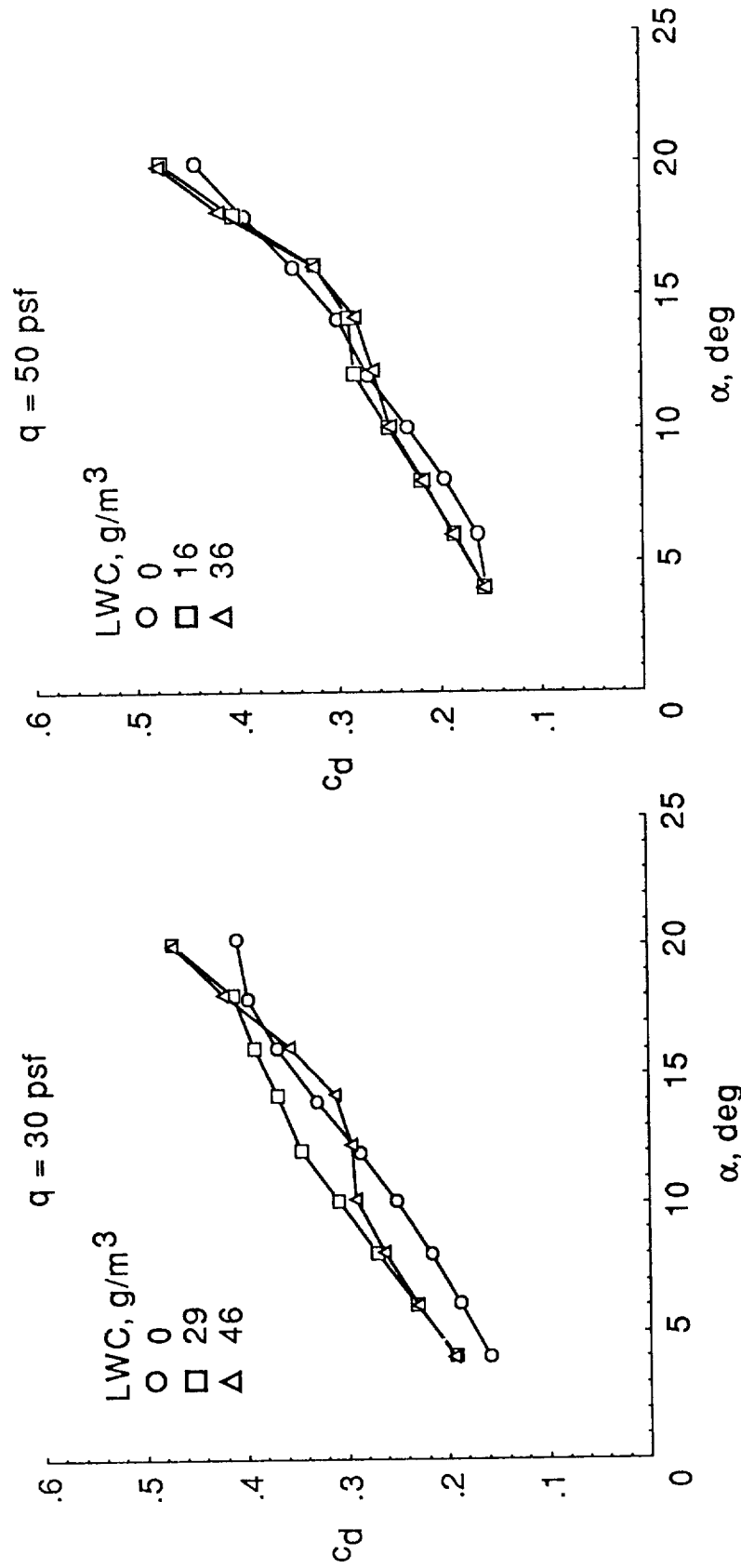
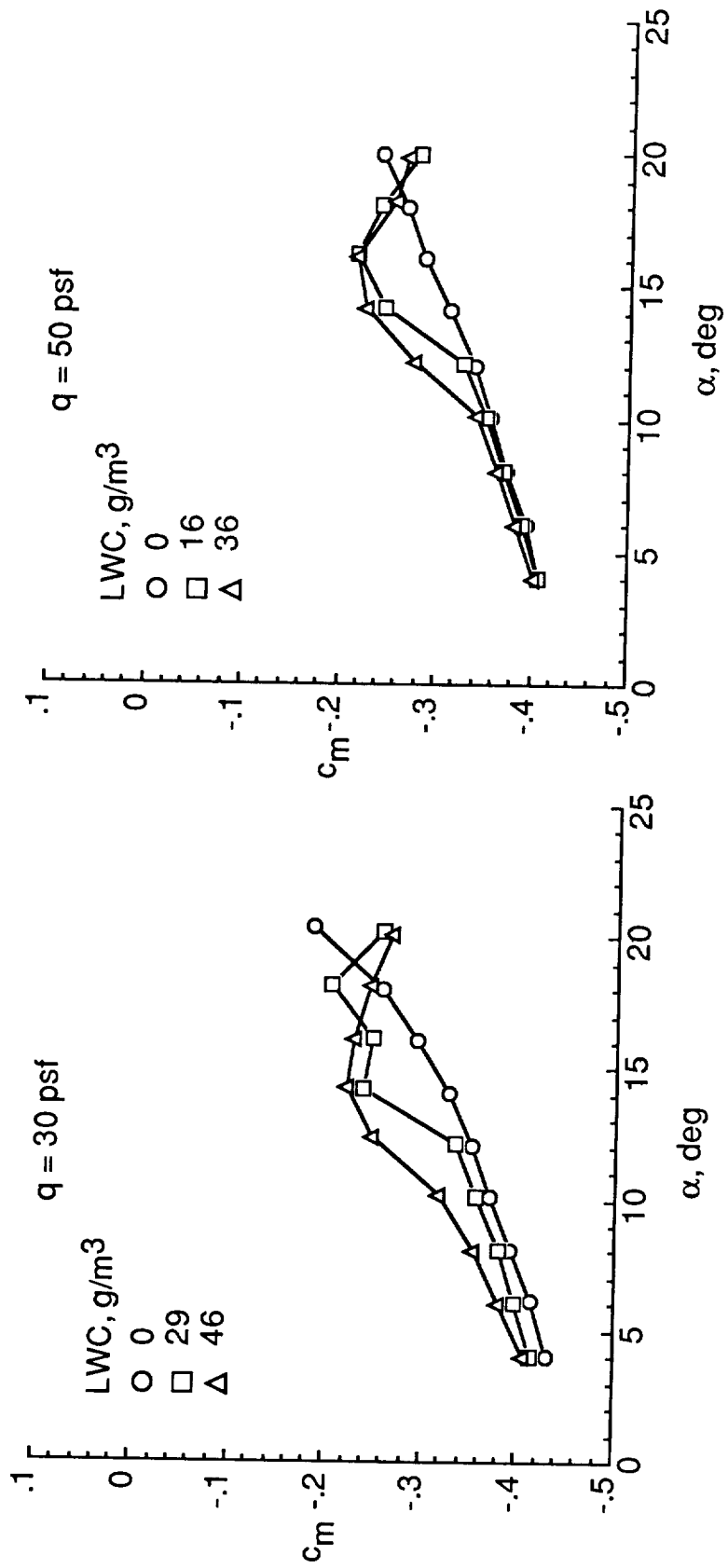
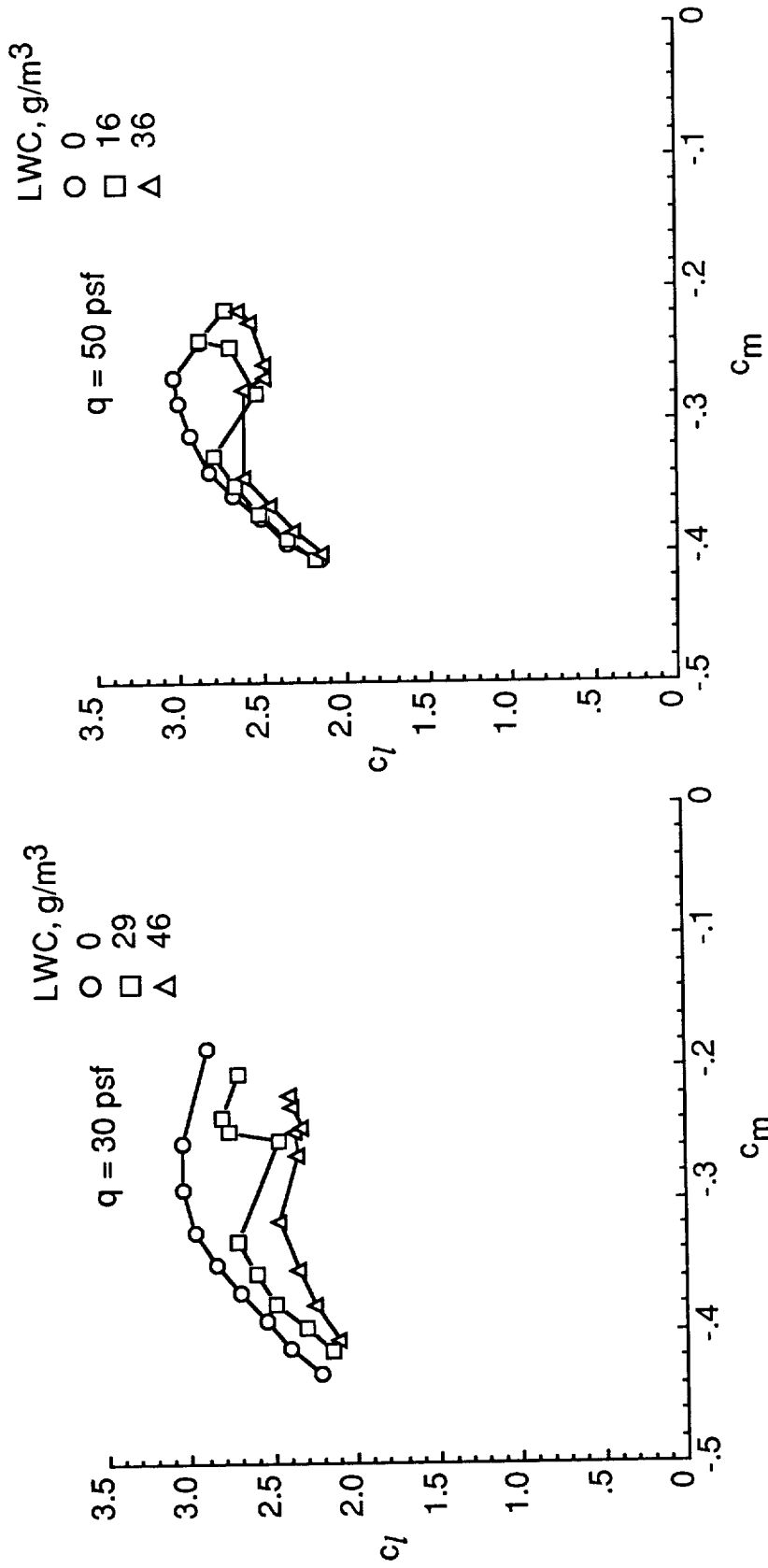


Figure 29. Landing configuration drag as a function of angle of attack.



(a) Pitching moment as a function of angle of attack.

Figure 30. Effect of rain on landing configuration pitching moment.



(b) Lift as a function of pitching moment.

Figure 30. Concluded.

ORIGINAL PAGE
BLACK AND WHITE PHOTOGRAPH

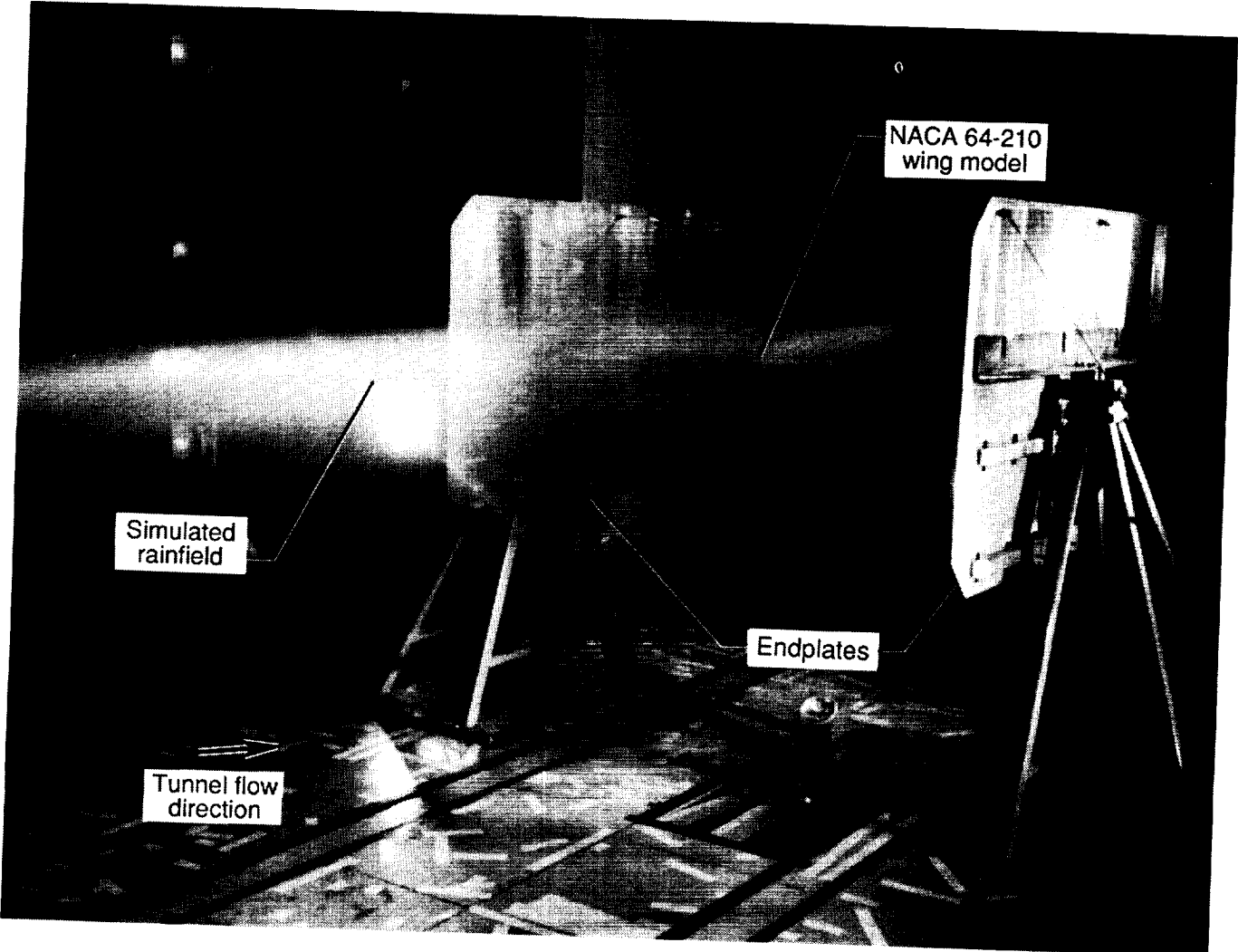
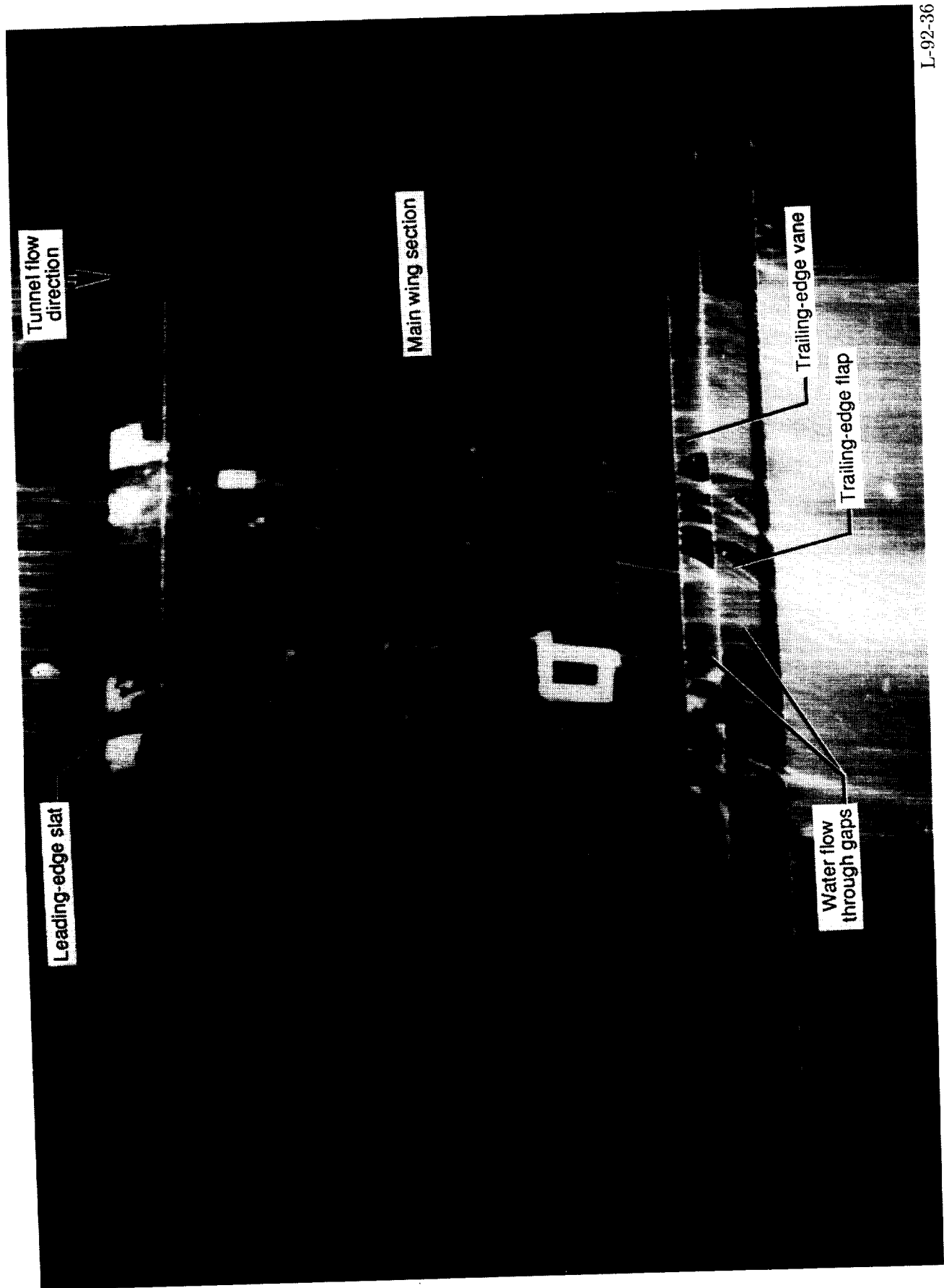


Figure 31. View looking downstream of NACA 64-210 airfoil model immersed in water spray in Langley 14-foot 22-Foot Subsonic Tunnel. L-85-13352



L-92-36

Figure 32. Sample of typical water film pattern on upper surface of model for landing configuration at angle of attack of 8° , dynamic pressure of 30 psf, and $LWC = 46 \text{ g/m}^3$.

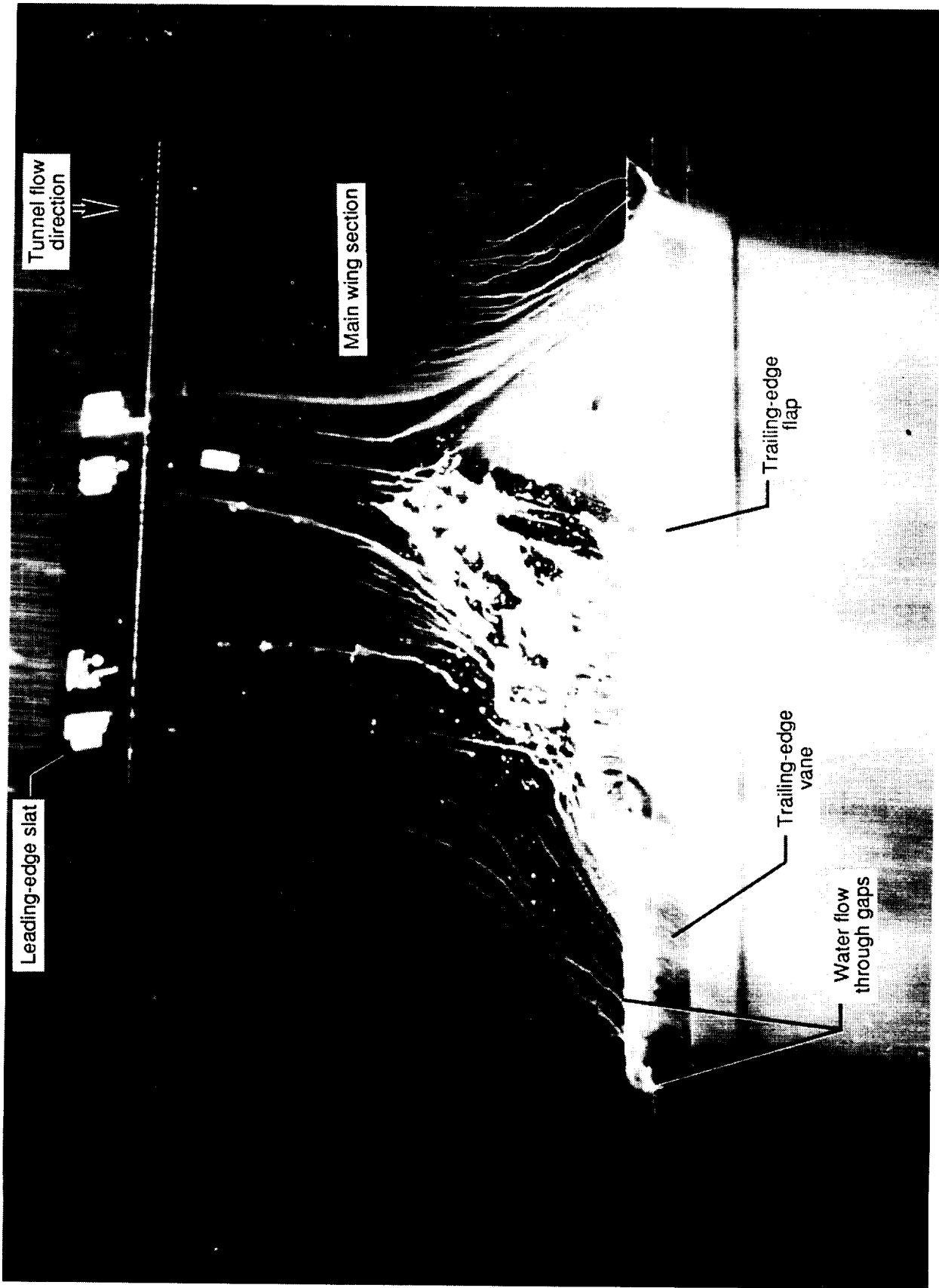
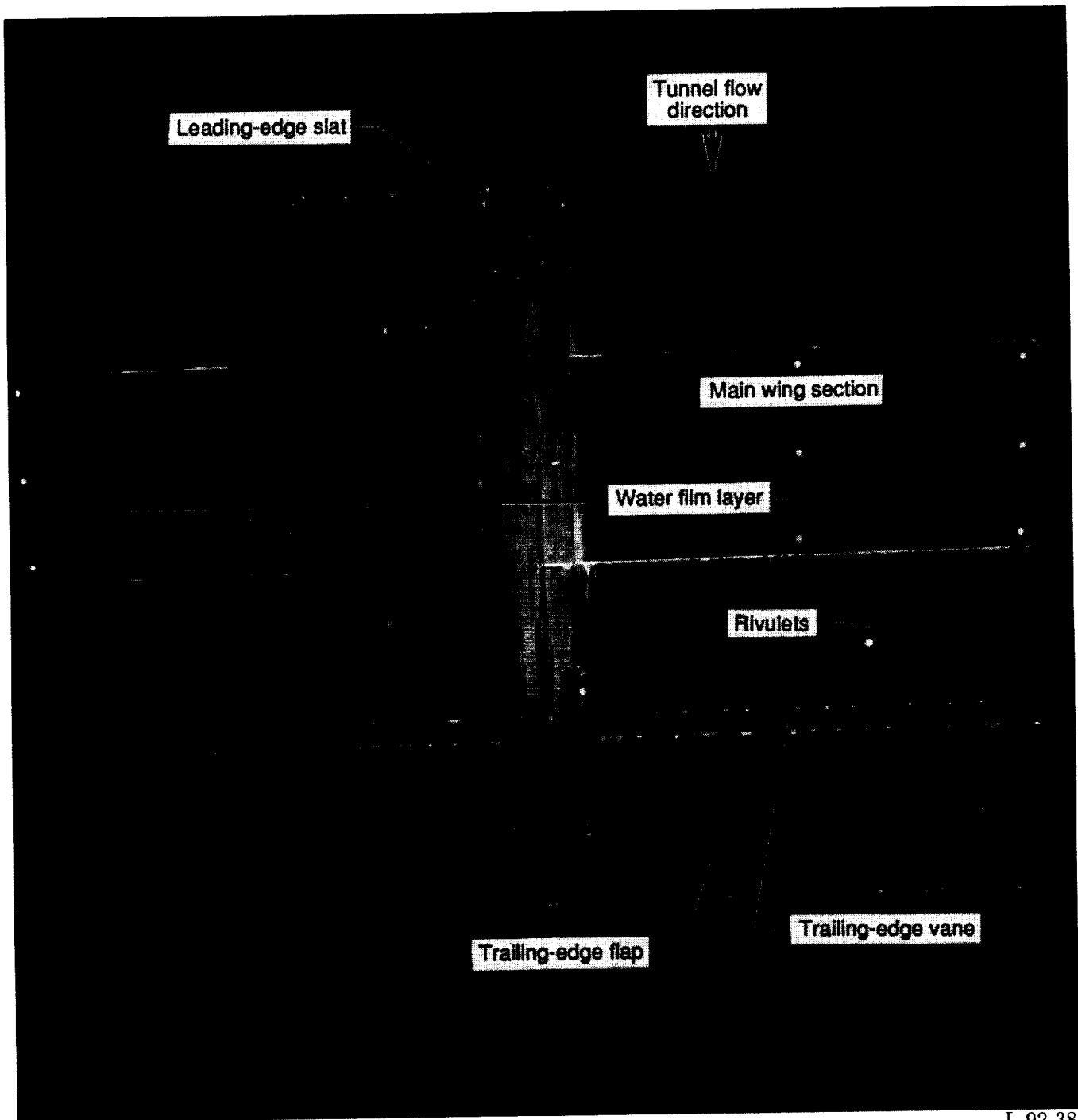


Figure 33. Sample of typical water film pattern on upper surface of model for landing configuration at angle of attack of 20° , dynamic pressure of 30 psf, and $LWC = 46 \text{ g/m}^3$.

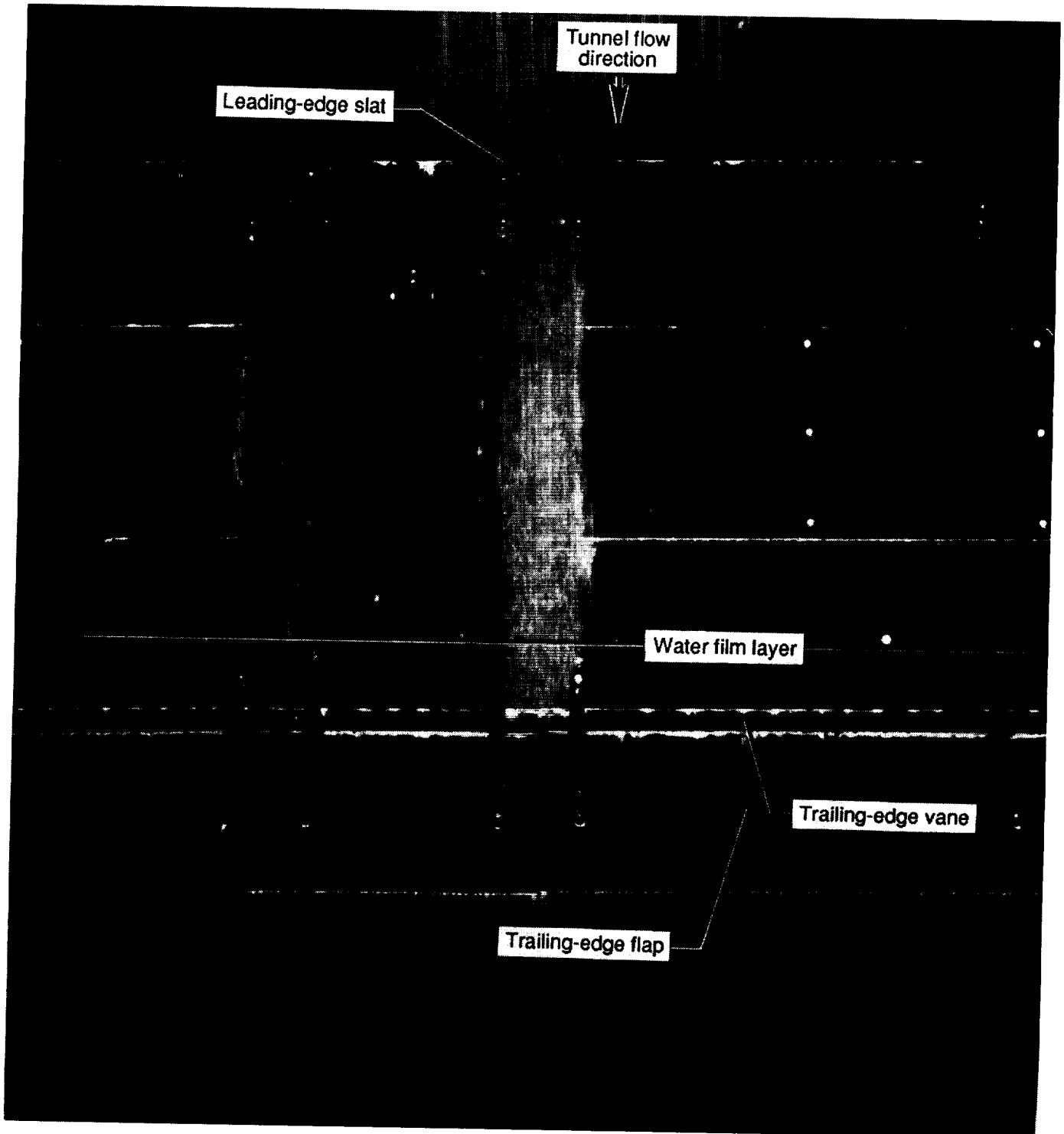
L-92-37



L-92-38

Figure 34. Sample of typical water film pattern on lower surface of model for landing configuration at angle of attack of 4° , dynamic pressure of 30 psf, and $LWC = 29 \text{ g/m}^3$.

ORIGINAL PAGE
BLACK AND WHITE PHOTOGRAPH



L-92-39

Figure 35. Sample of typical water film pattern on lower surface of model for landing configuration at angle of attack of 20° , dynamic pressure of 30 psf, and $LWC = 29 \text{ g/m}^3$.

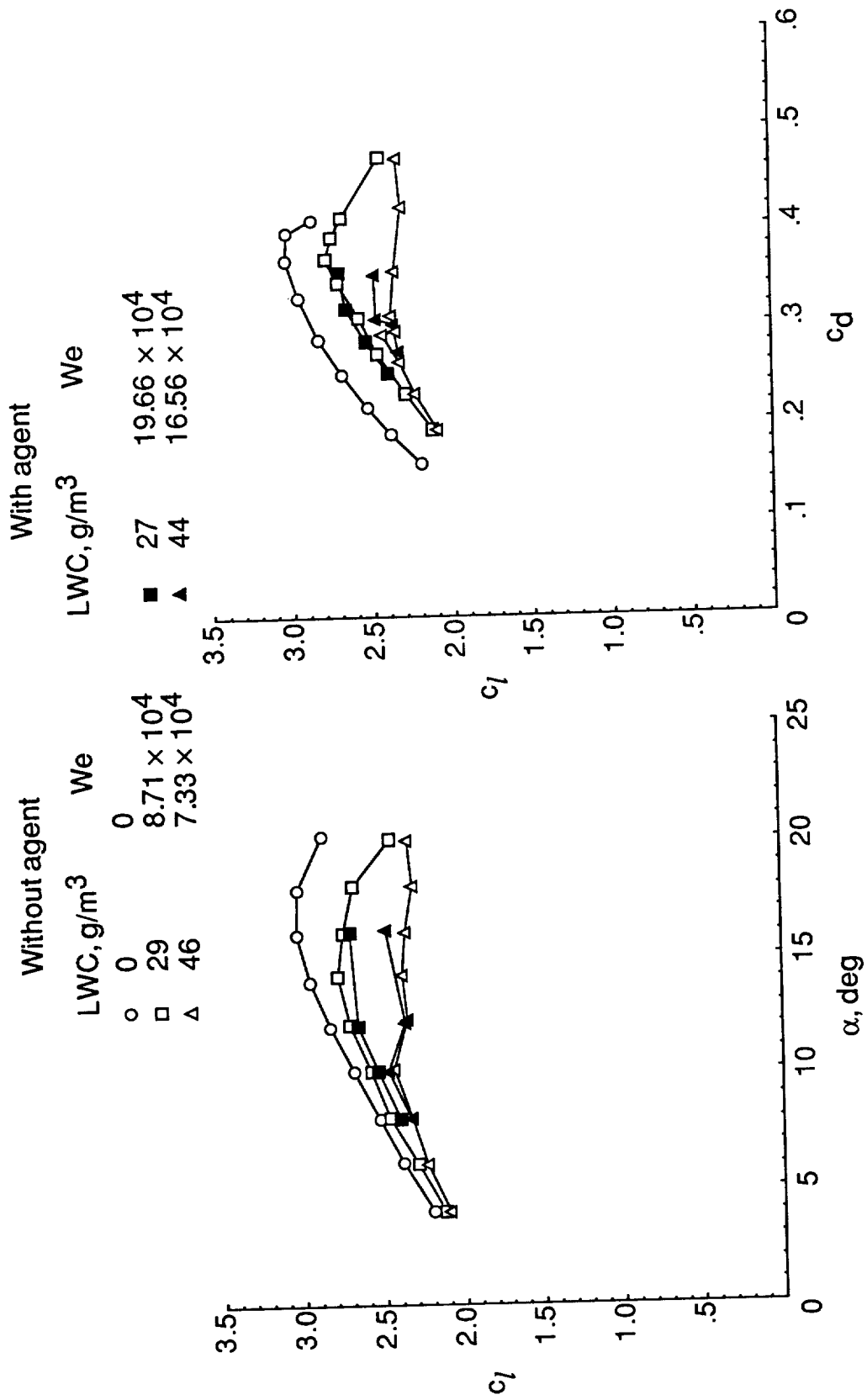


Figure 36. Water surface tension effects on landing configuration at dynamic pressure of 30 psf.

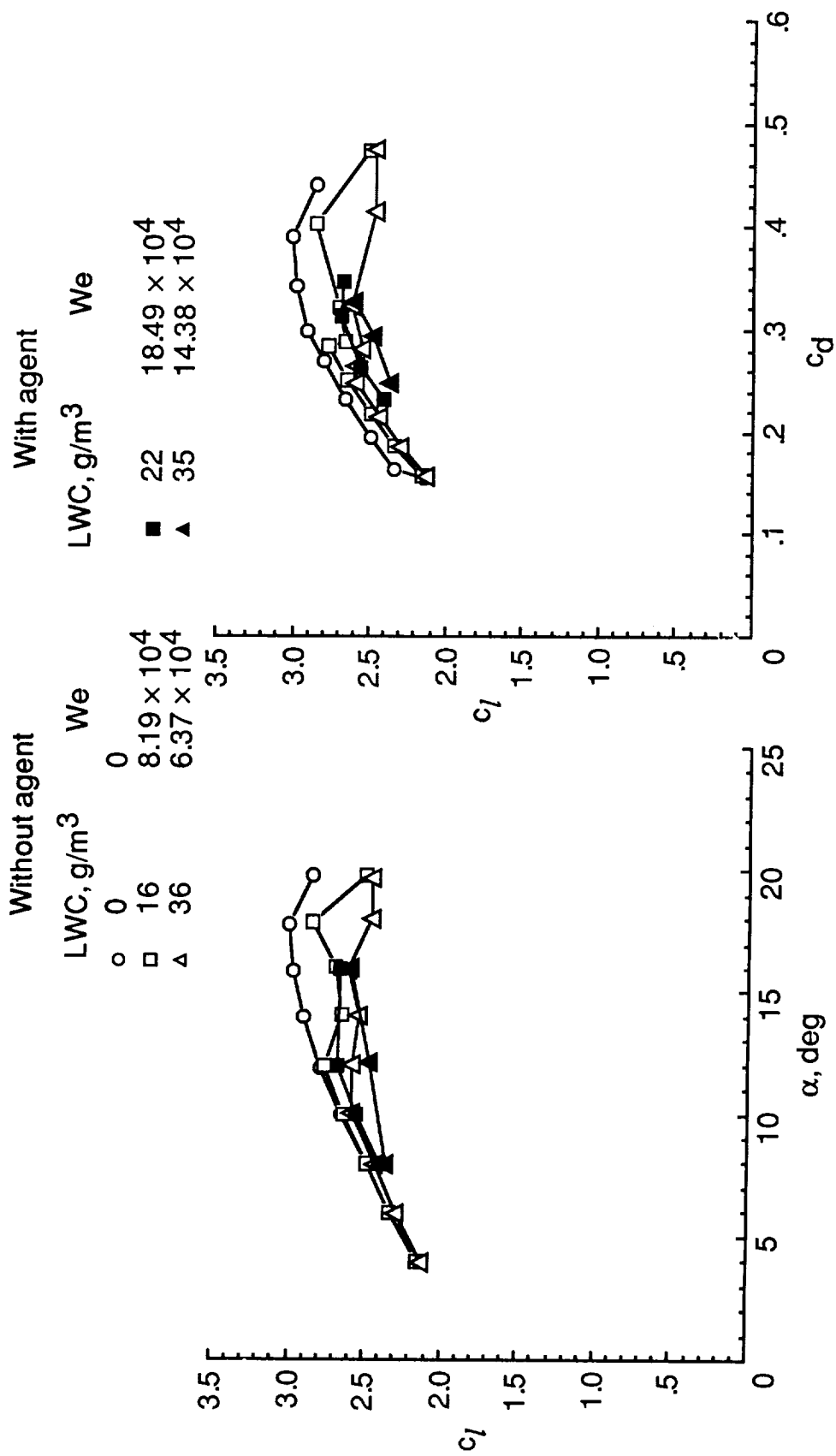


Figure 37. Water surface tension effects on landing configuration at dynamic pressure of 50 psf.

REPORT DOCUMENTATION PAGE			Form Approved OMB No. 0704-0188	
Public reporting burden for this collection of information is estimated to average 1 hour per response, including the time for reviewing instructions, searching existing data sources, gathering and maintaining the data needed, and completing and reviewing the collection of information. Send comments regarding this burden estimate or any other aspect of this collection of information, including suggestions for reducing this burden, to Washington Headquarters Services, Directorate for Information Operations and Reports, 1215 Jefferson Davis Highway, Suite 1204, Arlington, VA 22202-4302, and to the Office of Management and Budget, Paperwork Reduction Project (0704-0188), Washington, DC 20503.				
1. AGENCY USE ONLY (Leave blank)	2. REPORT DATE August 1992	3. REPORT TYPE AND DATES COVERED Technical Paper		
4. TITLE AND SUBTITLE Wind Tunnel Aerodynamic Characteristics of a Transport-Type Airfoil in a Simulated Heavy Rain Environment			5. FUNDING NUMBERS WU 505-68-01-02	
6. AUTHOR(S) Gaudy M. Bezos, R. Earl Dunham, Jr., Garl L. Gentry, Jr., and W. Edward Melson, Jr.				
7. PERFORMING ORGANIZATION NAME(S) AND ADDRESS(ES) NASA Langley Research Center Hampton, VA 23681-0001			8. PERFORMING ORGANIZATION REPORT NUMBER L-16959	
9. SPONSORING/MONITORING AGENCY NAME(S) AND ADDRESS(ES) National Aeronautics and Space Administration Washington, DC 20546-0001			10. SPONSORING/MONITORING AGENCY REPORT NUMBER NASA TP-3184	
11. SUPPLEMENTARY NOTES Bezos, Dunham, and Gentry: Langley Research Center, Hampton, VA; Melson: Wallops Flight Facility, Wallops Island, VA.				
12a. DISTRIBUTION/AVAILABILITY STATEMENT Unclassified-Unlimited Subject Category 02			12b. DISTRIBUTION CODE	
13. ABSTRACT (Maximum 200 words) The effects of simulated heavy rain on the aerodynamic characteristics of an NACA 64-210 airfoil section equipped with leading- and trailing-edge high-lift devices were investigated in the Langley 14- by 22-Foot Subsonic Tunnel. The model had a chord of 2.5 ft, a span of 8 ft, and was mounted on the tunnel centerline between two large endplates. Aerodynamic measurements in and out of the simulated rain environment were obtained for dynamic pressures of 30 and 50 psf and an angle-of-attack range of 0° to 20° for the cruise configuration and 4° to 20° for the landing configuration. The rain intensity was varied to produce liquid water contents ranging from 16 to 46 g/m ³ . The results obtained for various rain intensity levels and tunnel speeds showed significant losses in maximum lift capability and increases in drag for a given lift as the liquid water content was increased. The results obtained on the landing configuration also indicate a progressive decrease in the angle of attack at which maximum lift occurred and an increase in the slope of the pitching-moment curve as the liquid water content was increased. The sensitivity of test results to the effects of the water surface tension was also investigated. A chemical was introduced into the rain environment that reduced the surface tension of water by a factor of 2. The reduction in the surface tension of water did not significantly alter the level of performance losses for the landing configuration.				
14. SUBJECT TERMS Heavy rain effects; Transport-type airfoil; Aerodynamic performance degradation; Small-scale wind tunnel results			15. NUMBER OF PAGES 66	
			16. PRICE CODE A04	
17. SECURITY CLASSIFICATION OF REPORT Unclassified	18. SECURITY CLASSIFICATION OF THIS PAGE Unclassified	19. SECURITY CLASSIFICATION OF ABSTRACT	20. LIMITATION OF ABSTRACT	